Trace elements in silicate melts and the thermal conductivity of the Earth's deep mantle: insights from atomistic modeling of geomaterials

Inauguraldissertation
zur Erlangung des Grades eines
Doktors der Naturwissenschaften
am Fachbereich Geowissenschaften
der Freien Universität Berlin

Vorgelegt von Dipl.-Phys. Volker Haigis

Berlin, 2013

Promotionskommission:

Prof. Dr. Susan Schorr, FU Berlin (Vorsitzende)
Dr. Sandro Jahn, GFZ Potsdam und FU Berlin (Erstgutachter)
PD Dr. Ralf Milke, FU Berlin (Zweitgutachter)
Prof. Dr. Harry Becker, FU Berlin
Dr. Uwe Wiechert, FU Berlin

Tag der Disputation: 31. Januar 2013

Contents

Zusammenfassung

Die vorliegende Arbeit behandelt zwei Aspekte der chemischen und thermischen Heterogenität der gegenwärtigen Erde: die Verteilung von Spurenelementen und die thermische Leitfähigkeit des unteren Mantles. Elementverteilung und Wärmetransport sind makroskopische Phänomene, die sich z.B. in Mineralen und Gesteinen oder auf noch größeren Längenskalen abspielen, wenn man die Erde als ganze als chemisch differenzierten Körper mit einem geothermalen Temperaturgradienten auffasst. Diese Phänomene leiten sich jedoch von mikroskopischen, atomaren Eigenschaften der beteiligten Materialien ab: die Verteilung von Spurenelementen hängt von chemischen Affinitäten ab, die ihrerseits bestimmt werden von der Verfügbarkeit energetisch günstiger lokaler Umgebungen für Spurenelementatome in den verschiedenen Wirtsphasen. Der Gitterbeitrag zur Wärmeleitfähigkeit hängt von Schwingungseigenschaften des Kristallgitters ab, die den Wärmefluss auf atomarer Ebene bestimmen. In dieser Arbeit verwenden wir atomistische Computersimulationen, um erstens die mikroskopischen Mechanismen aufzuklären, die den Einbau von Spurenelementen in Silikatschmelzen und ihr Verteilungsverhalten in Gegenwart von Silikatschmelzen steuern. Zum zweiten benutzen wir die Methode der atomistischen Modellierung, um den Gitterbeitrag zur Wärmeleitfähigkeit von Mineralen des unteren Mantels bei hohen Drücken und Temperaturen zu erhalten. Dies erlaubt es, mit dem Wärmefluss durch die Kern-Mantel-Grenze einen wichtigen geophysikalischen Parameter zu bestimmen.

In Kapitel 2 untersuchen wir die Struktur von Aluminosilikat-Schmelzen und -Gläsern mit 76 mol% SiO_2 und unterschiedlichem Y- und La-Gehalt mit Hilfe sowohl von Ab-initio- und klassischer Molekulardynamik (MD) als auch von Röntgen- und Neutronenbeugung. Für die Simulation der Gläser, die lange Laufzeiten erfordern, verwenden wir einen Satz klassischer Wechselwirkungspotentiale für das System Y-Ca-Al-Si-O, der zu diesem Zweck um La ergänzt wird. Das neue Potential wird validiert durch Vergleich der resultierenden *Schmelz*strukturen mit Schmelzstrukturen, die wir aus Ab-initio-MD-Simulationen erhalten, und durch Vergleich der resultierenden *Glas*strukturen mit experimentellen Daten. Sowohl die Ab-initio-Simulationen von Silikatschmelzen mit Seltenen Erden (REE, engl. rare-earth elements) als auch die klassischen Simulationen der entsprechenden Gläser weisen folgende Trends auf: Die durchschnittlichen Koordinationszahlen von Y und La nehmen mit zunehmendem REE-Gehalt ab, ebenso die durchschnittliche Koordinationszahl von Al. Außerdem ist die Verteilung der Al-Koordinationszahlen in den La-haltigen Schmelzen im Vergleich zu den Y-haltigen Schmelzen zu kleineren Werten verschoben. Diese Trends werden anhand der Feldstärken der beteiligten Kationen erklärt. Ein weiteres Ergebnis der Ab-initio-Simulationen ist die Verletzung der Al-Vermeidungsregel (Loewenstein-Regel) in den hier untersuchten REE-haltigen Aluminosilikatschmelzen.

Kapitel 3 widmet sich dem Einbau von Y als Spurenelement in Calcium-Aluminosilikatschmelzen, der mit Hilfe von von klassischen MD-Simulationen und EXAFS- (engl. Extended X-ray Absorption Fine Structure)-Spektroskopie untersucht wird. Ziel ist es zu verstehen, wie die Schmelzzusammensetzung, insbesondere der Ca-Gehalt und die Polymerisierung der Schmelze, das Verteilungsverhalten von Y zwischen Mineralen und Schmelzen oder zwischen verschiedenen Schmelzen beeinflusst. Zunächst untersuchen wir die Veränderung der lokalen Umgebung von Y in Abhängigkeit von der Schmelzzusammensetzung. Sowohl die Simulationen als auch die EXAFS-Messungen zeigen, dass die durchschnittliche Koordinationszahl von Y und der durchschnittliche Y-O-Abstand mit zunehmendem Ca-

Gehalt, d.h. mit wachsender Depolymerisierung, abnehmen. Außerdem ergeben die Simulationen, dass Y vorzugsweise mit Ca in der zweiten Koordinationsschale assoziiert ist. In einem weiteren Schritt stellen wir einen Zusammenhang zwischen diesen strukturellen Informationen und der *Energetik* her: die Technik der thermodynamischen Integration erlaubt es uns, die Gleichgewichtskonstante einer Austauschreaktion von Y und Al zwischen zwei unterschiedlichen Silikatschmelzen zu bestimmen. Die Minimierung der freien Energie, so das Ergebnis, führt zu einer Anreicherung von Y in der Ca-haltigen, weniger polymerisierten Schmelze. Dieses Resultat steht im Einklang mit experimentellen Daten und liefert eine Erklärung der beoachteten Verteilungstendenzen durch Prozesse auf atomarer Ebene.

In Kapitel 4 verlassen wir das Gebiet der Spurenelemente in Silikatschmelzen und wenden uns dem zweiten Aspekt der vorliegenden Arbeit zu, nämlich der Wärmeleitfähigkeit des unteren Erdmantels. Diesen betrachten wir als ein Aggregat von Ferroperiklas, (Mg,Fe)O, und Magnesiumsilikat, (Mg,Fe)SiO_3, in der Perowskitstruktur (bzw. in der Postperowskitstruktur nahe der Kern-Mantel-Grenze). Wir bestimmen den Gitterbeitrag zur Wärmeleitfähigkeit der drei Phasen mittels klassischer Gleichgewichts-MD-Simulationen und der Green-Kubo-Methode in einem weiten Druck- und Temperaturbereich, der auch die Bedingungen an der Kern-Mantel-Grenze abdeckt. Die Leitfähigkeiten der einzelnen Phasen werden dann als Funktion der Dichte und der Temperatur parametrisiert, und die Leitfähigkeit des Mantelaggregats wird entlang einer Modellgeotherme berechnet. Unter der Annahme, dass der Eisengehalt der Minerale ihre Wärmeleitfähigkeit um 50% reduziert, wie es experimentelle Ergebnisse nahelegen, erhalten wir den Gitterbeitrag zur Wärmeleitfähigkeit eines eisenhaltigen Aggregats mit der mineralogischen Zusammensetzung des unteren Mantels bis hinunter zur Kern-Mantel-Grenze, wo er 8 W/(mK) beträgt. Dies ist unseres Wissens die erste Bestimmung der thermischen Leitfähigkeit des tiefen Mantels direkt bei den entsprechenden Drücken und Temperaturen, ohne die sonst üblichen Extrapolationen auf Grundlage von Niederdruck- und Niedertemperatur-Daten. Wir schätzen den Gitterbeitrag zum globalen Wärmefluss durch die Kern-Mantel-Grenze auf 11 Terawatt.

Summary

The present thesis deals with two aspects which are related to the present Earth's chemical and thermal heterogeneity, namely trace element partitioning and the lattice thermal conductivity of the lower mantle. Element partitioning and heat conduction are macroscopic phenomena occurring, e.g., within minerals and rocks or on even larger scales, if the Earth as a whole is considered as a chemically differentiated body with a geothermal temperature gradient. But these phenomena are rooted in the atomic-scale properties of the involved materials: trace element partitioning depends on chemical affinities which, in turn, are governed by the availability of energetically favorable local environments for trace element atoms in alternative host phases. The lattice thermal conductivity is determined by vibrational properties of the crystal lattice which control the heat flux on an atomic scale. In this thesis, we use atomistic computer simulations, first, to elucidate the microscopic mechanisms governing the incorporation of trace elements into silicate melts and their partitioning behavior in the presence of silicate melts. Second, the atomistic modeling approach is employed to obtain the lattice thermal conductivity of lower-mantle minerals at high pressures and temperatures. This allows us to constrain the heat flux across the core-mantle boundary, an important geophysical parameter.

In chapter 2, the structure of aluminosilicate melts and glasses with 76 mol% SiO_2 and varying amounts of Y and La is studied by means of ab-initio and classical molecular dynamics (MD) simulations as well as x-ray and neutron diffraction experiments. For the simulation of glasses, requiring long simulation times, we use a set of classical interaction potentials for the system Y-Ca-Al-Si-O which is extended to La for this purpose. The new potential is validated by comparing the resulting *melt* structures to melt structures obtained from ab-initio MD simulations and by checking the resulting *glass* structures against experimental data. Both the ab-initio simulations of rare earth element (REE)-bearing melts and the classical simulations of the respective glasses reveal the following major structural trends: the average coordination numbers of Y and La decrease with increasing REE content, and so does the average coordination number of Al. Furthermore, the distribution of Al coordination numbers is shifted to lower values in La-bearing melts, as compared to Y-bearing melts. These trends are rationalized in terms of cation field strengths. As another result, the ab-initio MD simulations show that the Al avoidance, or Loewenstein, rule is not valid for the studied REE-bearing aluminosilicate melts.

Chapter 3 is devoted to the incorporation of Y as a trace element into calcium aluminosilicate melts, which is investigated by means of classical MD simulations and extended x-ray absorption fine structure (EXAFS) spectroscopy (on quenched melts). The aim is to understand how the melt composition, in particular the Ca content and the degree of melt polymerization, influences the partitioning behavior of Y between minerals and melts or between different melts. In a first step, the variation of the local environment of Y in response to changes in melt composition is studied. Both simulations and EXAFS measurements indicate that the average coordination number of Y decreases with increasing Ca content of the melt, i.e. with increasing depolymerization, and so does the average Y-O distance. Moreover, the simulations show that Y is preferentially associated with Ca in the second coordination shell. In a second step, this structural information is related to *energetics*: using the technique of thermodynamic integration, we determine the equilibrium constant for an exchange reaction of Y and Al between two different melts, and free energy minimization is found to drive Y into the Ca-bearing, less polymerized

melt. This result is consistent with experimental data and provides an atomic-scale explanation of the observed partitioning trends.

Leaving the field of trace elements in silicate melts and glasses, chapter 4 deals with the second aspect of the present thesis, which is the thermal conductivity of the Earth's lower mantle. The latter is assumed to be an aggregate of (Mg,Fe)O ferropericlase and (Mg,Fe)SiO_3 magnesium silicate in the perovskite structure (or the post-perovskite structure close to the core-mantle boundary). We determine the lattice thermal conductivities of the three iron-free phases by means of classical equilibrium MD simulations, in conjunction with the Green-Kubo approach, over a wide pressure and temperature range, reaching conditions representative of the core-mantle boundary. The conductivities of the individual phases are then parameterized as a function of density and temperature, and the thermal conductivity of the lower-mantle aggregate is calculated along a model geotherm. Assuming that the presence of iron impurities in the minerals reduce their thermal conductivity by 50%, as suggested by experimental results, we obtain the lattice thermal conductivity of an iron-bearing lower-mantle aggregate, down to the core-mantle boundary, where it reaches 8 W/(mK). To our knowledge, this is the first determination of the thermal conductivity of the deep mantle directly at the relevant pressures and temperatures, without the otherwise common extrapolation from low-P,T data. The lattice contribution to the global heat flux across the core-mantle boundary is estimated to be 11 terawatts.

Chapter 1

Introduction

1.1 Context of the thesis

The present Earth is a highly differentiated planetary body with both chemical and thermal inhomogeneities on large and short scales. Concerning the chemical heterogeneity, seismic data, geo- and cosmochemical considerations and results from mineral physics converge to the picture of an iron-rich core surrounded by a silicate mantle and crust (Stacey and Davis, 2008; Carlson, 2005). But chemical differentiation is also ubiquitous on much smaller scales within rocks or mineral grains and constitutes a key interest to petrologists and geochemists. The distribution of chemical elements in a mineral assemblage, for example, allows far-reaching conclusions concerning the petrogenetic history and has applications in geothermometry and geobarometry (Philpotts and Ague, 2009). Thermal inhomogeneities within the Earth, on the other hand, are the driving force for planetary dynamics: the temperature gradient between the hot core and the surface generates an outward heat flux which provides the energy for mantle convection and plate tectonics. Thermochemical gradients also drive the convection of the liquid outer core and therefore determine the energy available to the geodynamo which generates the magnetic field of our planet. Hence knowledge of the Earth's thermal budget and the heat transport through core and mantle materials is essential for an understanding of the current state and the evolution of the planet (Lay et al., 2008).

Given the fundamental importance of chemical and thermal inhomogeneities within in the Earth, the question arises how they could emerge from the more or less homogeneous solar nebula from which the planet is believed to have formed. As for the chemical differentiation, one possible scenario for the core formation that is currently discussed involves the segregation of iron-rich melt from a silicate magma ocean in the early history of the Earth (Rubie et al., 2009). Once this segregation has occurred, further differentiation is governed by gravitation which drives the denser metallic melt into the core. But the segregation itself, starting probably on a sub-millimeter scale, is rooted in chemical affinities which thermodynamically lead to a separation into a silicate and an iron-rich phase. Likewise, the concomitant partitioning of lithophile elements into the silicate fraction and of the siderophile elements into the metallic phase is governed by chemical affinities (Goldschmidt, 1937). Apart from playing an important role in this primordial differentiation event, the underlying chemical and thermodynamic principles equally apply to differentiation processes at later stages of planetary evolution. They control, e.g., the element partitioning during crystallization and fractional melting in magmatic systems (Shaw, 2006) as well as the partitioning between minerals and fluids during ore formation.

As for the origins of thermal inhomogeneities within the Earth, thermal conductivity plays a key role. Heat is transported through Earth via convection and conduction, and in the absence of thermal boundary layers, thermal transport is mostly convective (Stacey and Davis, 2008). However, heat transfer across thermal boundary layers at the core-mantle boundary or at the Earth's surface is dominated by conduction. Hence for a given heat flux, the thermal conductivity of the materials present at the boundary

determines the temperature gradient across the boundary (and vice versa). Furthermore, the thermal conductivity also impacts the convective regime of the Earth's mantle via the Rayleigh number. To make a connection to the chemical differentiation discussed above, we mention that based on geodynamic simulations, Naliboff and Kellogg (2007) suggest a link between the thermal conductivity and large-scale heterogeneity of the mantle.

The preceding discussion sets the context for the present thesis, which is devoted to two particular aspects of the broad subject outlined above. One concerns the atomic-scale processes that govern trace element partitioning. On the atomic level, the distribution of a trace element between several coexisting phases depends on how well (or how badly) it "fits" into the structural environment offered by the alternative host phases. For *crystalline* host phases, this informal statement can be expressed in more quantitative terms by the lattice strain model, which explains the observed trends in minor and trace element partitioning as a function of crystal chemistry successfully and in many cases quantitatively (Blundy and Wood, 1994). However, the influence of melt or fluid composition (and structure) on partitioning is less well understood, although it can strongly affect the conclusions drawn from the lattice strain model alone (Schmidt et al., 2006). A complete picture of element partitioning between minerals and melts/fluids or between different melts requires an understanding of the mechanisms by which melt/fluid composition influences the distribution of trace elements. This thesis investigates the behavior of two trace elements, Y and La, in silicate melts by means of atomistic simulation. We propose an atomic-scale explanation of how melt composition affects the structural environments and thus the chemical affinities of trace elements.

The second aspect of the thesis concerns the thermal conductivity of the Earth's lower mantle. The mineralogy of the latter is believed to be dominated by ferropericlase, (Mg,Fe)O, and perovskite, (Mg,Fe)SiO_3, with respective volume fractions of approximately 80% and 20% (Piazzoni et al., 2007). Close to the core-mantle boundary, the (Mg,Fe)SiO_3 fraction probably undergoes a phase transition to the post-perovskite structure (Murakami et al., 2004; Oganov and Ono, 2004). The thermal conductivity depends strongly on temperature and pressure, but no general, exact theory of this dependence is currently available. Therefore, values of the conductivity at deep-mantle conditions either have to be determined directly at the relevant temperatures and pressures or must be inferred from low-P,T values and more or less heuristic extrapolation schemes to deep-mantle conditions. Conductivity measurements have been performed at lower-mantle pressures and room temperature (Ohta et al., 2012) as well as at intermediate pressures and temperatures (Manthilake et al., 2011a), but no experimental data are currently available at both temperature *and* pressure conditions of the deep mantle. Computer simulations are a valuable tool to probe conditions which are not accessible to experiments. To date, computational techniques have been used to obtain the thermal conductivity of MgO up to pressures and temperatures corresponding to the core-mantle boundary (de Koker, 2010; Tang and Dong, 2010; Stackhouse et al., 2010), but no simulation results on the $MgSiO_3$ phases are currently available, to our knowledge. In this thesis, we use atomistic simulations to determine the thermal conductivities of MgO, $MgSiO_3$ perovskite and post-perovskite directly in the pressure and temperature range of the lower mantle.

1.2 The atomistic simulation approach to material modeling

Science is not only devoted to an accurate description of the world surrounding us but is also driven to a large extent by the search for general underlying principles which explain seemingly unrelated phenomena. Thermodynamics constitutes a good example for this reductionist approach, tracing back highly manifold phenomena to more basic principles: its innumerable applications in physics, chemistry, geoscience, biology, engineering and other fields are all governed by the same few laws. These thermodynamic laws, in turn, are themselves rooted in the even more fundamental principles of statistical mechanics, i.e. in the statistical description of systems containing a large number of constituents such as atoms or molecules (Callen, 1985). The promise associated with the reductionist approach is appealing:

once the fundamental laws are known which govern the behavior and the interactions of the constituents of a large system (e.g., atoms), all macroscopic thermodynamic properties of arbitrary systems made up of these constituents (e.g., a mineral) can be deduced, at least in principle.

This is the spirit in which the atomistic simulation approach to material modeling was developed (Allen and Tildesley, 1987; Frenkel and Smit, 2002). It makes use of computer algorithms in which the system under study is represented as a collection of atoms or molecules in a simulation cell (the name "molecular dynamics" or MD remains in use for historical reasons even if the constituent particles are in fact atoms). For a given atomic configuration, the forces acting on the individual atoms due to their interactions with each other are calculated, either on the basis of fundamental laws of nature (quantum mechanics) or via a simpler parameterized interaction potential. The atoms are then moved over a short distance according to these forces, typically in time steps of about 1 fs, and the procedure is repeated for the new configuration and with new forces, and so on. Thus, MD simulations generate numerically a collection of atomic trajectories through space and time which mimic the dynamics of the real system. After a period of equilibration, the system will have lost its memory of the initial configuration and velocities, and thermodynamic equilibrium is reached. Note, however, that there are "pathological", non-ergodic systems in which the configurational sampling during a simulation does not represent thermodynamic equilibrium and the system is trapped in a configurational subspace determined by the initial conditions (Frenkel and Smit, 2002). This is the case in glasses, e.g., which have therefore to be treated in a more subtle manner and will be discussed in detail in chapter 2.

Most measurements on real systems are not designed to "see" individual atoms at a given moment of time but probe sample volumes containing a great number of atoms over a time span which is large compared to, e.g., the time scale of atomic vibrations in the system. The result of such a measurement therefore represents an average over many atoms and configurations (Callen, 1985). In MD simulations, the extraction of macroscopic quantities such as temperature, pressure, stress, free energy, thermal conductivity, and others, from a collection of atomic trajectories follows the same route, i.e. averaging over the individual atoms and over the portion of the simulation time which represents thermodynamic equilibrium. But atomistic simulations are not restricted to mimicking experimental measurements. Since they provide a complete atomic-scale picture *and* the thermodynamic variables of the system at the same time, they are very suitable in establishing structure-property relations. They also provide information which is not easily accessible to experiments: they support, e.g., the assignment of peaks in experimental spectra to atomic-scale processes (Spiekermann et al., 2012) or help to interpret diffraction data of disordered phases by decomposing the total structure factor into partials (Drewitt et al., 2011). But atomistic simulations also open a path to conditions under which experiments are currently impossible (Gillan et al., 2006). Alfè et al. (1999) used ab-initio MD simulations to compute the melting curve of iron up to inner-core pressures. From the known pressure profile of the Earth and the calculated melting curve, they obtained the temperature at the boundary between solid inner and liquid outer core, which was only poorly constrained before. Another hallmark of atomistic simulation in geoscience is the discovery of the high-pressure $MgSiO_3$ post-perovskite phase in a joint computational and experimental effort (Oganov and Ono, 2004).

MD simulations can be classified into ab-initio or classical approaches, according to the way in which they compute interatomic forces. Ab-initio or first-principles MD simulations are based on fundamental laws of nature (quantum mechanics) and are therefore very accurate and predictive, which makes them highly transferable, i.e. applicable to a wide temperature, pressure and composition range. These advantages, however, come at the price of high computational costs. The usually applied Born-Oppenheimer approximation (Born and Oppenheimer, 1927) to the general quantum mechanical problem (Cohen-Tannoudji and Laloe, 1999) makes use of the dynamic decoupling of the fast electronic and the much slower nuclear dynamics: only the (valence) electrons' degrees of freedom are described quantum-mechanically by the Schrödinger equation (or an equivalent equation, see below), which has to be solved at each time step, i.e. for each atomic configuration. The nuclear coordinates, on the other

hand, are treated as parameters which evolve in time according to classical Newtonian dynamics, subject to the Born-Oppenheimer potential energy. The latter is defined by the (quantum mechanical) electronic energy and by classical electrostatic interactions and conveys the genuinely quantum-mechanical information. If one is only interested in the electronic ground state properties of the system, which is often the case for electronic insulators, the Schrödinger equation for the electrons can be recast in a simpler form using density functional theory (DFT) which makes larger systems computationally tractable in the first place (Hohenberg and Kohn, 1964; Kohn and Sham, 1965). In DFT, the electronic ground state energy does not depend on all electronic coordinates any more, but only on the electronic ground state density, which is determined via the self-consistent DFT equations at every time step. However, the exact density dependence of the ground state energy is not known and has to be approximated. For the present thesis, we use the local density approximation (LDA, Kohn and Sham (1965)). In many cases, a computational speed-up is achieved by Car-Parrinello dynamics (Car and Parrinello, 1985). With this method, the computationally demanding DFT equations for the electronic ground state density are solved only once, for the initial atomic configuration. Subsequently, the electronic degrees of freedom evolve in time according to fictitious classical dynamics which are designed in a clever way such as to keep the system close to the Born-Oppenheimer potential energy surface over long times.

DFT and DFT-based MD simulations have proven to be an accurate and predictive tool for a broad range of applications, including the study of silicate melts (Vuilleumier et al., 2009). However, due to the approximative nature of LDA (and alternative proposed approximations), the method faces serious shortcomings in the treatment of systems with strong electronic correlations such as, e.g., transition metal oxides (Gori-Giorgi et al., 2009). Similarly, van der Waals interactions are not correctly described in the standard DFT scheme (Tkatchenko et al., 2012), but these are of secondary importance in the ionic systems studied in this thesis. Due to the high computational costs, ab-initio MD simulations are currently restricted to simulation cells containing a few hundred atoms and to simulation times of several tens of picoseconds.

Classical MD simulations, on the other hand, derive the interatomic forces from parameterized interaction potentials and do not treat the electronic degrees of freedom explicitly. This leads to much lower computational costs and makes classical MD suitable for the simulation of large systems and in cases where long run durations are needed, as in the case of glasses and in the calculation of thermal conductivities. However, the accuracy of classical interaction potentials has to be tested carefully. Furthermore, since they are usually parameterized with respect to specific structures or chemical compositions and for a certain range of temperatures and pressures, their transferability has to be checked before applying them to different systems or under different physical conditions. For this thesis, we used two forms of ionic interaction potentials for silicates with different degrees of sophistication which were parameterized with respect to DFT reference calculations. The polarizable ion model (Wilson and Madden, 1993) (PIM) improves on simple pair potentials by taking into account the electric polarizability of large ions. The electric polarization of individual ions is determined self-consistently at each time step, mimicking to some extent the variation of the environment-dependent electronic structure in ab-initio simulations. For this thesis, we parameterized the polarizable ion model for the system La-Y-Ca-Al-Si-O, and used it for the study of Y and La in silicate melts and glasses. More information on the functional form of the potential as well as on the parameterization and validation is provided in the following two chapters. The second set of interaction potentials has the form of an aspherical ion model (AIM) and adds effects of ionic shape deformation to the polarizable ion model. This makes it more flexible but also more expensive in terms of computation time. It was parameterized for the system Ca-Mg-Al-Si-O and has been shown to yield accurate results in a wide range of compositions, pressures and temperatures (Jahn and Madden, 2007). In this thesis, the aspherical ion model is used for the calculation of thermal conductivities.

1.3 Outline of the thesis

In chapter 2, the structure of Y- and La-bearing aluminosilicate melts and glasses is investigated by means of ab-initio and classical MD simulations as well as neutron and x-ray diffraction experiments. The main finding is a systematic variation of melt/glass structure with composition which can be rationalized in terms of the field strength of the various cations. The classical interaction potential, in the form of PIM, for the elements Y-Ca-Al-Si-O (Haigis et al., 2012b) is extended to La, and the chapter describes in detail the form of the polarizable ion model. This work is in preparation for publication in a peer-reviewed journal, in collaboration with the coauthors Louis Hennet and Marlène Leydier (CNRS-CEMHTI, 45071 Orleans CEDEX 2, France) and Sandro Jahn (GFZ German Research Centre for Geosciences, Telegrafenberg, 14473 Potsdam, Germany). VH performed the simulations and their analysis and wrote the manuscript, Louis Hennet and Marlène Leydier carried out the diffraction experiments, and Sandro Jahn supervised the research and commented on the manuscript.

Chapter 3 resumes the topic of the previous one, dealing with aluminosilicate melts with small amounts of Y, now treated as a trace element. But it extends the subject in two respects: first, the Y-bearing aluminosilicate melts in this study contain Ca as an additional cation, which acts as a network modifier, and the role of Ca for Y incorporation into the melts is studied. Second, this work goes beyond a description of the melt structure: the changes in melt structure around Y atoms upon variation of the melt composition are related to energetics. By means of thermodynamic integration, it is shown that the presence of Ca lowers the free energy of Y in the melt with respect to a Ca-free composition. This sheds light on the role of melt composition in trace element partitioning. In terms of methodology, this chapter also describes the parameterization of the new polarizable ion model for the system Y-Ca-Al-Si-O. It has been published in Chemical Geology (Haigis et al., 2012b), with the following contributions from the authors: VH carried out the MD simulations, analyzed the results and wrote the article, whereas Sebastian Simon and Max Wilke performed the EXAFS measurements and analyzed the data. Mathieu Salanne, Max Wilke and Sandro Jahn supervised the research and also commented on the manuscript.

In chapter 4, we leave the field of geochemistry and turn to a geophysical application of atomistic modeling. This chapter investigates the thermal conductivity of the lower-mantle minerals periclase (MgO) and $MgSiO_3$ in the perovskite and post-perovskite structure directly at lower-mantle conditions. This is done by means of classical equilibrium MD simulations in conjunction with the Green-Kubo approach, using the aspherical ion model of Jahn and Madden (2007). The thermal conductivity of the individual phases is parameterized as a function of density and pressure, and the thermal conductivity of a lower-mantle model aggregate is calculated along the geotherm, down to the core-mantle boundary. This chapter has been published in Earth and Planetary Science Letters (Haigis et al., 2012a) in collaboration with Mathieu Salanne, who provided the computer code for the calculation of thermal conductivities, and Sandro Jahn, who supervised the research. VH performed the simulations as well as the data analysis and wrote the article, and the coauthors commented on the manuscript.

Finally, we give an outlook and discuss ongoing work in the field of thermal conductivity.

Chapter 2

The structure of Y- and La-bearing aluminosilicate glasses and melts: a combined molecular dynamics and diffraction study

2.1 Abstract

Compared to alkali- and alkaline earth-bearing aluminosilicate glasses, the properties of aluminosilicate glasses and melts containing rare-earth elements is less well understood. We performed first-principles and classical MD simulations of Y- and La-bearing aluminosilicate melts and glasses as well as neutron and x-ray diffraction experiments on the glasses in order to elucidate the structure of these materials and the way it changes if the rare-earth element concentration is changed or if Y is replaced by La. It is found that the average coordination numbers of Al, Y and La decrease with increasing rare-earth content. This behavior can be rationalized in terms of the field strengths of the various cations, which, moreover, is seen to be correlated with the width of the coordination shells of oxygen around cations. Finally, we found that, unlike in alkali- and alkaline earth-bearing aluminosilicates, the Al avoidance rule is not satisfied by the melts studied here. This indicates that the traditional picture of charge balancing through mono- and divalent cations in silicate glasses and melts might have to be modified when applied to high field strength cations such as Y and La.

2.2 Introduction

Alkali and alkaline earth bearing (alumino)silicate glasses and melts have been studied extensively, due to their broad range of technological applications and their importance in geoscience. Hence, their structure and properties are relatively well understood (Stebbins et al., 1995; Mysen and Richet, 2005). On the other hand, aluminosilicates containing rare earth elements (REE) are less well studied but have recently attracted considerable interest owing to their remarkable properties and their use in various applications. They exhibit high glass transition temperatures, hardness and refractive indices as well as moderate thermal expansion coefficients (Shelby and Kohli, 1990; Iftekhar et al., 2011). REE-bearing aluminosilicate glasses have been proposed for optical devices (Kohli and Shelby, 1991; Tanabe, 1999), and since rare-earth elements represent analogs for actinides, these glasses have also been studied for applications in nuclear waste storage, and high corrosion resistance in the presence of aqueous fluids was found (Bois et al., 2002).

REE-bearing aluminosilicate glasses have been investigated by a range of experimental techniques,

including nuclear magnetic resonance (NMR) (Schaller and Stebbins, 1998; Clayden et al., 1999; Marchi et al., 2005; Florian et al., 2007; Iftekhar et al., 2009, 2011), infrared spectroscopy (Clayden et al., 1999; Marchi et al., 2005) as well as neutron and x-ray diffraction (Wilding et al., 2002; Pozdnyakova et al., 2008). These techniques provide valuable insight into the local atomic structure of glasses such as coordination environments of the probed elements, glass network structures and vibrational properties. Often, the interpretation of experimental data relies on more or less heuristic assumptions about the atomic structure of the probed material. For instance, Iftekhar et al. (2009) fitted a structural model to the measured NMR peak shifts and were able to extract information about the glass network connectivity from ^{29}Si signals alone. Another example is the interpretation of x-ray and neutron diffraction data: a common approach to obtain bond lengths and coordination numbers is to fit Gaussian peaks to the Fourier-transformed structure factor, i.e. to implicitly assume a specific structural model for the quantitative analysis of experimental data (Wilding et al., 2002; Pozdnyakova et al., 2008).

Molecular dynamics (MD) simulations are a particularly powerful and predictive method to generate complete structural models for disordered systems and to link atomic-scale structure to material properties (Allen and Tildesley, 1987). Apart from supporting the interpretation of experimental data, MD simulations provide complete atomic-scale structures and therefore yield information which is not directly accessible experimentally. To date, there are only a few classical MD studies on REE-bearing aluminosilicate glasses: Du (2009) investigated low-silica (<40 mol%) yttrium aluminosilicates, and Iftekhar et al. (2012) performed MD simulations of Y- and Lu-bearing glasses, with compositions containing less than 50 mol% SiO_2. Very recently, Jaworski et al. (2012) published results from classical MD simulations on aluminosilicate glasses containing La.

Here, we present the results of a combined MD and neutron/x-ray diffraction study on yttrium- and lanthanum-bearing aluminosilicate melts and glasses, RE_2O_3-Al_2O_3-SiO_2 (RE = Y, La), with high silica content (76 mol% SiO_2). Keeping the molar fraction of SiO_2 fixed, the RE/Al ratio was varied between 0.09 and 0.5. We investigated the atomic-scale changes in the structure in response to 1) exchanging Y by La and 2) varying the RE content, i.e. the RE/Al ratio, of the system. A particular focus lies on the coordination environment of Y and La, since these are difficult to probe by the otherwise rather powerful NMR technique (Dupree et al., 1989; Schaller and Stebbins, 1998) and by diffraction experiments (Leydier, 2010). Furthermore, we discuss the structural role of bridging oxygen in the aluminosilicate network and the status of the Al avoidance rule (Loewenstein, 1954) in disordered phases.

Glasses pose a fundamental challenge to the MD method: the latter simulates the motion of the individual atoms in the system over a certain time, and macroscopic quantities are then obtained by averaging over these atomic trajectories. The statistical results are meaningful only to the extent that the phase space available to the system is sufficiently sampled during the simulation, i.e. that all relevant atomic configurations are visited during the MD run. However, structural relaxation in glasses is so slow that it certainly cannot be captured by atomistic simulations, which cover time spans of some tens of nanoseconds at best. Therefore, a simulated glass will be trapped in its initial configuration and will not overcome the energy barriers which separate it from the remaining phase space within the simulation time. In order to circumvent this difficulty, we used two complementary simulation approaches.

Ab-initio or first-principles MD is based on fundamental laws of nature (quantum mechanics) in the form of density functional theory (DFT) (Hohenberg and Kohn, 1964; Kohn and Sham, 1965) and yields a parameter-free description of arbitrary systems of atoms. Although, for practical purposes, some approximations have to be made, it is accurate and highly predictive in many cases (see Gillan et al. (2006) for applications in geoscience). These qualities, however, come at the expense of high computational costs, which limits simulation times to some tens of picoseconds and system sizes to a few hundred atoms at most. For this study, we overcome the problem of insufficient sampling of glass configurations in ab-initio MD simulations by raising the temperature, i.e. by simulating melts as analogs for glasses. Melt structures are expected to represent a reasonable approximation to glass structures, but the effect of temperature is discussed as well. To our knowledge, this is the first ab-initio MD study of

REE-bearing aluminosilicate melts.

The ab-initio simulations not only provide accurate structural information on melts but also serve as a benchmark for classical MD simulations, which constitute the second approach to modeling melt and glass structures. They describe atomic interactions by a classical (as opposed to quantum-mechanical) potential and are less demanding in terms of computation time, but their accuracy has to be tested carefully. Their computational efficiency allows simulated quenching of the melts to glasses at lower rates than can be afforded with ab-initio techniques. The resulting glass structures can then be validated, e.g. by comparison to results from neutron and x-ray diffraction experiments. Conversely, the simulations assist the interpretation of experimental data and provide additional information not directly accessible through experiments. In this study, we perform both ab-initio and classical simulations of REE-bearing aluminosilicate melts and classical molecular dynamics for their glasses.

2.3 Simulation procedure

2.3.1 First-principles molecular dynamics for melts

We performed first-principles, Car-Parrinello molecular dynamics simulations, using the CPMD code (Car and Parrinello, 1985; Marx and Hutter, 2000), of REE-bearing aluminosilicate melts of four different compositions, $REAl_{11}Si_{19}O_{56}$ and $RE_4Al_8Si_{19}O_{56}$, where RE stands for either Y or La. Each simulation cell contained 174 atoms and was repeated periodically in space. Since these melts are considered here, in an approximate way, as an analog for glasses, we chose the dimensions of the simulation cells such as to obtain the experimentally determined density of the respective glass at room temperature, i.e. 2.91 g/cm^3, 2.97 g/cm^3, 2.94 g/cm^3 and 3.09 g/cm^3, respectively (Leydier, 2010).

Interatomic forces were determined within the framework of DFT, and the exchange-correlation functional was evaluated in the local density approximation (LDA). The interaction between ionic cores and valence electrons was described by Troullier-Martins pseudopotentials (Troullier and Martins, 1991). For Y, also the semi-core 4s and 4p electrons were treated explicitly as valence electrons, additionally to the 4d and 5s orbitals. Similarly, for La, also the semi-core 5s and 5p electrons were treated as valence electrons, additionally to the 5d and 6s orbitals. This allows for electric polarizability of the Y^{3+} and La^{3+} ionic cores. The cutoff for the expansion of the electronic wavefunctions into plane waves was 90 Ry, which was found sufficient to give converged results for the average melt structure. We also checked that sampling the Brillouin zone at Γ (i.e. the center) only yielded converged interatomic forces.

The four simulation cells were pre-equilibrated at 3000 K for 50 ps with a classical MD simulation (see section 2.3.2) and further equilibrated for 5 ps using DFT. Data were collected from the following production runs of 10 ps to 15 ps duration. For the Car-Parrinello MD, the fictitious mass of the electronic degrees of freedom was 400 a.u., and the equations of motion were solved with a time step of 0.1 fs. The temperature of 3000 K and the kinetic energy of the fictitious degrees of freedom were controlled by Nosé-Hoover thermostats (Nosé (1984); Hoover (1985)).

2.3.2 Classical molecular dynamics for melts and glasses

For the classical MD simulations of RE-bearing aluminosilicate melts and glasses, the interactions between atoms were described by a polarizable ion model (Wilson and Madden, 1993). Such a model was parameterized for La-free compositions in a previous study (Haigis et al., 2012b) and is extended here to include La. It adds true many-body effects to a simple pair potential through the inclusion of electronic polarization of oxygen, yttrium and lanthanum ions, determined self-consistently at each time step. This improvement with respect to a pure pair potential has been shown to be crucial for an adequate description of oxides (Rowley et al., 1998).

In the polarizable ion model, the potential energy V depends on the set of the ionic coordinates $\{\mathbf{r}\}$ and has the form

$$\begin{aligned} V(\{\mathbf{r}\}) = &\sum_{i<j} \frac{q_i q_j}{r_{ij}} + \sum_{i<j} A_{ij} \exp(-a_{ij} r_{ij}) + \sum_{i<j} B_{ij} \exp(-b_{ij} r_{ij}) \\ &- \sum_{i<j} f_6^{ij}(r_{ij}) \frac{C_6^{ij}}{r_{ij}^6} + V^{\mathrm{pol}}(\{\mathbf{r}\}) \end{aligned} \tag{2.1}$$

The first term on the right side represents the Coulomb interaction, q_i denoting the charge of ion i and r_{ij} the distance between ion i and ion j. At short distances, the overlap of electron shells of two ions leads to a repulsive interaction, described by the second and third term, with model parameters A_{ij}, a_{ij}, B_{ij} and b_{ij}. In fact, the third term is taken to be non-zero only for the La-O interaction and ensures that two ions do not get trapped in an unphysical configuration with a very short distance. The fourth term accounts for dispersion interactions and contains the adjustable parameters C_6^{ij}. The $f_6^{ij}(r_{ij})$ are Tang-Toennies damping functions (Tang and Toennies, 1984) which yield corrections to the asymptotic $1/r_{ij}^6$ behavior at short distances and are defined as

$$f_6^{ij}(r_{ij}) = 1 - \exp(-b_6^{ij} r_{ij}) \sum_{k=0}^{4} \frac{(b_6^{ij} r_{ij})^k}{k!} \tag{2.2}$$

where the b_6^{ij} are parameters of the model. Finally, the last term on the right side of Eq. 2.1 takes into account the polarizability of the ions and contains Coulombic charge-dipole and dipole-dipole interactions as well as a self-energy term describing the energy cost to polarize an ion:

$$\begin{aligned} V^{\mathrm{pol}} = &\sum_{i<j,\alpha} \left[q_i \mu_j^\alpha f_D^{ij}(r_{ij}) - q_j \mu_i^\alpha f_D^{ji}(r_{ji}) \right] T_\alpha^{(1)} \\ &- \sum_{i<j,\alpha,\beta} \mu_i^\alpha \mu_j^\beta T_{\alpha\beta}^{(2)} + \sum_i \frac{|\mu_i|^2}{2\alpha_i} \end{aligned} \tag{2.3}$$

Here, μ_i^α is the Cartesian component of the electric dipole moment of ion i in direction α. The interactions between ionic dipoles and charges q_i are modified at short distances by damping functions $f_D^{ij}(r_{ij})$ which account for additional dipoles induced by short-range interactions (Wilson and Madden, 1993). They are of the same form as in Eq. 2.2, but now contain the parameters b_D^{ij} instead of b_6^{ij}. We also use the short-hand notation $T_{\alpha\beta\ldots}^{(n)} = \nabla_\alpha \nabla_\beta \cdots 1/r_{ij}$ to denote the multipole interaction tensors, where the superscript gives the order of the derivative (Stone, 1996).

The polarizable ion model for the system Y-Ca-Al-Si-O has been parameterized in a previous study by force-, dipole- and stress-matching with respect to density functional theory (DFT) results and has been applied successfully to silicate melts (Haigis et al., 2012b). For the present work, we extended the model by adding interaction parameters for La while keeping the established parameters for Y, Al, Si and O. Methodological details concerning the parameterization can be found in Salanne et al. (2012). As a reference for the matching procedure for the La parameters, five configurations of $La_4Al_8Si_{19}O_{56}$ melt were chosen on which we performed static DFT calculations, using the same settings as described in section 2.3.1, except for the higher plane-wave cutoff of 140 Ry, which ensures full convergence of the DFT reference calculations. All parameters of the polarizable ion model are listed in Table 2.1.

The aim of the classical MD simulations is to generate structural models for four RE-bearing aluminosilicate glasses instead of melts, which can then be validated by comparison to diffraction experiments. In order to circumvent the problem of insufficient phase-space sampling, we first performed classical high-temperature simulations of melts of the four compositions, which display sufficiently fast dynamics to explore the entire phase space. Then 100 configurations were picked from each melt trajectory and

i–j	O–O	Si–O	Al–O	La–O	Y–O	La–La	Y–Y
q_i	-2	+4	+3	+3	+3		
A_{ij}	5328.3	44.624	39.404	49.165	95.048		
a_{ij}	3.1526	1.6513	1.6413	1.4658	1.6813		
B_{ij}				10^5			
b_{ij}				4.2			
C_6^{ij}	52.461			45.041	23.763	41.213	12.504
b_6^{ij}	2.7370			1.0	1.4995	1.0	0.67066
α_i	10.754			7.3962	3.5475		
b_D^{ij}	0.0	1.6489	1.5573	1.3460 (La–O)/ 3.2197 (O–La)	1.5056 (Y–O)/ 3.3585 (O–Y)		

Table 2.1: Interaction parameters, see eqs. (2.1), (2.2) and (2.3), in atomic units. Interactions not listed or left blank here, e.g., short-range repulsion for Si–Si, are taken to be absent in the model. Since $b_D^{ij} \neq b_D^{ji}$ in general, both parameters are listed.

used as starting configurations for subsequent quenching to room temperature. For each composition, we thus obtained a large set of different glass structures which were used for structural analysis.

In detail, we set up four simulation cells, each containing 174 atoms, with periodic boundary conditions and the same compositions and densities as for the ab-initio MD (section 2.3.1). Starting from final atomic configurations of ab-initio simulations, the cells were further equilibrated for 10 ps at 3000 K, with a time step of 1 fs. The temperature was controlled by means of a Nosé-Hoover thermostat (Nosé, 1984; Hoover, 1985). Equilibration was followed by production runs of 50 ps duration with melts at 3000 K, from which we picked 100 starting configurations for the quench runs. During each of the latter, temperature was lowered by 100 K every 2 ps, down to 300 K, which corresponds to a quench rate of $5 \cdot 10^{13}$ K/s. Analysis was based on the last 1 ps of each quench run, and for each composition, an average over all the resulting glasses is taken. The duration of all the quench runs together amounts to 22.4 ns.

We also checked that the results of the analysis are not affected by the finite size of the simulation cell: for the composition $La_4Al_8Si_{19}O_{56}$, we simulated a glass using a simulation cell of eight times the original volume, and no significant changes were observed in the parameters discussed in this study, i.e. in the inter-atomic distances, coordination numbers and the widths of coordination shells. However, we deliberately do not discuss the large-scale network structure of the glasses (e.g., rings formed by tetrahedrally coordinated species), because these features are expected to be more heavily influenced by the periodic boundary conditions used here, and probably also by the rather high quench rate (Drewitt et al., 2012).

2.4 Results

2.4.1 Ab-initio MD: first coordination shell in melts

From the trajectories of the ab-initio MD simulations for each composition, the coordination environment of the cations has been extracted. Fig. 2.1 and Fig. 2.2 show the radial distribution functions $g_{XO}(r)$ (X = Y/La, Al, Si, O) for the Y-bearing and the La-bearing melts, respectively. The average coordination number of a cation X is calculated as the average number of oxygen ions around the cation within a cutoff radius r_{cut}^{XO}, which is given by the distance where the radial distribution function $g_{XO}(r)$ for the pair X–O takes its first minimum. The minimum has been determined by a polynomial fit to the minimum region and depends (weakly) on composition. This dependence results from the change in shape of the first

coordination shell which accompanies variations in composition.

The average cation-oxygen bond length d_{XO} is calculated as the average distance between a cation X and oxygen for pairs closer than r_{cut}^{XO}. We also determined the first maximum $\hat{d}_{XO}$ of the function $r^2 g_{XO}(r)$, i.e. the most probable $X-O$ bond length, using a polynomial fit to the maximum region. This maximum does not coincide with the average bond length in general, and the difference between the two quantities is a measure for the radial asymmetry of the first coordination shell. Finally, the standard deviation σ of the distribution of cation-oxygen bond lengths was determined, giving a measure for the width of the coordination shell. In Table 2.2, we list the results characterizing the first coordination shell of the different cations.

Table 2.2: Ab-initio MD results for the first coordination shell around cations in melts: cutoff radius r_{cut} for cation-oxygen pairs, average coordination number CN, average bond length d, most probable bond length $\hat{d}$ and standard deviation σ of cation-oxygen bond lengths (a measure for the width of the coordination shell).

cation	r_{cut} (Å)	CN	d (Å)	$\hat{d}$ (Å)	σ (Å)
$YAl_{11}Si_{19}O_{56}$ melt					
Si	2.32	4.1	1.69	1.63	0.151
Al	2.61	4.7	1.93	1.78	0.249
Y	3.25	7.9	2.53	2.26	0.359
$Y_4Al_8Si_{19}O_{56}$ melt					
Si	2.31	4.1	1.69	1.63	0.150
Al	2.57	4.5	1.91	1.78	0.232
Y	3.22	7.1	2.50	2.25	0.348
$LaAl_{11}Si_{19}O_{56}$ melt					
Si	2.36	4.2	1.70	1.63	0.161
Al	2.60	4.7	1.93	1.78	0.243
La	3.41	8.2	2.72	2.45	0.376
$La_4Al_8Si_{19}O_{56}$ melt					
Si	2.38	4.1	1.69	1.63	0.153
Al	2.55	4.3	1.89	1.77	0.223
La	3.44	7.9	2.71	2.43	0.388

As a result, it is found that the coordination shells of the different cations exhibit different sensitivities to changes in melt composition: the first-shell environment of Si is virtually the same for all melts, with a coordination number around 4.1, a Si-O average bond length around 1.69 Å and a most probable bond length of 1.63 Å. On the other hand, the coordination of Al shows a slight, but systematic variation with melt composition: for a given REE (Y or La), the coordination of Al by oxygen decreases for increasing RE content, and so does the average Al-O bond length. Moreover, the Al coordination number is smaller in the La-rich melt than in the corresponding Y-rich melt. Finally, also the coordination environments of Y and La are clearly sensitive to compositional changes. Coordination numbers decrease with increasing RE content, and for Y, this change is accompanied by a shortening of the bonds to the nearest oxygen ions.

The average coordination numbers listed in Table 2.2 are the mean of a range of coordination numbers occurring in the melt structure. The distribution of different coordination environments of Y and La for given glass compositions is shown in Fig. 2.3. The coordination numbers span a wide range, with significant contributions coming from 5- to 10-fold coordination of the RE cation by oxygen. With increasing RE content, the distributions shift to lower coordination numbers. A similar plot for the coordination of Al in the different melts is shown in Fig. 2.4. Most Al atoms are 4-, 5- or 6-fold coordinated

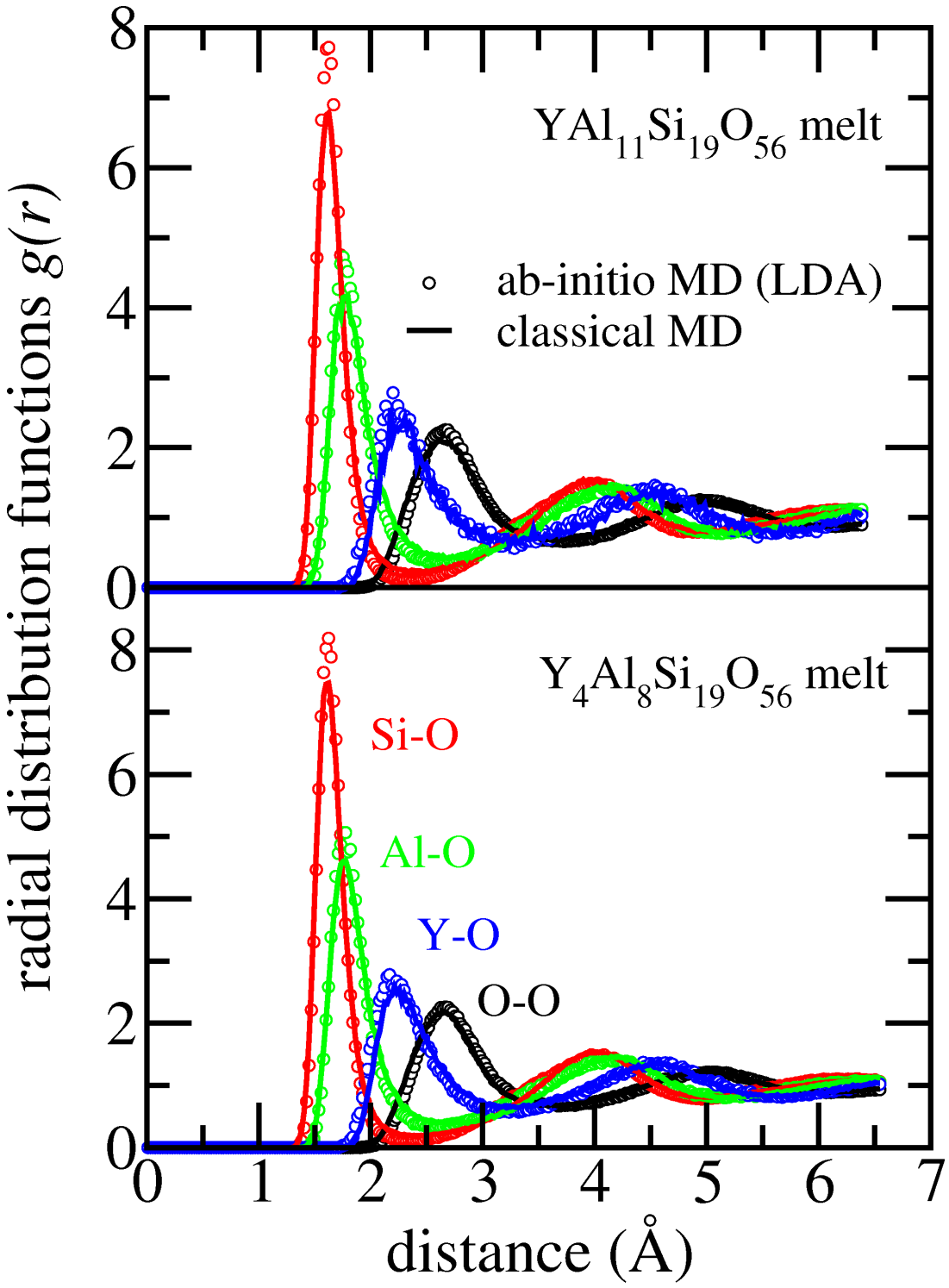

Figure 2.1: Radial distribution functions $g(r)$ for O-O and cation-O pairs in $YAl_{11}Si_{19}O_{56}$ melt (upper panel) and $Y_4Al_8Si_{19}O_{56}$ melt (lower panel), at 3000 K. Circles: ab-initio MD, full lines: classical MD (see section 2.4.3).

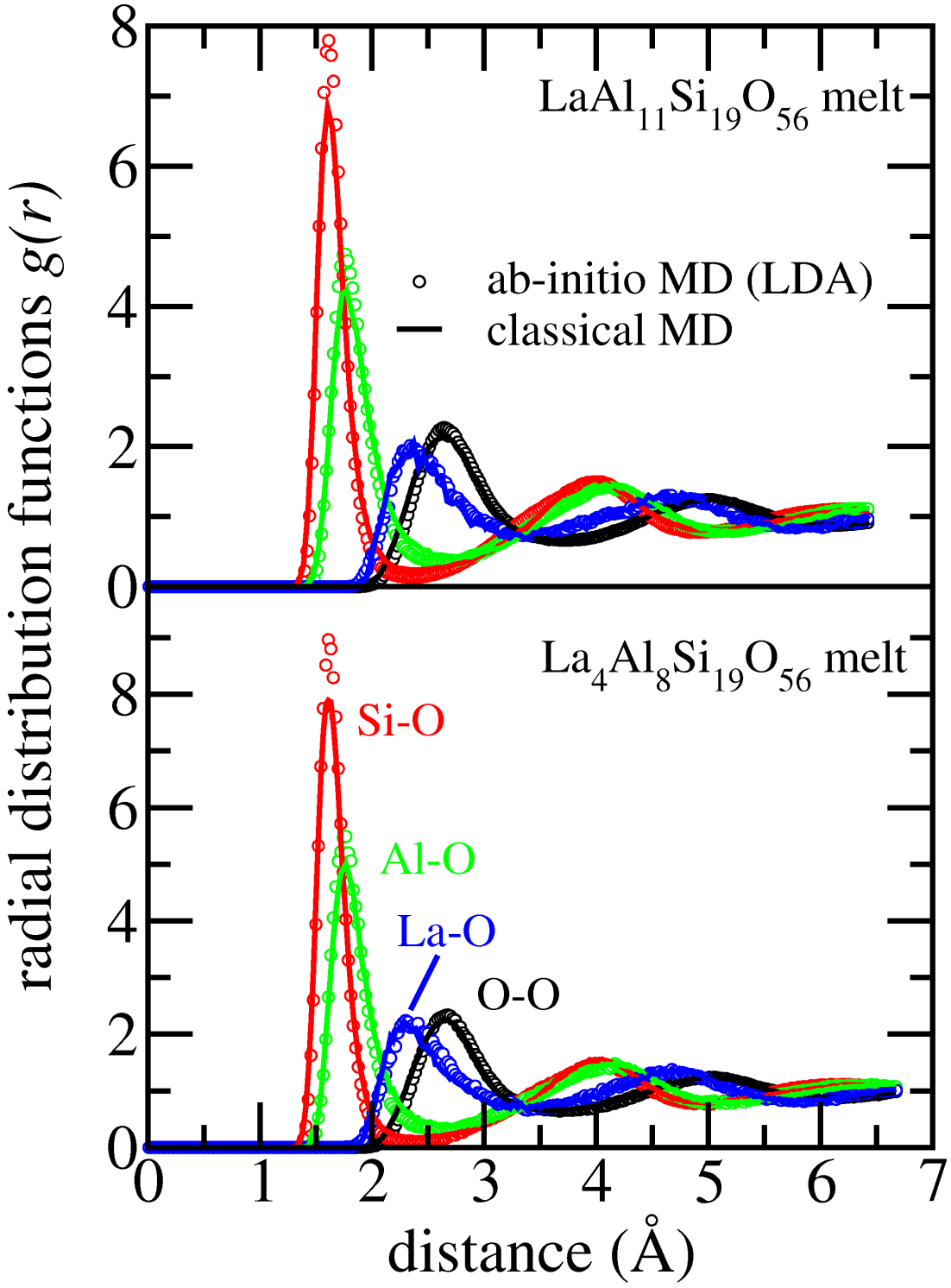

Figure 2.2: Radial distribution functions $g(r)$ for O-O and cation-O pairs in $LaAl_{11}Si_{19}O_{56}$ melt (upper panel) and $La_4Al_8Si_{19}O_{56}$ melt (lower panel), at 3000 K. Circles: ab-initio MD, full lines: classical MD (see section 2.4.3).

by oxygen, and two trends in the coordination distribution are observed: first, the distribution shifts to lower coordination numbers for increasing RE content, and second, the distribution is shifted to lower numbers if Y is replaced by La, especially for the RE-rich compositions.

2.4.2 Ab-initio MD: medium range order in melts

The medium range order of silicate melts and glasses is commonly discussed in terms of the tetrahedral network formed by fourfold coordinated Si and Al, and its perturbation by network modifiers (Mysen and Richet, 2005). In the analysis of our first-principles MD data, we follow this line, putting an emphasis on the various oxygen species which link the building blocks of the structure. Tetrahedrally coordinated Si and Al are counted as network formers (T), and oxygen is considered bridging (BO) if it links exactly two such tetrahedra. A terminal oxygen, which is bonded to only one T species, is referred to as non-bridging (NBO). Note that according to this terminology, an oxygen atom linking, for instance, a tetrahedrally coordinated Si and a fivefold coordinated Al atom is counted as non-bridging. The ratio NBO/T is a measure for the depolymerization of the melt or glass network. Finally, an oxygen atom which belongs simultaneously to three coordination tetrahedra around T is termed an oxygen tricluster. Note that there are oxygen atoms which do not fall into any of the mentioned categories, e.g. oxygen bonded to two fivefold coordinated Al atoms. The results of this analysis are listed in table 2.3. Whereas Si occurs predominantly as tetrahedrally coordinated network former T, less than half of Al is in T configuration in the RE-poor melts. NBO/T values are larger than 1 for all compositions, which indicates a substantial depolymerization of the network. Small amounts of oxygen triclusters (<5%) are observed throughout.

In aluminosilicate *minerals*, the distribution of tetrahedrally coordinated Si and Al in the crystal structure is subject to the Al avoidance or Loewenstein rule which states that due to their excess negative charge, pairs of Al tetrahedra linked by BO are strongly unfavored, and instead alternation of Si and Al tetrahedra occurs in the crystal structure (Loewenstein, 1954). Since silicate melts and glasses are composed of the same tetrahedral building blocks, it may be conjectured that they also obey this ordering principle. We tested if the rule applies to the amorphous phases studied here by checking the distribution of bridging oxygen, T-O-T, among the motifs Si-O-Si, Si-O-Al and Al-O-Al. It is instructive to compare the BO distribution actually found in the melt to the random distribution, which would be expected simply on the basis of the abundances of tetrahedral Si and Al, in the absence of any ordering rule. This random distribution is found as follows: if there are N_T tetrahedrally coordinated species of type T and $N_{T'}$ of type T' ($T, T' \in \{\mathrm{Si}, \mathrm{Al}\}$) in the simulation cell, then the number $p_{T,T'}$ of possible pairs of tetrahedra T, T' linked by bridging oxygen is

$$p_{T,T'} = \frac{1}{2} N_T (N_{T'} - \delta_{TT'}) \tag{2.4}$$

where $\delta_{TT'}$ is 1 for $T = T'$, i.e. for like pairs (Si-O-Si or Al-O-Al), and 0 otherwise. The factor 1/2 corrects for double counting of pairs, and the number of unlike pairs (Si-O-Al) is understood to be the sum $p_{\mathrm{Si,Al}} + p_{\mathrm{Al,Si}} = 2p_{\mathrm{Si,Al}} = N_{\mathrm{Si}} N_{\mathrm{Al}}$. For a random distribution, the fraction of BO linking T and T' would then be

$$x_{\mathrm{BO}}^{\mathrm{rand}}(T - O - T') = \frac{(2 - \delta_{TT'}) p_{T,T'}}{\sum_{T,T'} p_{T,T'}} \tag{2.5}$$

The results concerning the BO statistics are given in table 2.3, indicating a near-random distribution of BO, i.e. a considerable Al/Si disorder.

2.4.3 Classical MD: first coordination shell in melts

The reliability of the classical interaction potential described in section 2.3.2 can be assessed by comparison of its predictions either to ab-initio results or to experimental data. Here, we first check melt

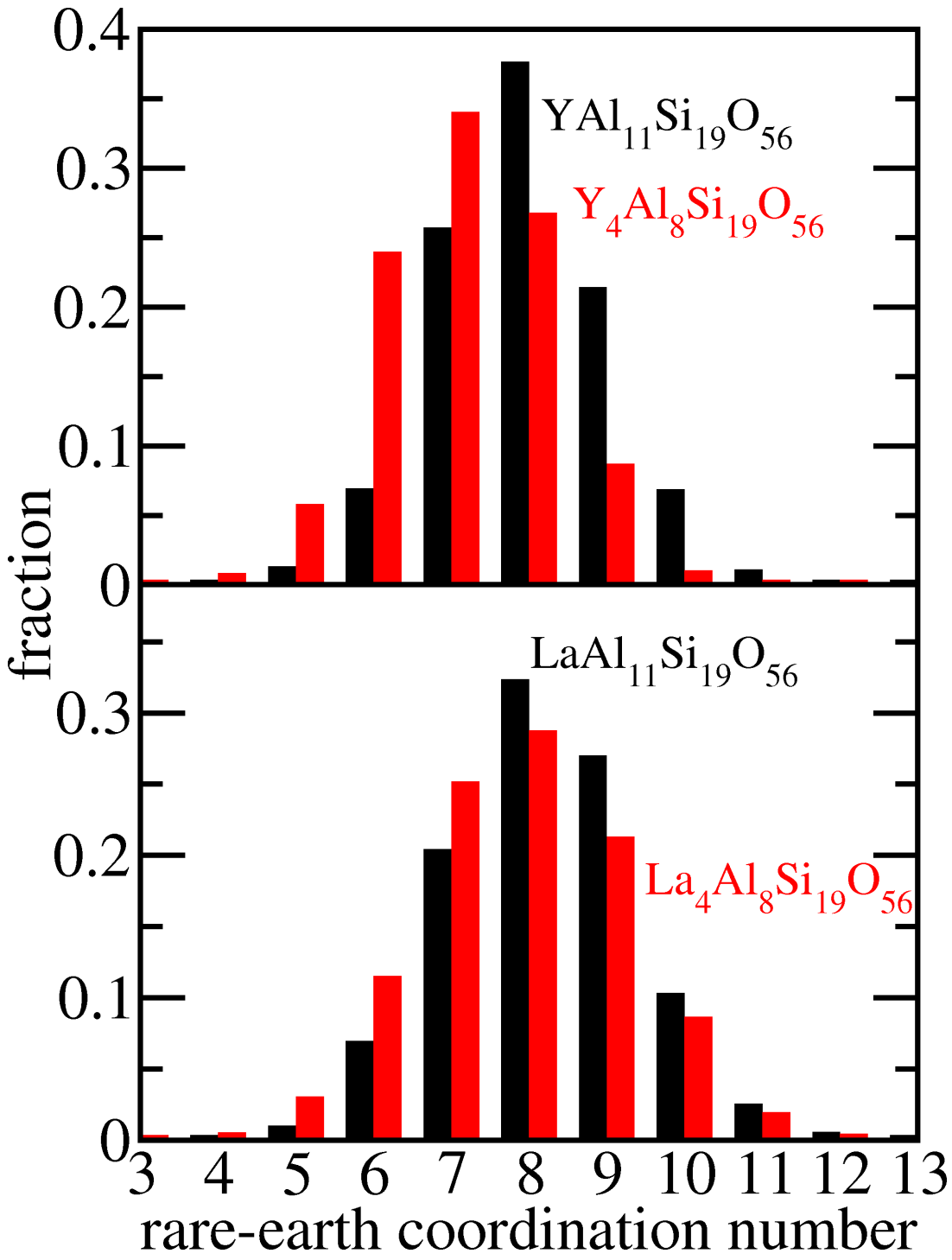

Figure 2.3: Ab-initio MD: distribution of coordination numbers of Y and La as a function of melt composition, with low (black) and high (red) RE content.

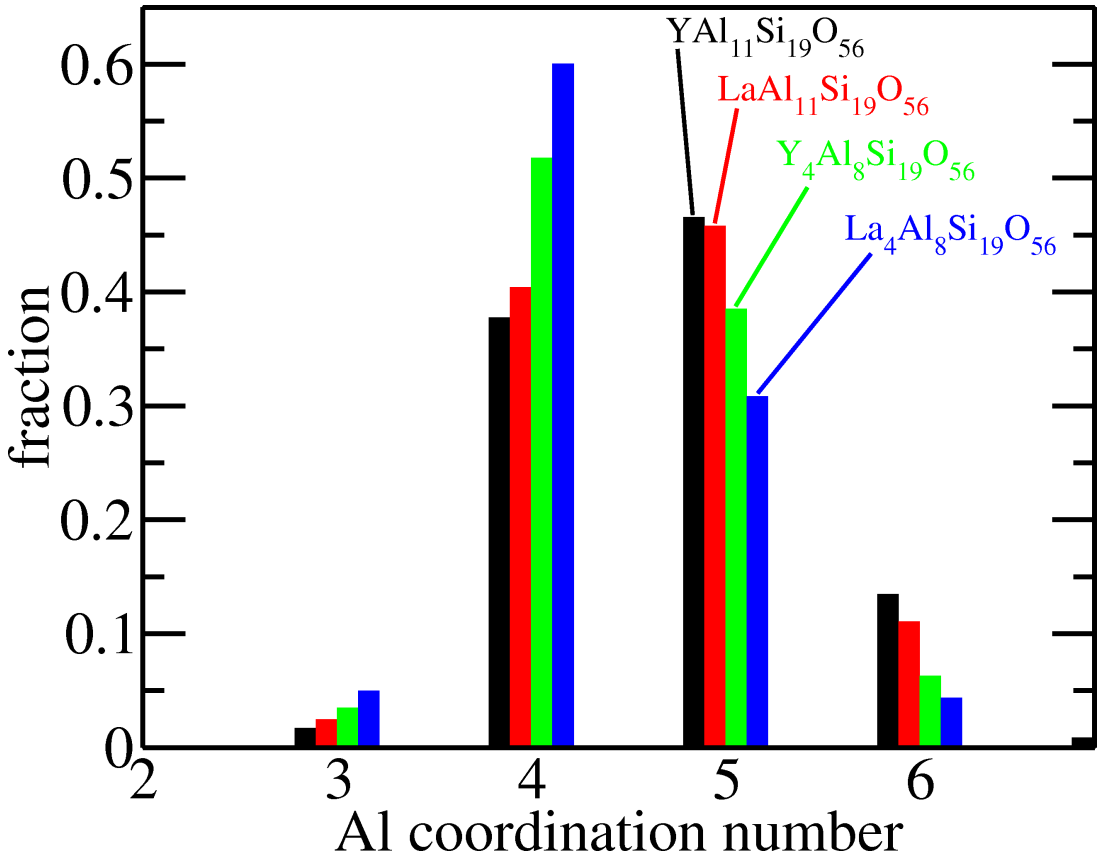

Figure 2.4: Ab-initio MD: distribution of coordination numbers of Al as a function of melt composition.

Table 2.3: Parameters concerning the melt network structure: the fractions $[Si_{IV}]$/[Si] and $[Al_{IV}]$/[Al] of fourfold coordinated Si and Al, respectively, determine the abundance of tetrahedrally coordinated species, and NBO/T is the ratio of non-bridging oxygen to tetrahedrally coordinated species. The fraction of bridging oxygen linking T and T' is denoted by x_{BO}(T-O-T'), and the BO fractions expected for a random distribution by $x_{\mathrm{BO}}^{\mathrm{rand}}$(T-O-T')

	$YAl_{11}Si_{19}O_{56}$	$Y_4Al_8Si_{19}O_{56}$	$LaAl_{11}Si_{19}O_{56}$	$La_4Al_8Si_{19}O_{56}$
$[Si_{IV}]$/[Si]	0.851	0.879	0.817	0.877
$[Al_{IV}]$/[Al]	0.377	0.517	0.404	0.600
NBO/T	1.145	1.123	1.179	1.028
x_{BO}(Si-O-Si)	0.633	0.617	0.598	0.551
x_{BO}(Si-O-Al)	0.326	0.345	0.351	0.423
x_{BO}(Al-O-Al)	0.041	0.038	0.052	0.025
$x_{\mathrm{BO}}^{\mathrm{rand}}$(Si-O-Si)	0.630	0.638	0.600	0.599
$x_{\mathrm{BO}}^{\mathrm{rand}}$(Si-O-Al)	0.333	0.326	0.355	0.355
$x_{\mathrm{BO}}^{\mathrm{rand}}$(Al-O-Al)	0.038	0.036	0.045	0.046
$[O_{\mathrm{tri}}]$/[O]	0.022	0.024	0.024	0.046

structures derived from classical MD at 3000 K against the ones obtained from Car-Parrinello simulations (see section 2.4.1). A comparison with diffraction data will be made in section 2.4.4. The radial distribution functions for X-O pairs (X = Y/La, Al, Si, O) are plotted along with the DFT results in Figs. 2.1 and 2.2. In Table 2.4, we list structural parameters of the four melts as obtained from classical MD, which can be compared to the ab-initio results in Table 2.2. While for the Y-O parameters, fair agreement is found with first-principles data, the drop of the most probable La-O distance by over 0.1 Å is not seen to this extent in the ab-initio simulations.

2.4.4 Classical MD and diffraction experiments on glasses

We turn now to the simulated *glass* structures obtained from multiple quenches of melt structures to 300 K. In order to compare simulation results to experiments, it is necessary to convert the structural information contained in the classical MD trajectories to experimentally observable quantities, i.e. to neutron end x-ray (static) structure factors $S_N(Q)$ and $S_X(Q)$, respectively. These can be written as a weighted sum of Faber-Ziman partial structure factors $S_{\alpha\beta}(Q)$, each corresponding to a pair of elements $\alpha,\beta \in$ {RE, Al, Si, O} (Faber and Ziman, 1965):

$$S(Q) = \frac{1}{\left(\sum_\alpha c_\alpha b_\alpha\right)^2} \sum_{\alpha,\beta} c_\alpha c_\beta \, b_\alpha(Q) b_\beta(Q) (S_{\alpha\beta}(Q) - 1) \tag{2.6}$$

where Q is the magnitude of the scattering vector $\mathbf{Q}$, c_α denotes the concentration of element α and b_α its neutron or x-ray scattering length. The latter is Q-dependent. Scattering lengths are tabulated in Sears (1992) and Ibers and Hamilton (1974). The partial structure factors are the Fourier transforms of the partial radial distribution functions $g_{\alpha\beta}(r)$, which in turn are obtained from the MD simulations:

$$S_{\alpha\beta}(Q) - 1 = n_0 \int dr \, \left(g_{\alpha\beta}(r) - 1\right) \exp(-i\mathbf{Q}\cdot\mathbf{r}) \tag{2.7}$$

with the atomic number density n_0 of the glass. The partial radial distribution functions for all glass compositions, obtained from classical MD simulations, have been converted to neutron and x-ray structure factors by use of Eq. 2.7 and Eq. 2.6, and the structure factors are compared to the experimental ones in Figs. 2.5 to 2.8. The agreement between experiment and simulation is good in the case of neutron diffraction, and the discrepancies in the x-ray structure factors for the RE-rich glasses will be discussed in section 2.5.1.

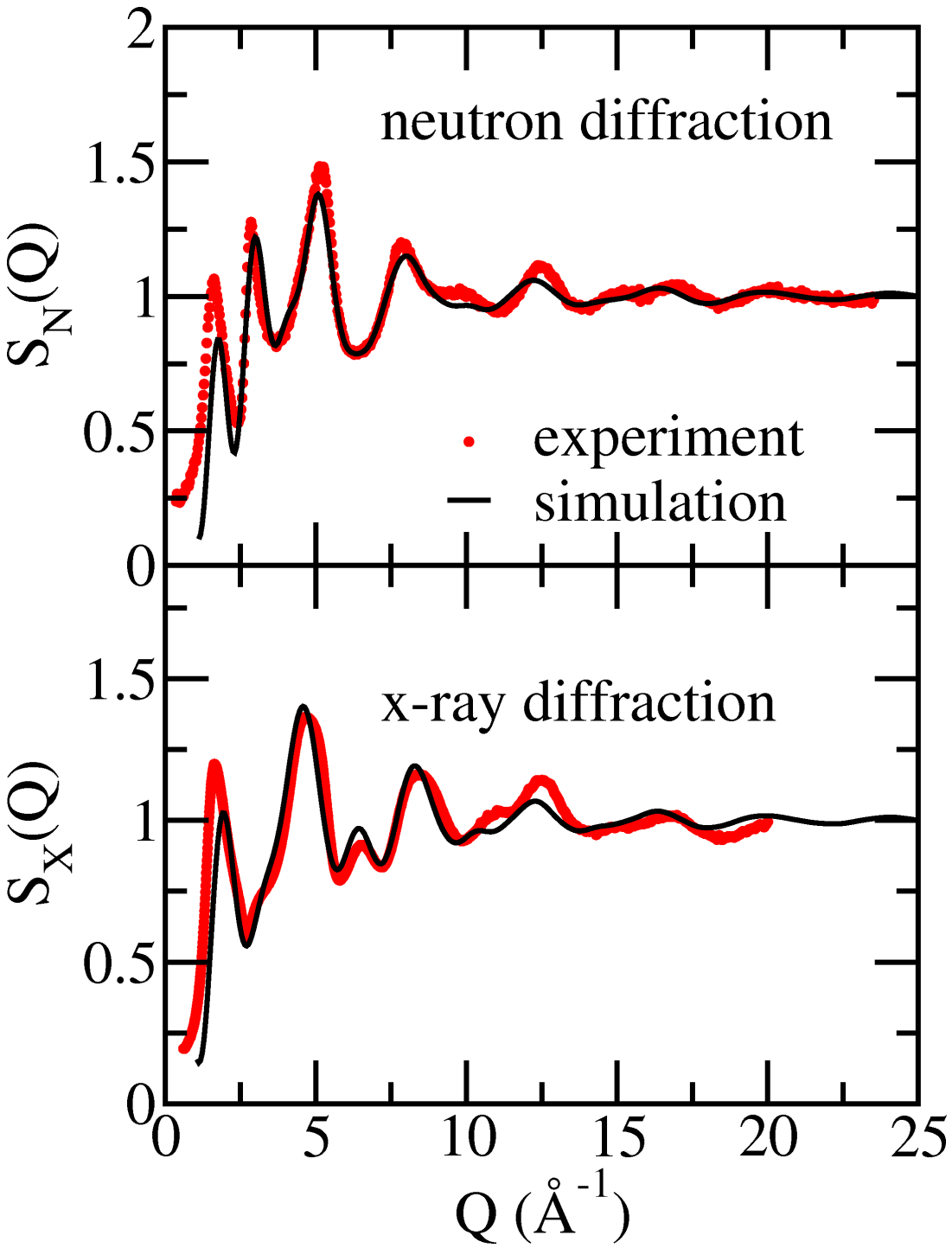

Figure 2.5: Neutron (upper panel) and x-ray (lower panel) structure factors $S(Q)$ of $YAl_{11}Si_{19}O_{56}$ glass. Red circles: experiment (Leydier, 2010), black lines: MD simulation.

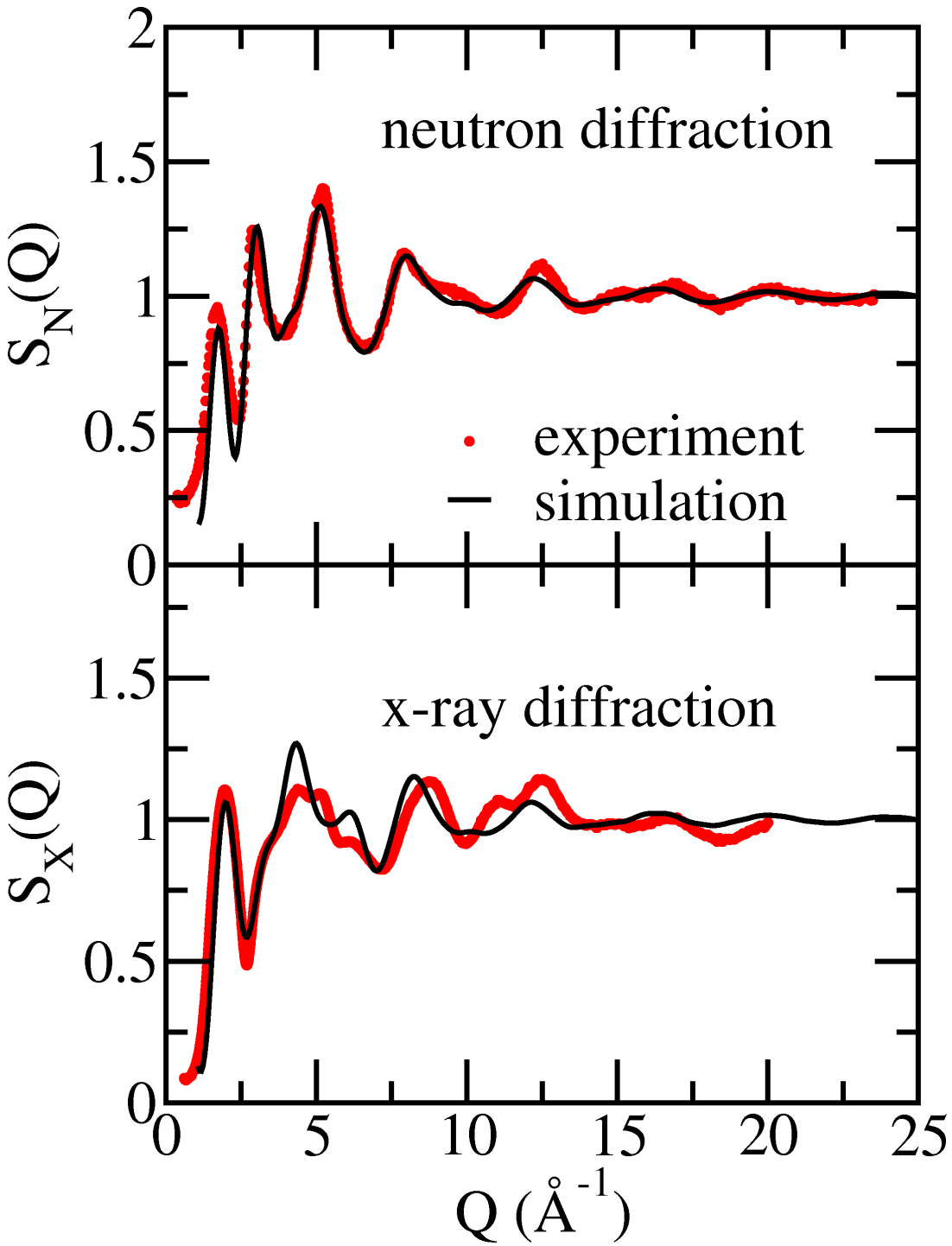

Figure 2.6: Neutron (upper panel) and x-ray (lower panel) structure factors $S(Q)$ of $Y_4Al_8Si_{19}O_{56}$ glass. Red circles: experiment (Leydier, 2010), black lines: MD simulation.

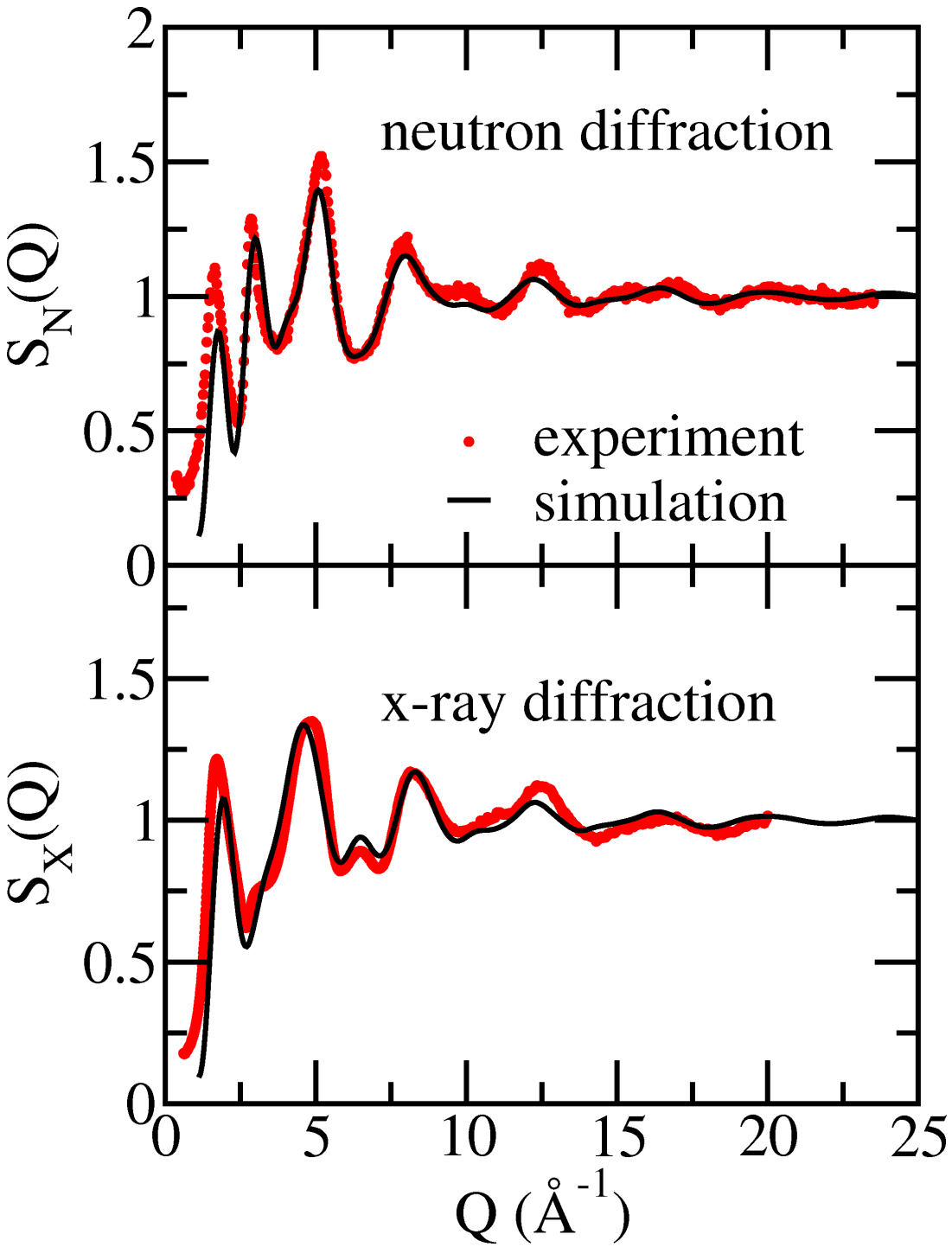

Figure 2.7: Neutron (upper panel) and x-ray (lower panel) structure factors $S(Q)$ of $LaAl_{11}Si_{19}O_{56}$ glass. Red circles: experiment (Leydier, 2010), black lines: MD simulation.

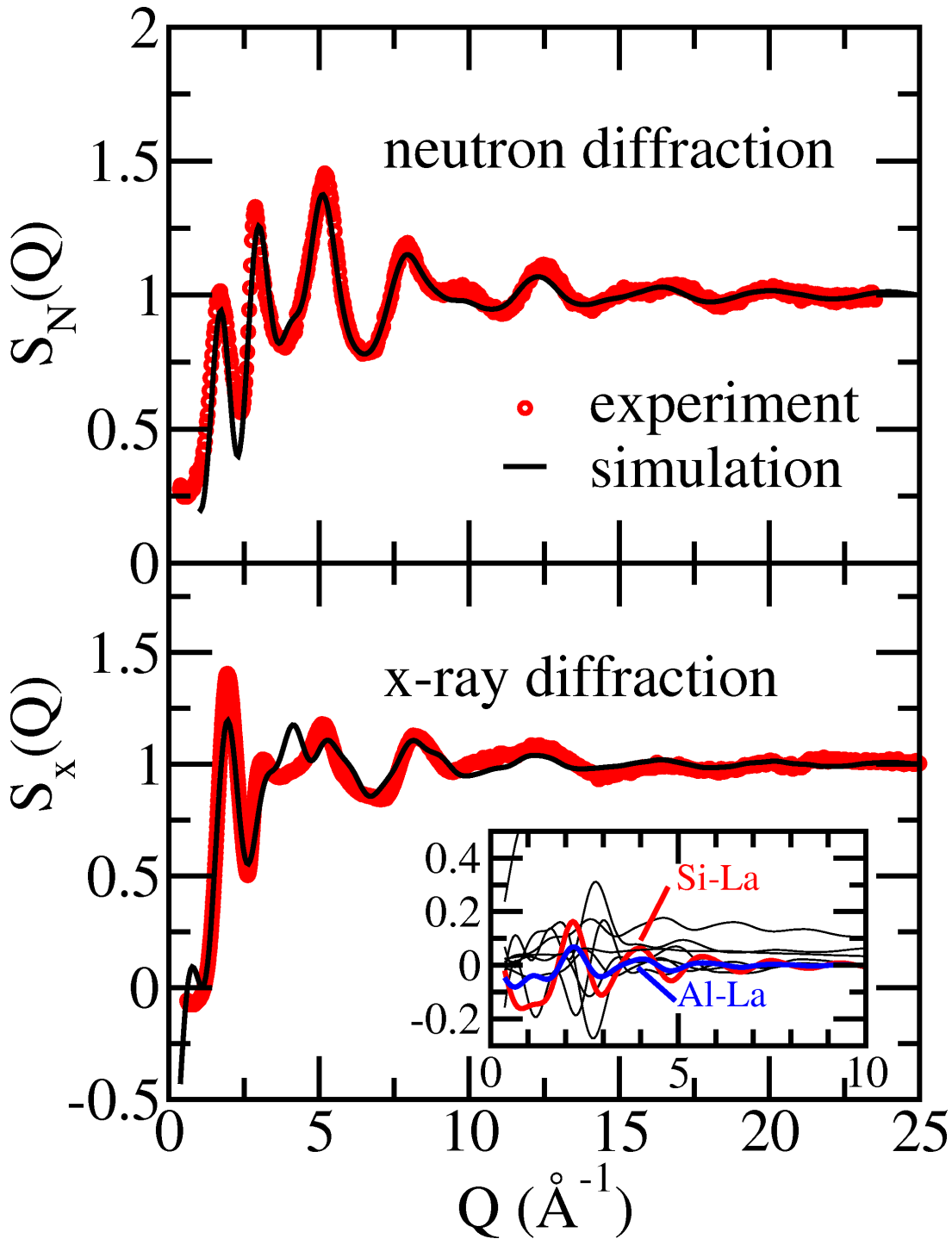

Figure 2.8: Neutron (upper panel) and x-ray (lower panel) structure factors $S(Q)$ of $La_4Al_8Si_{19}O_{56}$ glass. Red circles: experiment (Leydier, 2010), black lines: MD simulation. The inset in the lower panel shows the weighted partial structure factors $S_{\alpha\beta}(Q)$, see eqs. 2.6 and 2.7, obtained from simulation. It highlights the Si-La (red) and Al-La (blue) correlations, which both peak around 4 Å^{-1}.

Table 2.4: Classical MD results for the first coordination shell around cations in melts: cutoff radius r_{cut} for cation-oxygen pairs, average coordination number CN, average bond length d, most probable bond length $\hat{d}$ and standard deviation σ of cation-oxygen bond lengths (a measure for the width of the coordination shell).

cation	r_{cut} (Å)	CN	d (Å)	$\hat{d}$ (Å)	σ (Å)
$YAl_{11}Si_{19}O_{56}$ melt					
Si	2.40	4.3	1.72	1.63	0.197
Al	2.72	5.1	2.00	1.80	0.294
Y	3.25	7.5	2.57	2.31	0.351
$Y_4Al_8Si_{19}O_{56}$ melt					
Si	2.40	4.2	1.71	1.63	0.188
Al	2.71	4.9	1.97	1.79	0.284
Y	3.27	7.3	2.55	2.29	0.357
$LaAl_{11}Si_{19}O_{56}$ melt					
Si	2.37	4.3	1.72	1.63	0.191
Al	2.76	5.2	2.01	1.79	0.308
La	3.32	7.5	2.67	2.46	0.353
$La_4Al_8Si_{19}O_{56}$ melt					
Si	2.38	4.2	1.70	1.63	0.177
Al	2.72	4.8	1.96	1.78	0.285
La	3.33	7.0	2.65	2.35	0.367

2.4.5 Classical MD: first coordination shell in glasses

To conclude the results section, we give the parameters describing the first coordination shell around cations for all four glass compositions in Table 2.5. Also listed are coordination numbers and bond lengths extracted from the neutron diffraction experiments by fitting Gaussian peaks to the Fourier-transformed structure factor (Leydier, 2010). This procedure yields coordination numbers for Si and Al to within 0.5 only. Coordination numbers of Y and La could not be obtained from the diffraction experiments because the first peaks in the respective partial radial distribution functions were superposed by others and could not be unambiguously resolved.

2.5 Discussion

2.5.1 Assessment of the classical interaction potential

The accuracy of the melt and glass structures obtained from classical MD simulations is assessed by comparison to ab-initio-derived melt structures and to experimental diffraction data for the glasses. Figs. 2.1 and 2.2 demonstrate an overall good agreement between classical and DFT simulations for the partial radial distribution functions in the four investigated melts. The peaks corresponding to the first coordination shells of oxygen around Si and Al come out somewhat lower in the classical MD for all compositions, and they extend to a slightly higher distance (more so for Al-O than for Si-O). For the $La_4Al_8Si_{19}O_{56}$ melt, the classically simulated La-O peak falls off faster on the high-distance side than the one obtained from the ab-initio simulation. These slight deviations lead to some differences in the structural parameters describing the first coordination shells around cations, listed in Table 2.2 (ab initio) and Table 2.4 (classical): coordination numbers for Si are overestimated by the classical simulations by up to 0.2, and Al coordination numbers by up to 0.5, whereas in the $La_4Al_8Si_{19}O_{56}$ melt, the La coordination number is underestimated by 0.9 (13%) with respect to the ab-initio result. On the other hand, average cation-

Table 2.5: Classical MD and neutron diffraction results for the first coordination shell around cations in glasses: cutoff radius r_{cut} for cation-oxygen pairs, average coordination numbers CN, experimental CN^{exp}, average bond length d, most probable bond length $\hat{d}$, peak position $\hat{d}^{exp}$ of $rg_{\alpha\beta}(r)$ derived from experiments and standard deviation σ of cation-oxygen bond lengths.

cation	r_{cut}	CN	CN^{exp}	d (Å)	$\hat{d}$ (Å)	$\hat{d}^{exp}$ (Å)	σ (Å)
			$YAl_{11}Si_{19}O_{56}$ glass				
Si	2.23	4.2	4.0 ±0.5	1.68	1.64	1.62 ±0.03	0.109
Al	2.65	5.2	4.3 ±0.5	1.94	1.81	1.80 ±0.03	0.210
Y	3.48	7.6	-	2.51	2.35	2.30 ±0.03	0.256
			$Y_4Al_8Si_{19}O_{56}$ glass				
Si	2.25	4.2	4.1 ±0.5	1.67	1.64	1.62 ±0.03	0.104
Al	2.72	5.0	4.1 ±0.5	1.92	1.80	1.81 ±0.03	0.219
Y	3.20	7.3	-	2.50	2.33	2.32 ±0.03	0.272
			$LaAl_{11}Si_{19}O_{56}$ glass				
Si	2.19	4.2	4.0 ±0.5	1.67	1.63	1.62 ±0.03	0.101
Al	2.63	5.1	4.3 ±0.5	1.93	1.81	1.81 ±0.03	0.205
La	3.33	7.9	-	2.65	2.46	2.51 ±0.03	0.309
			$La_4Al_8Si_{19}O_{56}$ glass				
Si	2.25	4.1	4.2 ±0.5	1.66	1.64	1.62 ±0.03	0.095
Al	2.58	4.8	4.1 ±0.5	1.89	1.79	1.82 ±0.03	0.180
La	3.32	7.3	-	2.62	2.42	2.51 ±0.03	0.309

oxygen bond lengths agree well for both simulation methods, the largest deviation being 0.08 Å for Al-O bonds in $LaAl_{11}Si_{19}O_{56}$ melt. Note, moreover, that classical and ab-initio simulations yield the same trends for structural variations in response to compositional changes: RE and Al coordination numbers decrease with increasing RE content, and in the case of Al, this decrease is even quantitatively the same for both simulation methods.

As another test of the classical interaction potential, we compare neutron and x-ray structure factors derived from simulated glass structures to experimental data in Figs. 2.5 to 2.8. The simulated and the experimental neutron structure factors are found in good agreement in terms of peak positions, and in most cases also with regard to peak intensities (upper panels). The overall agreement of the x-ray structure factors (lower panels) is good as well for the RE-poor compositions, but less satisfactory for $Y_4Al_8Si_{19}O_{56}$ (Fig. 2.6) and $La_4Al_8Si_{19}O_{56}$ (Fig. 2.8).

In the case of $La_4Al_8Si_{19}O_{56}$ glass, a rather pronounced peak is observed in the simulated x-ray structure factor at 4 $Å^{-1}$ which is only visible as a shoulder in the experiment. By analysis of the partial structure factors obtained from simulation, this peak is attributed to Si-La and Al-La correlations (inset of Fig. 2.8), which seem to be overestimated by the classical simulation. The reason why the discrepancy between simulation and experiment shows up in the x-ray but not in the neutron structure factor is that La has a large x-ray scattering length $b(Q)$, due to the large number of electrons. Therefore, correlations involving La make a large contribution to the total x-ray structure factor. An analogous analysis has been performed for the simulated x-ray structure factor of $Y_4Al_8Si_{19}O_{56}$ (Fig. 2.6). Again, the greater intensity of the peak around 4.3 $Å^{-1}$ in the simulation can be explained by peaks in the simulated Si-Y and Al-Y partial structure factors (not shown). For the same composition, there is another discrepancy between simulation and experiment between 11 $Å^{-1}$ and 14 $Å^{-1}$. In the Q range above 10 $Å^{-1}$, all simulated partial structure factors are essentially flat except for the one representing Si-O correlations, which still exhibits oscillations. The additional features seen in the experiment in this Q region indicate that there are additional structural features in the glass which are not seen in the simulation.

From the preceding discussion, we conclude that the classical interaction potential yields overall reliable melt and glass structures, with the following caveats: the coordination numbers of Al seem too large by up to 0.5, and those of La seem to be on the low side. Moreover, classically simulated glasses appear to over-emphasize some structural features beyond the nearest-neighbor range (correlations between network formers and RE cations). However, we stress that the first-shell environment of Y in melts and glasses is described well, and so is the aluminosilicate network structure, as can be seen from the neutron and x-ray structure factors of the RE-poor glasses. Also the cation-oxygen bond lengths in the glasses as described by $\hat{d}$ agree with those derived from the diffraction data within the experimental uncertainty in most cases. Moreover, structural trends in response to compositional changes are predicted correctly by the model.

2.5.2 Melt vs. glass and simulated quenching

When using simulated melts as an analog for glasses, the effect of temperature on the structures has to be discussed. The Al coordination numbers found in the ab-initio and classical MD simulations of RE-bearing aluminosilicate melts are significantly larger than the ones extracted from the diffraction experiments (Table 2.5) and from experiments using NMR or infrared spectroscopy on glasses of similar compositions (Schaller and Stebbins, 1998; Marchi et al., 2005; Florian et al., 2007; Iftekhar et al., 2011). In these studies, AlO_4 was always found to be the most abundant Al species by far, although noticeable amounts of 5- and 6-fold coordination were detected. This raises the question if the simulation results are inaccurate or if the discrepancies reflect real structural differences between melts at 3000 K and glasses at room temperature.

The effect of temperature on structure has been investigated experimentally: Florian et al. (2007) performed in-situ ^{27}Al NMR measurements on melt samples with compositions very similar to ours and found that fivefold coordinated Al is favored at high temperatures, without quantifying the extent to which this happens. An increase of the Al coordination number with temperature was even observed in nominally fully polymerized glasses, where AlO_4 could theoretically be fully charge-balanced by modifier cations: by extrapolation to high temperatures of NMR data obtained on $CaAl_2Si_2O_8$ glasses, quenched with varying rates and hence representing varying fictive temperatures, Stebbins et al. (2008) predicted that at 2800 K, up to 39% of Al should be fivefold coordinated. In a temperature-dependent NMR study on calcium aluminate liquid, Massiot et al. (1995) observed an increase of the average Al coordination number above the glass transition temperature by 0.2 per 1000 K. In a neutron diffraction study also on calcium aluminate, (Drewitt et al., 2012) report a significant decrease of Al coordination and other structural rearrangements upon vitrification. These experimental findings lead us to the conclusion that the large Al coordination numbers found in our ab-initio simulations of melts do not indicate a deficiency of the method but are due to the high temperature (3000 K) of the modeled systems. In our classical MD simulations of melts, the even higher Al coordination numbers are explained by the combined effect of high temperatures and the tendency of the interaction potential to over-coordinate Al (see section 2.5.1).

If the large Al coordination numbers in the simulated melts are explained by the high temperature, so why are they still so large in the simulated *glasses* (table 2.5)? The model glasses in this study have been generated by cooling from high-temperature melts (see section 2.3.2), with a quench rate of $5 \cdot 10^{13}$ K/s. This exceeds experimental quench rates, which are typically below 10^5 K/s (see e.g. Stebbins et al. (2008)), by many orders of magnitude. Since the fictive temperature, at which the melt structure is frozen into the glass, increases with increasing quench rate (Mysen and Richet (2005)), the preceding argument for high Al coordination applies as well to rapidly quenched glasses. To assess the influence of the quench rate, we also generated a glass structure of composition $YAl_{11}Si_{19}O_{56}$ with a four times slower simulated quench. No significant changes in the structural parameters were observed with respect to the quickly cooled glass. However, this slower quench is still much faster than in experiments, and we

suppose that lower rates are required to produce structural changes in the resulting glass.

Differences between modeled and measured glass structures do not disprove the simulation results, since the two approaches actually probe different states of the glass resulting from different thermal histories. In the following discussion, we focus on structural *changes* as a function of composition rather than on absolute values of coordination numbers, in order to circumvent this ambiguity.

2.5.3 Relation between cation coordination and field strength

We suggest to rationalize the observed changes in cation coordination for different glass compositions (classical MD simulations) in terms of cation field strength (CFS), which gives a simple measure of a cation's ability to force the surrounding oxygen anions into an energetically favorable configuration. It is defined as CFS = q/r^2, with nominal ionic charge q and ionic radius r. The ionic radii were taken from Shannon (1976), assuming 4-fold coordinated Si, 5-fold coordinated Al and 7- or 8-fold coordinated Y and La, depending on composition (see table 2.5). The resulting CFS are, in descending order, 59 eÅ^{-2} for Si^{4+} (with elementary charge e), 13 eÅ^{-2} for Al^{3+}, 3.3 eÅ^{-2} and 2.9 eÅ^{-2} for Y^{3+} in 7-fold and 8-fold coordination, respectively, and 2.5 eÅ^{-2} and 2.2 eÅ^{-2} for La^{3+} in 7-fold and 8-fold coordination, respectively.

The increasing variability of cation coordination as a function of glass composition, in the order Si, Al, Y, La, reflects their decreasing CFS. The fact that the Si coordination is virtually independent of composition can be explained by its large CFS: in the competition for oxygen bonding among the cations, the Si ions' preference for tetrahedral coordination is satisfied foremost, be it at the expense of more unfavorable coordination environments of the the other cations. The distribution of oxygen between the coordination shells around Al and RE cations is determined by the "reaction"

$$\mathrm{AlO}_n + \mathrm{REO}_m \rightleftharpoons \mathrm{AlO}_{n+1} + \mathrm{REO}_{m-1} \tag{2.8}$$

between coordination polyhedra in the glass. Y has a larger field strength than La and therefore requires a more compact coordination shell with less but shorter and stronger bonds to surrounding oxygen atoms. Thus, the equilibrium in Eq. 2.8 is shifted more to the right for the Y-bearing glasses, as compared to the La-bearing compositions, which explains the higher Al coordination numbers in the former. This trend in Al coordination number has also been observed in a number of experimental studies (Schaller and Stebbins, 1998; Marchi et al., 2005; Florian et al., 2007; Iftekhar et al., 2011).

Also the changes in Al coordination as a function of RE content (for a given REE) can be rationalized in terms of field strength effects: in the RE-rich compositions, the environment of Al is richer in lower-field-strength Y or La and contains less higher-field-strength Si and Al than in the RE-poor glasses, so that Al readily forms a tighter coordination shell in the RE-rich glasses. Furthermore, the low-RE glasses are peraluminous, $[Al_2O_3]/[RE_2O_3] > 3$, and full charge compensation for fourfold coordinated Al is not possible. This also forces Al into higher coordination in these glasses. The same dependence of Al coordination numbers on RE content is also confirmed experimentally by Schaller and Stebbins (1998) and Florian et al. (2007). The latter investigated glass compositions very similar to ours, and they found that the average Al coordination number drops from 4.3 in the Y-poor to 4.1 in the Y-rich glass, which is the same change by 0.2 as found with classical MD simulations. The decreasing RE coordination with increasing RE content can be explained in the same way. It is consistent with the findings in Haigis et al. (2012b), where the Y coordination number in Ca-bearing aluminosilicate melts was shown to decrease with increasing Ca content, since Ca is a weaker competitor for oxygen bonding than Si and Al.

Not only the coordination numbers of cations can be linked to the field strength, but also the width of the coordination shell formed by oxygen around the cations. Whereas high field strength cations are expected to form a tight coordination shell with well defined bond lengths, less powerful cations are anticipated to be forced into more disordered environments with a wider range of nearest-neighbor

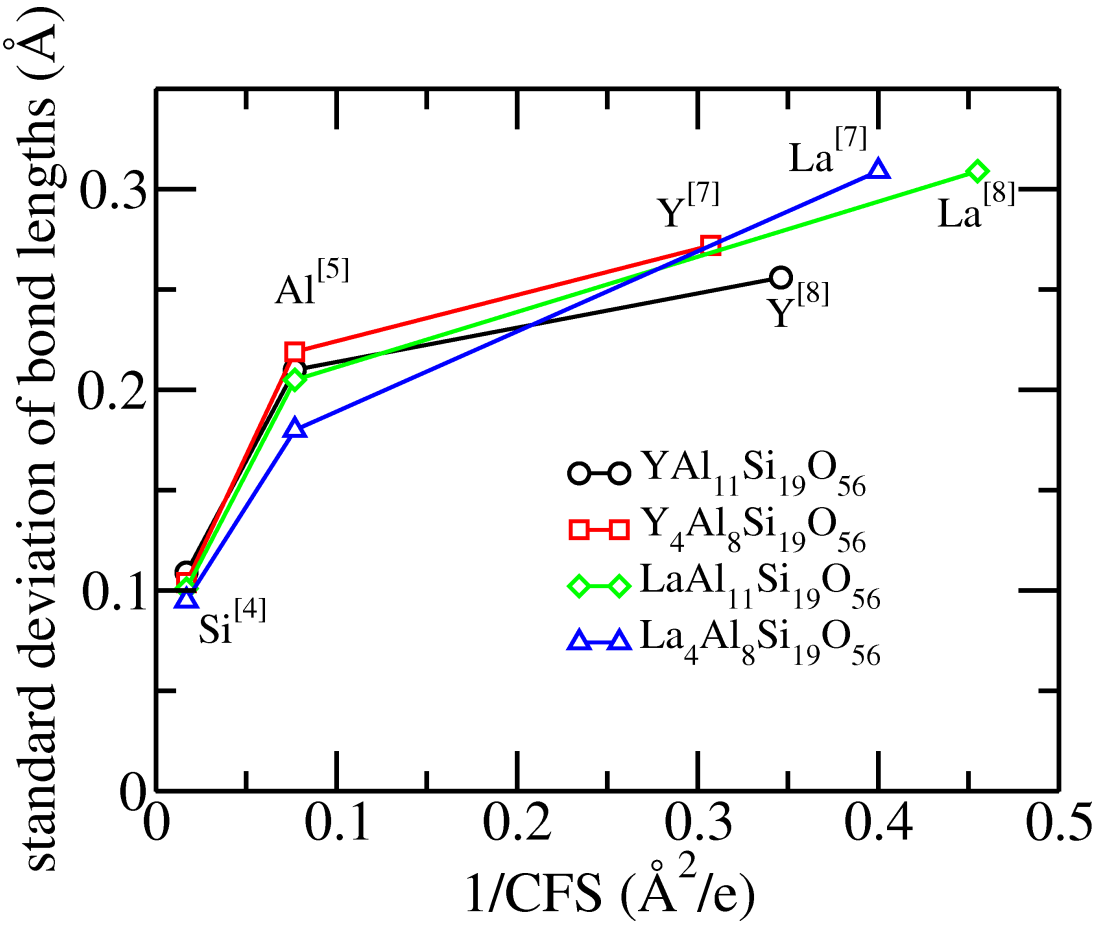

Figure 2.9: Classical MD on glasses: width of the oxygen coordination shell around cations, given as the standard deviation of the distribution of cation-oxygen bond lengths, as a function of inverse cation field strength. The coordination numbers used for the calculation of the field strength are indicated as superscripts. Lines are a guide to the eye.

distances. This behavior is confirmed by the simulation results shown in Fig. 2.9, where the standard deviation of cation-oxygen bond lengths (a measure for the width of the coordination shell) is plotted against the inverse cation field strength. For all four compositions, a (non-linear) correlation is clearly visible. Moreover, the oxygen shell around Si and Al in the La-bearing glasses is found to be narrower, i.e. less perturbed, than in the Y-based compositions. This further corroborates the interpretation of coordination environments in terms of a competition for oxygen bonding between cations of different field strengths.

Coordination shells of cations and their evolution upon compositional changes have been discussed here in terms of the glass structures obtained from classical MD simulations, but the same trends are also observed in the ab-initio MD simulations of melts (Table 2.2). Therefore, the results appear to be robust with respect to the simulation method and seem to hold for both melts and glasses.

2.5.4 Medium-range order: Al/Si ordering

To conclude this section, the distribution of bridging oxygen among the various pairs of tetrahedral species is discussed. Iftekhar et al. (2009) investigated this distribution by means of ^{29}Si NMR experiments on La-bearing aluminosilicate glasses, which were, however, considerably richer in La than our compositions. Their results are based on fitting several distribution models to the data and suggest a nearly random distribution of BO between tetrahedrally coordinated Si and Al. But given the uncertainty of their assumptions and structural models, they caution against over-interpreting this conclusion. Our ab-initio MD simulations of aluminosilicate melts containing Y and La are a unique opportunity to complement the experimental data and to address this question quantitatively and without further assumptions.

In all four compositions studied here, the molar ratio [Al]/[Si] is considerably less than 1, so that strict avoidance of Al-centered tetrahedra linked by BO could formally be achieved (Loewenstein, 1954). However, the results presented in table 2.3 indicate that in all compositions except for the La-rich melt, the BO partitioning between Si and Al is close to random. Only in $La_4Al_8Si_{19}O_{56}$, the $Al^{[4]}$-BO-$Al^{[4]}$ motif is less frequent than expected for a random distribution, in favor of an elevated amount of $Si^{[4]}$-BO-$Al^{[4]}$, but still a significant degree of randomness is observed. A priori, this structural disorder in simulated RE-bearing aluminosilicates may be an effect of the high temperature, which favors configurations of higher entropy. Recently, Jaworski et al. (2012) reported an essentially random Al/Si distribution in La-bearing aluminosilicate glasses, which were, however, considerably richer in La than the compositions studied here. They performed classical MD simulations with a simple pair potential. From our ab-initio simulations in conjunction with the experimental data of Iftekhar et al. (2009) and the results of Jaworski et al. (2012), we conclude that the Al avoidance rule is not obeyed in the melts studied here and that it probably does not (or at least not strictly) apply to the glasses either.

This may be attributed to the greater structural flexibility of amorphous structures as compared to crystalline phases, which allows excess charges on BO between Al-centered tetrahedra to be compensated more easily. On the other hand, in aluminosilicate glasses containing mono- and divalent network modifiers, Al avoidance was found to be realized to a large extent, although not strictly (Lee and Stebbins, 2006). This indicates that also the higher charge and field strength of trivalent Y and La have a share in the Al/Si disorder found in our study, by facilitating charge compensation of otherwise unfavorable structural motifs. This suggests that the traditional picture of glasses, derived from alkali- and alkaline earth-bearing aluminosilicates, should be used carefully when applied to REE-bearing glasses, since trivalent elements may behave differently in terms of network modification and charge balancing.

2.6 Conclusions

The atomic-scale structure of four Y- and La-bearing aluminosilicate glasses and melts with high SiO_2 content (76 mol%) was investigated by ab-initio and classical MD simulations as well as neutron and x-ray diffraction experiments. By combining information from all four approaches, we described the coordination environments of the cations and found robust evidence for structural trends as a function of composition: coordination numbers of RE cations decrease with increasing RE content, and so do Al coordination numbers. Moreover, Al was found to be in a higher coordination state in Y-rich than in La-rich composition. These trends can consistently be explained by the various cation field strengths: they impose a hierarchy on the melts and glasses as to which cation's coordination requirements are satisfied preferentially, at the expense of the others' bonding requirements. Furthermore, the Al avoidance rule, obeyed by aluminosilicate minerals and approximately by glasses with mono- and divalent network modifiers, was found to be almost completely invalidated in RE-bearing aluminosilicate melts.

Ab-initio and classical MD simulations consistently yield a coordination number of Y in RE-bearing aluminosilicate melts and rapidly quenched glasses between 7 and 8, depending on composition. This is larger than the values found in other classical MD studies on glasses, which lie below 7 (Du, 2009) or even below 6 (Iftekhar et al., 2012). It is not clear if the discrepancies are due to the different compositions or to the simple (non-polarizable) interaction potentials used in these studies, or to a combination of both. Similarly, the La coordination numbers found in our ab-initio simulations give values close to 8, considerably larger than the ones obtained for systems richer in La by means of a non-polarizable pair potential (6.0 to 6.6, Jaworski et al. (2012)). The new classical interaction potential for La was shown to produce reasonable melt and glass structures but to form a slightly too tight coordination shell around La, especially in La-rich compositions, which leads to underestimated coordination numbers.

For future classical MD studies, an improved description of La might be achieved by parameterizing a more flexible form of the interaction potential (Jahn and Madden, 2007), which allows for shape deformations of the rather large La^{3+}. Furthermore, it would be desirable to test if increasingly lower quench rates than the one used in this study lead to glass structures with lower Al coordination, closer to those observed in the diffraction experiments.

Chapter 3

Molecular dynamics simulations of Y in silicate melts and implications for trace element partitioning

3.1 Abstract

Element partitioning depends strongly on composition and structure of the involved phases. In this study, we use molecular dynamics simulations to investigate the local environment of Y as an exemplary trace element in four silicate melts with different compositions and thus varying degrees of polymerization. Based on these structural results, we propose a mechanism which explains the observed partitioning trends of Y and other rare-earth elements between crystals and melts or between two melts. With our computational approach, we found a systematic correlation between melt composition and Y coordination as well as Y-O bond lengths, a result which was corroborated by EXAFS spectroscopy on glasses with the same compositions as the simulated melts. Our simulations revealed, moreover, the affinity of Y for network modifiers as second-nearest neighbors (Ca in this study) and the tendency to avoid network formers (Si and Al). This is consistent with the observation that Y (and other rare-earth elements) in general prefer depolymerized to polymerized melts in partitioning experiments (see, e.g., Schmidt et al. (2006)). Furthermore, we used the method of thermodynamic integration to calculate the Gibbs free energy which governs Y partitioning between two exemplary melts. These more quantitative results, too, are in line with the observed partitioning trends.

3.2 Introduction

In the presence of two or more coexisting phases in thermodynamic equilibrium, a minor or trace element will, in general, not be distributed equally among these phases, but will be incorporated preferentially into some chemical environments at the expense of others. The resulting distribution of an element i between two phases α and β is quantified by the Nernst partition coefficient $D_i^{\alpha/\beta} = c_i^\alpha / c_i^\beta$, with c_i^α denoting the concentration (mass fraction) of element i in phase α. The molar partition coefficient $D_{i*}^{\alpha/\beta} = x_i^\alpha / x_i^\beta$ is defined in terms of mole fractions x instead of concentrations and can easily be converted to $D_i^{\alpha/\beta}$ (see Beattie et al. (1993), for terminology). The partition coefficient of element i depends, in general, on temperature, pressure, chemical composition and structure of the involved phases. Conversely, if this dependence is known, either from a compilation of experimental data or from a suitable theory, then the distribution of trace elements in, e.g., rock samples can provide information about the petrogenetic history, and hence constitute a valuable tool for petrologists and geochemists (e.g. Shaw (2006)).

Trace element partitioning between coexisting crystal and melt phases can be understood, at least partially, in terms of the local environment of the incorporated cation in the crystal: if the trace element fits available crystal sites well by size and charge, then it is enriched in the crystal, otherwise it partitions into the melt. It has long been known that crystal-melt partition coefficients of a series of isovalent cations, plotted logarithmically as a function of ionic radius, form near-parabolic patterns which peak at an ideal radius (Onuma et al. (1968)). These patterns have been described quantitatively by Blundy and Wood (1994) by means of the lattice strain model, based on work by Brice (1975). It translates the strain in the crystal lattice, induced by the mismatch of the incorporated cation, to a free energy penalty for cation incorporation, which in turn governs the partitioning.

The lattice strain model, when suitably parameterized, successfully describes observed crystal-melt partitioning behavior in terms of crystal chemistry alone, without explicitly taking into account melt properties. If the latter are important, their influence on partitioning is hidden in the adjustable model parameters and cannot be predicted nor explained by the original model (although Wood and Blundy (1997) extended the model by taking into account the Mg/(Mg+Fe) ratio in the melt). However, there is broad evidence that melt composition can indeed have a strong effect on trace element partitioning. Prowatke and Klemme (2005), in a series of experiments, measured partition coefficients of several trace elements between titanite ($CaTiSiO_5$) and a range of coexisting silicate melts of different compositions. Although the crystal chemistry was virtually constant in all experiments, partition coefficients varied by two orders of magnitude for several rare-earth elements (REE) and Th. Moreover, the partition coefficients were found to depend systematically on melt polymerization, quantified by the molar ratio of $Al_2O_3/(Na_2O + K_2O + CaO)$. In particular, all the REE probed in the study showed an increasing tendency to partition into the melt the more the melt was depolymerized.

More evidence for the influence of melt composition (and thus melt structure) on element partitioning comes from experiments with immiscible silicate melts (Watson (1976); Ryerson and Hess (1978); Schmidt et al. (2006)). In the latter study, partition coefficients between coexisting gabbroic (highly depolymerized) and granitic (highly polymerized) melts were determined for a large set of elements. A strong preference of the REE for the depolymerized melt was found, with $D_{\mathrm{REE}}^{\mathrm{gabbro/granite}} \simeq 10$. According to the authors' interpretation, the abundance of non-bridging oxygen in the depolymerized melt facilitates the formation of the preferred (i.e. energetically favorable) coordination polyhedra of REE and thus favors the observed distribution. In a similar study, Veksler et al. (2006) found the same partitioning trend between immiscible pairs of Fe-rich and Si-rich melt. Mysen (2004) suggested to understand the influence of melt composition on element partitioning in terms of Q^n ($0 \leq n \leq 4$) species whose abundance and proportions vary with bulk composition, thus offering varying amounts of energetically favorable "sites" for trace element incorporation.

It is the aim of this computational study to elucidate the mechanisms by which melt composition influences the distribution of trace elements between crystal and melt or between two melts. We chose Y as an exemplary REE whose partition behavior was shown to depend strongly on melt properties (Prowatke and Klemme (2005); Schmidt et al. (2006)). From a computational point of view, Y is a more convenient element than the (chemically similar) lanthanides whose strongly correlated $4f$ electrons pose notorious problems for theoretical descriptions. Our approach is based on molecular dynamics, a method which provides simultaneous access to the atomic structure and dynamics and to the thermodynamic variables of a system. Taking four different model silicate melts, we first investigated how melt composition influences the local coordination environment of Y ions in the melt. We then translated these structural changes to differences in free energy, which in turn determine the partitioning behavior of Y.

3.3 Methods

3.3.1 Interaction potential

We performed molecular dynamics (MD) simulations to investigate structural and thermodynamic properties of silicate melts. Given the considerable system sizes and simulation times required for our study, we did not perform first-principles MD but used a polarizable ionic interaction potential (see Wilson and Madden (1993) for a general discussion) which has been parameterized from first principles (i.e. from fundamental laws of nature, without reference to experimental data), taking density functional theory (DFT, Hohenberg and Kohn (1964); Kohn and Sham (1965)) as a reference. The polarizable ion model is of the form

$$V(\{\mathbf{r}\}) = V^{qq} + V^{\mathrm{rep}} + V^{\mathrm{disp}} + V^{\mathrm{pol}} \tag{3.1}$$

where $\{\mathbf{r}\}$ represents the set of ionic positions. The first term on the right side describes charge-charge interactions between pairs of ions at $\mathbf{r}_i$ and $\mathbf{r}_j$, with distance $r_{ij} = |\mathbf{r}_i - \mathbf{r}_j|$ and nominal charges q_i and q_j ($q_{\mathrm{O}} = -2$, $q_{\mathrm{Si}} = 4$, $q_{\mathrm{Ca}} = 2$, $q_{\mathrm{Al}} = q_{\mathrm{Y}} = 3$):

$$V^{qq} = \sum_{i<j} \frac{q_i q_j}{r_{ij}} \tag{3.2}$$

The second term represents the repulsion between two ions due to the overlap of electron densities at short distances:

$$V^{\mathrm{rep}} = \sum_{i<j} A_{ij} \exp(-a_{ij} r_{ij}) \tag{3.3}$$

The A_{ij} and a_{ij} are adjustable model parameters. With the third term, we model dispersion interactions:

$$V^{\mathrm{disp}} = -\sum_{i<j} f_6^{ij}(r_{ij}) \frac{C_6^{ij}}{r_{ij}^6} \tag{3.4}$$

Here, the C_6^{ij} are calculated from condensed-phase ionic polarizabilities (see below) and the f_6^{ij} represent Tang-Toennies dispersion damping functions which describe deviations from the asymptotic C_6^{ij}/r_{ij}^6 behavior at short distances (Tang and Toennies (1984)) and are defined as

$$f_6^{ij}(r_{ij}) = 1 - \exp(-b_6^{ij} r_{ij}) \sum_{k=0}^{4} \frac{(b_6^{ij} r_{ij})^k}{k!} \tag{3.5}$$

with adjustable parameters b_6^{ij}. The last term in Eq. 3.1 takes into account the polarizability α of the ions and comprises Coulombic charge-dipole and dipole-dipole interactions as well as a self-energy term which describes the energy cost to polarize an ion:

$$\begin{aligned} V^{\mathrm{pol}} = & \sum_{i<j,\alpha} \left[q_i \mu_j^\alpha f_D^{ij}(r_{ij}) - q_j \mu_i^\alpha f_D^{ji}(r_{ji}) \right] T_\alpha^{(1)} \\ & - \sum_{i<j,\alpha,\beta} \mu_i^\alpha \mu_j^\beta T_{\alpha\beta}^{(2)} + \sum_i \frac{|\mu_i|^2}{2\alpha_i} \end{aligned} \tag{3.6}$$

By μ_i^α, we denote the Cartesian components of ionic dipole moments, and their interaction with ionic charges q_i is damped at short distances by means of Tang-Toennies dipole damping functions $f_D^{ij}(r_{ij})$. These have the same form as in Eq. 3.5, but now contain the adjustable parameters b_D^{ij} instead of b_6^{ij}. Finally, we write $T_{\alpha\beta\ldots}^{(n)} = \nabla_\alpha \nabla_\beta \cdots 1/r_{ij}$ for the multipole interaction tensors, with the superscript denoting the order of the derivative (Stone (1996)).

We emphasize that the polarization term V^{pol} goes beyond a simple pairwise interaction and introduces real many-body effects. This is because at each MD step, i.e. for given ionic positions $\{\mathbf{r}\}$, all ionic dipole moments are determined self-consistently by minimizing V^{pol} as a function of the dipole moments (Wilson and Madden (1993)), using a conjugate-gradient algorithm. The polarization term turned out to be crucial for a transferable interaction potential for oxides (Rowley et al. (1998)). In fact, polarizability mimics a deformable electron density, which is an indispensable ingredient of formally ionic models if they are to describe oxides (or silicates) correctly.

The interaction potential, Eqs. 3.1 to 3.6, was parameterized by matching dipoles, forces, and stresses derived from the potential to dipoles, forces, and stresses obtained from DFT, following the procedure presented in Aguado et al. (2003) and Jahn and Madden (2007). As reference configurations, we chose four melt configurations with compositions SiO_2, Al_2O_3, CaO, and Y_2O_3, generated by Born-Oppenheimer MD with at least 80 atoms in the simulation cell. The equilibration runs and the static DFT calculations on the four reference configurations were carried out with the CPMD code (Car and Parrinello (1985); Marx and Hutter (2000)) within the local density approximation, using Troullier-Martins pseudopotentials (Troullier and Martins (1991)). We found that a plane-wave cutoff of at least 180 Ry (240 Ry for CaO) and a Brillouin zone sampling restricted to Γ produced converged forces, dipoles and stress tensors. The ionic dipoles were calculated from the configuration of maximally localized Wannier functions (Marzari and Vanderbilt (1997)) around ion cores. The model parameters were determined by a least-square fit in a two-step procedure. First, the condensed-phase ionic polarizabilities α_i and all the dipole damping parameters b_D^{ij} were optimized. We treated only O^{2-}, Ca^{2+}, and Y^{3+} as polarizable, and neglected the polarizability of the small cations Si^{4+} and Al^{3+}. Second, keeping these values fixed, the remaining parameters were fitted to DFT forces and stresses. The values of all model parameters are listed in table 3.1.

i–j	O–O	Si–O	Al–O	Ca–O	Y–O	Ca–Ca	Y–Y	Ca–Y
q_i	-2	+4	+3	+2	+3			
A_{ij}	5328.3	44.624	39.404	76.811	95.048			
a_{ij}	3.1526	1.6513	1.6413	1.7038	1.6813			
C_6^{ij}	52.461			16.716	23.763	6.4724	12.504	8.9817
b_6^{ij}	2.7370			1.7543	1.4995	2.8594	0.67066	1.0865
α_i	10.754			2.4116	3.5475			
b_D^{ij}	0.0	1.6489	1.5573	1.4304 (Ca-O)/ 3.4741 (O-Ca)	1.5056 (Y-O)/ 3.3585 (O-Y)			

Table 3.1: Interaction parameters, see Eqs. 3.1 to 3.6, in atomic units. Interactions not listed or left blank here, e.g., short-range repulsion for Si–Si, are taken to be absent in the model. Since $b_D^{ij} \neq b_D^{ji}$ in general, both parameters are listed.

To test the accuracy of the new interaction potential, we applied it to $Ca_3(Al,Y)_2(SiO_4)_3$ melt, with one Y atom in the simulation cell, and compared the results to the outcome of a DFT MD run for this system. Since this melt was not among the reference systems used for the fit, we hereby also checked whether the potential is transferable to different chemical compositions. The radial distribution functions for all the cation-oxygen pairs, plotted in Fig. 3.1, are in excellent agreement with DFT. Melt density constitutes another test of the interaction potential. In an MD simulation at 3000 K and ambient pressure, the density was found to be 2.62 g/cm^3. Unfortunately, no experimental data are available at these conditions, so we resort to the expression given by Lange and Carmichael (1987) for the density of multicomponent silicate melts, which is based on a large experimental data set. At 3000 K, $Ca_3Al_2(SiO_4)_3$ melt is predicted to have a density of 2.45 g/cm^3, 6% lower than our simulation result. This overestimation of density by our interaction potential can be explained by the fact that it has been

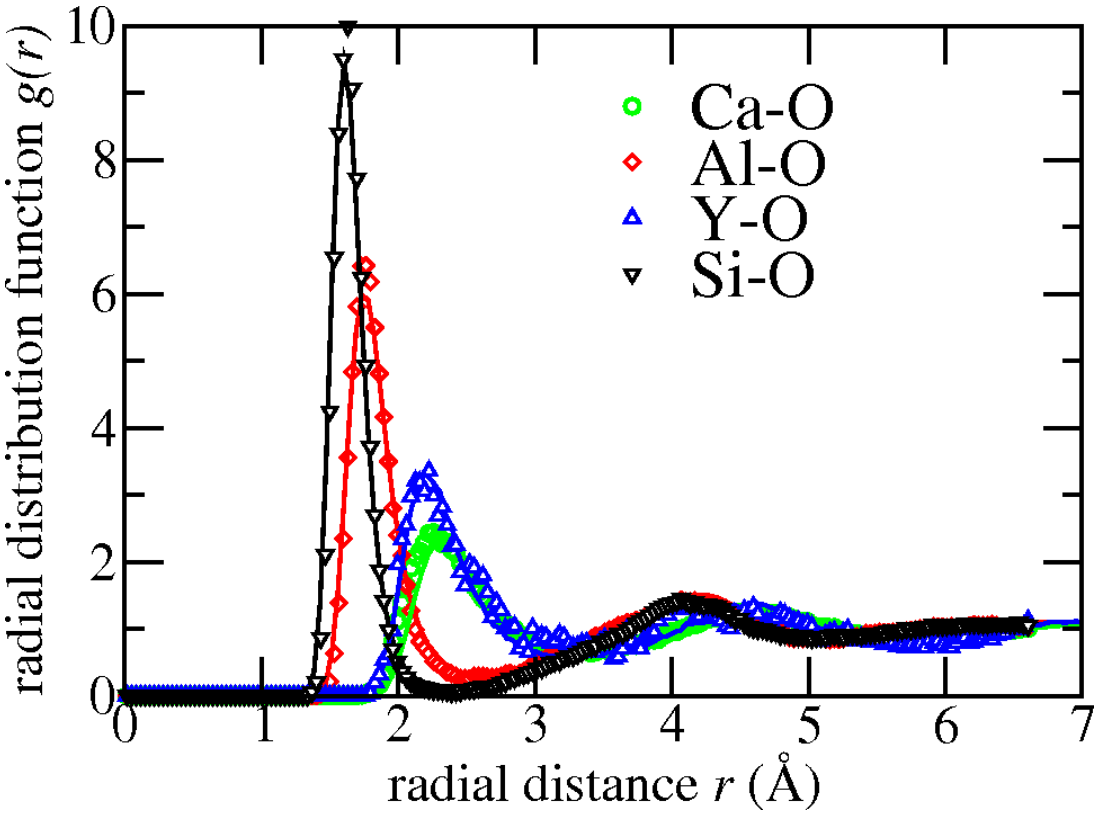

Figure 3.1: Radial distribution functions for cation-oxygen pairs in $Ca_3(Al,Y)_2(SiO_4)_3$ melt (grossular composition), at 3000 K and a density of 2.62 g/cm^3. Full lines represent data obtained with the polarizable ion model and symbols are DFT results. The simulation with the polarizable ion model was done with a simulation cell containing one Y atom and 1280 atoms in total. For the DFT-based MD, the simulation cell contained one Y atom and 160 atoms in total, and Born-Oppenheimer MD was performed in the local density approximation, with a plane-wave cut-off of 80 Rydberg.

parameterised with respect to the local density approximation to DFT, which is known to underestimate lattice constants by about 1%-2%, i.e. to overestimate densities by 3%-6%. On the other hand, Lange and Carmichael (1987) caution against using their density formula at temperatures far above 1873 K and indicate that it might underestimate the density of Al-bearing silicate melts at higher temperatures by several percent, so that the difference to our simulated density would be even smaller. In conclusion, the interaction potential has been shown to reproduce DFT-derived melt structures well and to predict melt densities consistent with extrapolations of experimental data.

We close this part of the paper by commenting on the dispersion interaction, the contribution of which to the total potential energy of our model is small, but not negligible. There is no obvious way of obtaining the coefficients C_6^{ij} from DFT calculations, since dispersion is not well described by the available approximate exchange-correlation functionals. However, the coefficients are related to the polarizabilities via the Casimir-Polder integral (Casimir and Polder (1948)) or, in an approximate way, via the Slater-Kirkwood expression (Slater and Kirkwood (1931))

$$C_6^{ij} = \frac{3}{2} \frac{\alpha_i \alpha_j}{\sqrt{\alpha_i/N_i} + \sqrt{\alpha_j/N_j}} \tag{3.7}$$

where N_i is a parameter which can be calculated from like-ions interactions and eq. 3.7 as

$$N_i = \left[\frac{4}{3} \frac{C_6^{ii}}{\alpha_i^{3/2}} \right]^2 \tag{3.8}$$

if C_6^{ii} and α_i are known. N_i can then be used in the "combination rule" for unlike ions, Eq. 3.7. Unfortunately, we don't know the value of $C_6^{O^{2-}-O^{2-}}$ etc. in condensed phases. However, Koutselos and Mason (1986) found empirically that N is nearly constant for ions of an isoelectronic sequence, i.e. $N_{O^{2-}} \simeq N_{Ne}$ etc. Thus we chose the following procedure to determine the coefficients C_6^{ij}: First we calculated N_{Ne}, N_{Ar}, and N_{Kr} from Eq. 3.8, with gas phase α's and like-ions C_6's obtained from high-level calculations by Chu and Dalgarno (2004). Following Koutselos and Mason (1986), we then assumed $N_{O^{2-}} = N_{Ne}$, $N_{Ca^{2+}} = N_{Ar}$, $N_{Y^{3+}} = N_{Kr}$, and together with the condensed-phase polarizabilities resulting from the dipole-fitting, these yield the required coefficients C_6^{ij}, by Eq. 3.7. These coefficients, like the dipole parameters, are held constant during the subsequent optimization of the remaining model parameters. Although approximate, the procedure is physically justified and produces reasonable dispersion coefficients.

3.3.2 Molecular dynamics

Once the interaction potential was parameterized, we performed MD simulations for four silicate melts, of major-element composition Al_2SiO_5, $CaAl_2Si_2O_8$, $Ca_3Al_2(SiO_4)_3$ and $CaSiO_3$. The cubic simulation cells, repeated periodically in space, contained 1152, 1664, 1280 and 1079 atoms, respectively, with one Al^{3+} replaced by Y^{3+} (three CaO replaced by Y_2O_3 in the case of $CaSiO_3$). The atoms were first placed randomly into the cells, which were then equilibrated for at least 20 ps at 3000 K and ambient pressure. Temperature and pressure were controlled by a Nosé-Hoover thermostat (Nosé (1984); Hoover (1985)) and a barostat (Martyna et al. (1994)), respectively. We then fixed the volume of the simulation cell to the average volume of the last 10 ps and equilibrated the systems during another 10 ps, now at constant volume and temperature $T = 3000$ K (NVT ensemble). Data were acquired during subsequent NVT simulations of 100 ps duration, using a time step of 1 fs for the integration of the Newtonian equations of motion. The structural results obtained from the MD simulations (coordination numbers, bond lengths) are well-converged with respect to the run duration, since virtually the same values result from analysis of the last 50 ps only of each simulation. For the first three compositions, since there was only one Y atom per cell, the interaction with other Y atoms (periodic images in other cells) was very weak, given

a minimum distance of 23.5 Å. For $CaSiO_3$, we checked that the two Y atoms in the simulation cell did not form a complex during the simulation. Hence, we expect Y to behave as a trace element in all simulations.

3.3.3 Thermodynamic integration

Trace element partitioning is ultimately driven by the tendency of any thermodynamic system to minimize its free energy. Whereas the internal energy U of a system is readily obtained from MD simulations, free energies cannot be extracted directly from a single simulation (note that also in experiments, free energies cannot be determined from a single measurement, in contrast to quantities like temperature or pressure). However, the method of thermodynamic integration can be used to derive free energy differences from MD (Frenkel and Smit (2002)). We applied this method to calculate the change in Gibbs free energy associated with an exchange reaction of Y and Al between two silicate melts:

$$\begin{aligned} \mathrm{Y}^{3+} \text{ in melt 1} + \mathrm{Al}^{3+} \text{ in melt 2} \\ \rightleftharpoons \mathrm{Al}^{3+} \text{ in melt 1} + \mathrm{Y}^{3+} \text{ in melt 2} \end{aligned} \tag{3.9}$$

The equilibrium constant K of this reaction is related to the molar exchange coefficient $K_{D,\mathrm{Y/Al}}^{\mathrm{m2/m1}}$ (see Beattie et al. (1993) for terminology):

$$K = \frac{a_{\mathrm{Al}}^{\mathrm{m1}} a_{\mathrm{Y}}^{\mathrm{m2}}}{a_{\mathrm{Y}}^{\mathrm{m1}} a_{\mathrm{Al}}^{\mathrm{m2}}} \simeq \frac{x_{\mathrm{Al}}^{\mathrm{m1}} x_{\mathrm{Y}}^{\mathrm{m2}}}{x_{\mathrm{Y}}^{\mathrm{m1}} x_{\mathrm{Al}}^{\mathrm{m2}}} = \frac{D_{\mathrm{Y}*}^{\mathrm{m2/m1}}}{D_{\mathrm{Al}*}^{\mathrm{m2/m1}}} = K_{D,\mathrm{Y/Al}}^{\mathrm{m2/m1}} \tag{3.10}$$

Here, m1 and m2 stand for the two melts, of different composition. The exchange coefficient is just the partition coefficient of Y, normalized by the one of Al, and thus quantifies the fractionation of Y and Al between the melts. We assumed that activities a can be replaced by mole fractions x in Eq. 3.10.

For computational purposes, we split the exchange reaction (3.9) into two partial reactions, or "transmutations",

$$\begin{aligned} \mathrm{Y}^{3+} \text{ in melt 1} &\rightleftharpoons \mathrm{Al}^{3+} \text{ in melt 1} \\ \mathrm{Al}^{3+} \text{ in melt 2} &\rightleftharpoons \mathrm{Y}^{3+} \text{ in melt 2} \end{aligned} \tag{3.11}$$

The reason for this splitting is that we can compute the change in Gibbs free energy for each of the two partial reactions by means of thermodynamic integration, following the procedure described by Salanne et al. (2008) and outlined in the next paragraph. With this method, the interaction parameters of Y are gradually transformed into those of Al (or vice versa). Although the two reactions in Eq. 3.11 do not correspond to real physical processes, the associated free energy differences are well defined, and taken together, they give the complete (physical) exchange reaction (3.9). The total change in Gibbs free energy, ΔG, for the reaction (3.9) determines the equilibrium constant $K = \exp(-\Delta G/(RT))$ and thus the exchange coefficient through eq. 3.10.

In more technical terms, in order to describe the transmutations, we introduce a hybrid potential energy function, characterizing a system in which one Y atom is partially transmuted into Al. It is defined as a linear mixture of two potential energy functions of the same form as in Eq. 3.1:

$$V_\lambda(\{\mathbf{r}\}) = (1-\lambda) V_{\mathrm{Y}}(\{\mathbf{r}\}) + \lambda V_{\mathrm{Al}}(\{\mathbf{r}\}) \tag{3.12}$$

Here, V_{Y} is the potential energy of the system (melt) containing one Y^{3+}, and V_{Al} is the potential energy of a system where Y^{3+} is replaced by Al^{3+}. The parameter λ takes on values between 0 (the atom in question is pure Y) and 1 (the atom is fully transmuted into Al). Now, following an idea of Kirkwood (1935), we express the free energy change for the "reaction" $\mathrm{Y}^{3+} \longrightarrow \mathrm{Al}^{3+}$ in a given melt (one of the transmutations in Eq. 3.11) as

$$\Delta G = \int_0^1 \left\langle \frac{\partial V_\lambda}{\partial \lambda} \right\rangle_\lambda \mathrm{d}\lambda = \int_0^1 \langle V_{\mathrm{Al}} - V_{\mathrm{Y}} \rangle_\lambda \, \mathrm{d}\lambda \tag{3.13}$$

where $\langle \ldots \rangle_\lambda$ denotes the average in a system governed by the hybrid potential energy function V_λ. The crucial point of the method is that the difference $V_{\mathrm{Al}}(\{\mathbf{r}\}) - V_{\mathrm{Y}}(\{\mathbf{r}\})$ is a known function of the atomic coordinates, and hence its average can be computed directly from an MD trajectory, unlike ΔG itself. If $\langle V_{\mathrm{Al}} - V_{\mathrm{Y}} \rangle_\lambda$ is evaluated by means of several MD simulations for a set of λ values, the free energy of reaction (transmutation) can be obtained by numerical integration according to Eq. 3.13.

The simulations were carried out by means of the CP2K code (http://cp2k.berlios.de/). As melt compositions m1 and m2, we chose Al_2SiO_5 and $CaAl_2Si_2O_8$, with supercells containing 22 formula units in the case of Al_2SiO_5 and 16 formula units in the case of $CaAl_2Si_2O_8$. Both systems were equilibrated at 2500 K and ambient pressure, and data were acquired at constant volume (corresponding to ambient pressure) and with a Nosé-Hoover thermostat maintaining the temperature at 2500 K. In each system, Al was gradually transformed into Y in five steps, and at each intermediate step, we performed a full MD of 12 ps duration, starting from the final configuration of the previous run. Of these 12 ps, the first 2 ps served for equilibration after slightly changing the interaction potential V_λ, and the remaining 10 ps were used for analysis. After a full transmutation from Al to Y, we also simulated the reverse transmutation from Y to Al. The sum of free energy changes, $\Delta G_{\mathrm{forward}} + \Delta G_{\mathrm{backward}}$, of the forward and the backward transmutation (which should ideally be zero since it represents a null reaction) was used to estimate the error due to incomplete sampling of the phase space.

Since periodic boundary conditions were applied, the question arises how the finite size of the simulation cell influences the calculated free energy differences. We expect that the respective error is below 5%, for the following reason: Ayala and Sprik (2008) carefully studied the finite-size effect on the free energy change associated with a redox reaction of a single metal cation in water, using thermodynamic integration as well. They found that free energies were converged to $< 5\%$ with respect to the limit of very large cells, for cell sizes comparable to ours. Now, in their study, the transmutation involves a change of the cationic charge ($M^{2+} \rightleftharpoons M^{3+}$), whereas in our case, only the short-range interaction and the less significant polarizability and van der Waals parameters are changed ($Y^{3+} \rightleftharpoons Al^{3+}$). Therefore, the effect of limited cell sizes should be even less important here than in the redox case, where changes in strong, long-range Coulomb interactions occur.

3.4 Results and discussion

3.4.1 Atomic environment of Y in silicate melts from MD simulations

The four melt compositions, Al_2SiO_5, $CaAl_2Si_2O_8$, $Ca_3Al_2(SiO_4)_3$ and $CaSiO_3$, were selected in such a way as to span a wide range of melt polymerization. As a simple compositional variable, we chose the ratio of non-bridging oxygens to the total amount of Si and Al, NBO/(Si+Al), which was obtained from the simulations. For the present study, we prefer this terminology to the more standard NBO/T (T = tetrahedrally coordinated network former) because the average coordination of Al was found to be larger than 4, even in nominally fully polymerized melts, and thus Al cannot always be classified as T. We still suggest to view NBO/(Si+Al) as a measure of melt depolymerization, with Ca acting as a network modifier. Non-bridging oxygen is defined here as oxygen which is not exclusively bonded to Si or Al, according to the bonding criterion presented in the following paragraph.

Coordination numbers and average bond lengths were obtained from the simulations in the following way: for a given pair of elements i, j, we calculated the radial pair distribution function $g(r_{ij})$ by organizing the various $i-j$ distances occurring during the simulation into bins and suitably normalizing the resulting distribution (see, e.g., Fig. 3.1). We then fixed the cut-off radius r_{cut} for this element pair at the distance where $g(r_{ij})$ adopts its first minimum, i.e. r_{cut} represents the radial extent of the first coordination shell. The coordination of element i by element j is determined by averaging, over all i-atoms and over the duration of the simulation, the number of j-atoms closer to a given i-atom than r_{cut}. Similarly, the average $i-j$ bond length is obtained as the average distance r_{ij} of atom pairs with a distance less

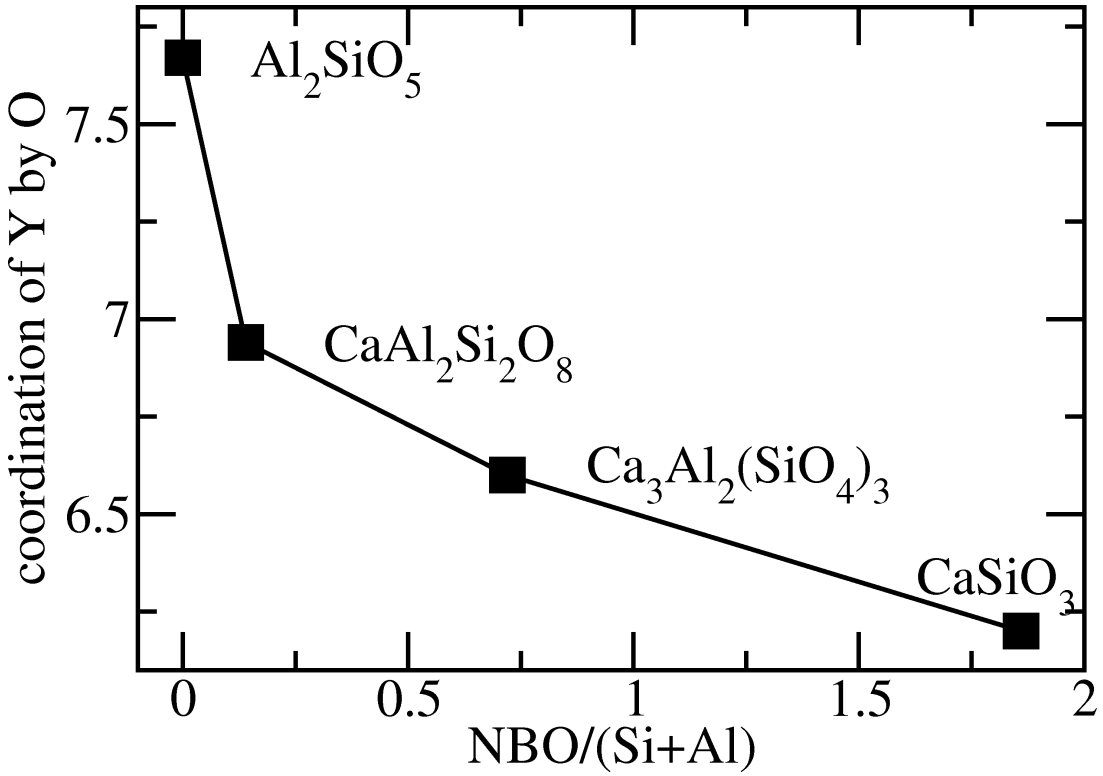

Figure 3.2: Coordination number of Y by O as a function of melt composition, NBO/(Si+Al) from simulation. Lines are a guide to the eye.

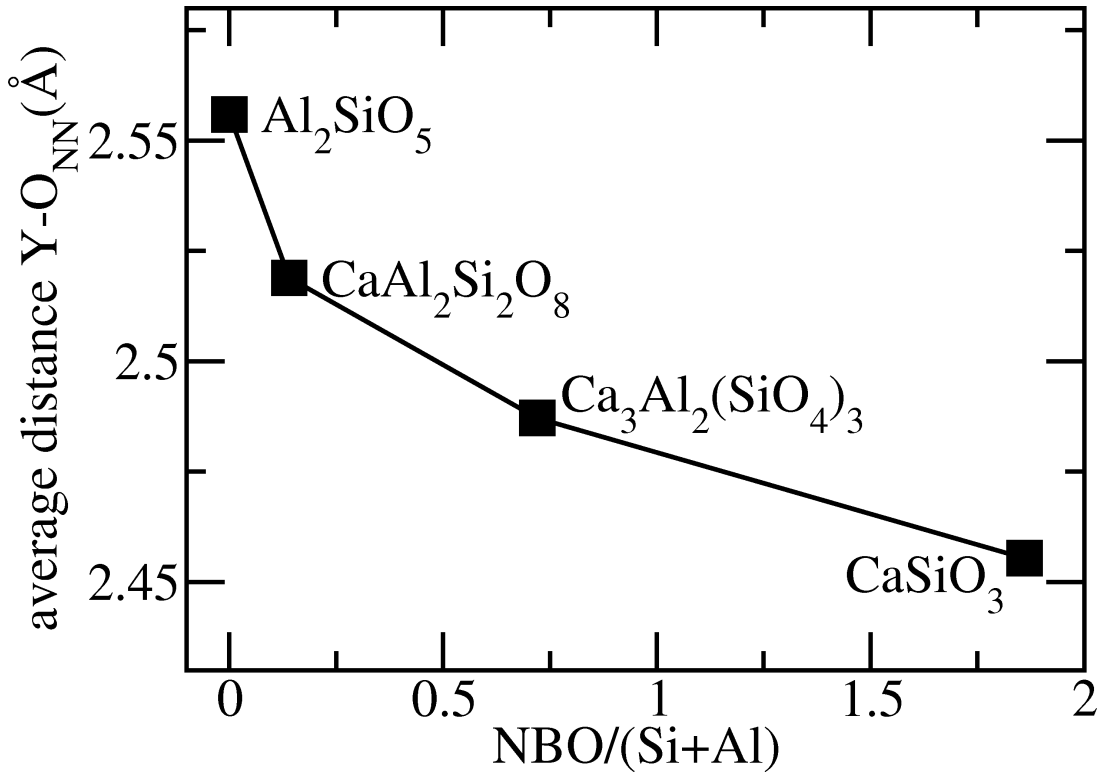

Figure 3.3: Average nearest-neighbor (NN) Y-O bond length as a function of melt composition, NBO/(Si+Al) from simulation. Lines are a guide to the eye.

than r_{cut}. Note that in general, r_{cut} for a given element pair varies with melt composition, which reflects changes in the shape of the first coordination shell.

As a first step towards understanding the atomistic mechanisms leading to trace element partitioning between melts, we investigated how the local environment of Y changes as a function of melt composition. Fig. 3.2 shows that the coordination of Y by O drops from 7.7 in Al_2SiO_5 (which has NBO/(Si+Al) = 0.0) to 6.2 in $CaSiO_3$ (NBO/(Si+Al) = 1.9). Concurrently, the average distance between Y and its nearest-neighbor oxygen decreases from 2.56 Å to 2.46 Å, as can be seen from Fig. 3.3. Coordination numbers and average Y-O distances are also listed in table 3.2. In Fig. 3.4, the radial distribution of oxygen atoms around Y is plotted for the four different melt compositions. We observe that with increasing NBO/(Si+Al), the distribution becomes narrower, or in other words, oxygen disorder around Y decreases. The peak position does not exhibit systematic changes, except for the case of Al_2SiO_5, where it is shifted to larger Y-O distances. For the other three compositions, the height of the peak increases with increasing NBO/(Si+Al). These data imply that the observed decrease of coordination number and Y-O bond length with decreasing polymerization is largely due to the reduction of the tail of the distribution at large Y-O distances.

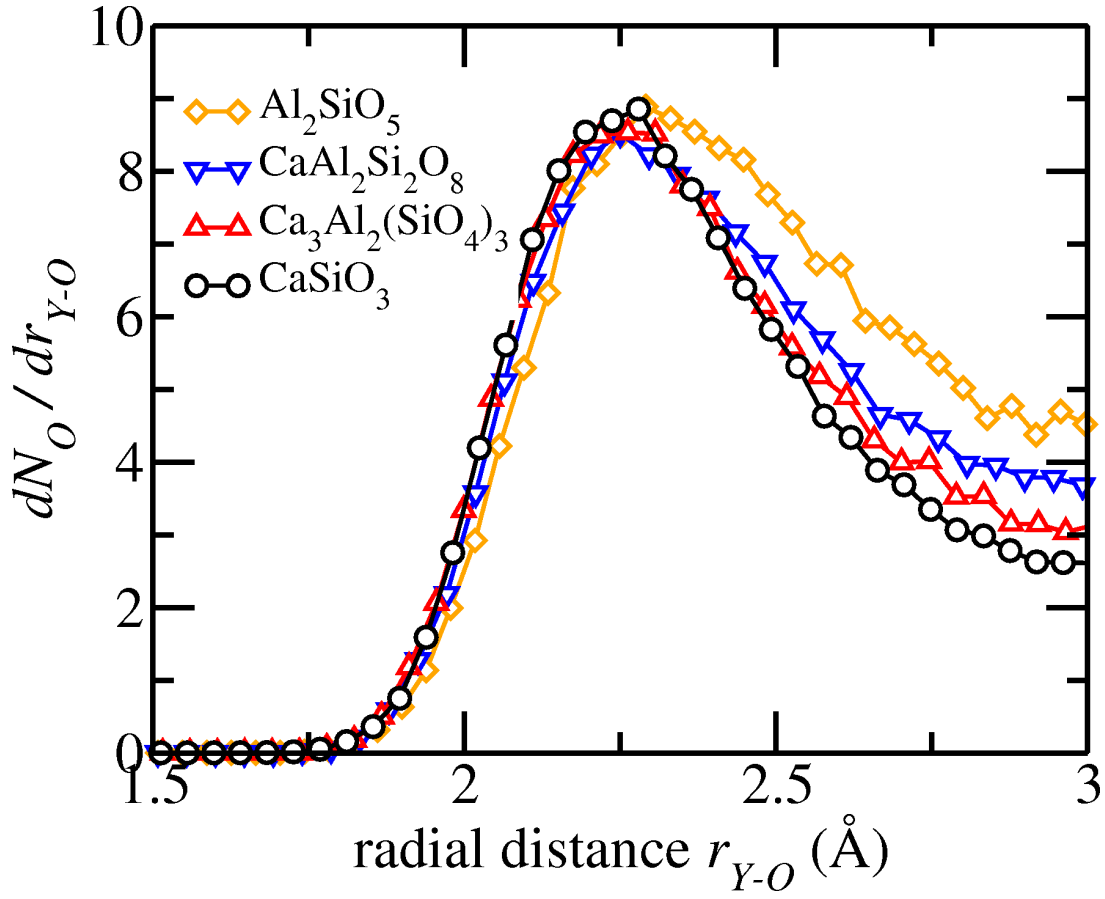

Figure 3.4: Distribution of O around Y in four silicate melts as obtained from MD simulation. The area under a curve up to a certain distance r_{Y-O} gives the number N_O of oxygen atoms within a sphere of radius r_{Y-O} around Y. Lines are a guide to the eye.

In order to gain further insight into structural differences resulting from changes in composition, we also investigated the chemical composition of the second coordination shell around Y. In Fig. 3.5, we plot the average number of cations bonded to one oxygen atom if the latter is itself bonded to Y. Oxygen-cation bonding statistics were again based on cut-off radii obtained from the simulations. As expected from the bulk melt composition, the amount of Ca in the second shell increases at the expense of Si

and Al, when going to the more depolymerized, i.e. more Ca-rich compositions. The essential result, however, is that for all Ca-bearing melts, the ratio Ca/(Si+Al) in the second coordination shell is *larger* than the bulk ratio, i.e. Y tends to be associated with the network modifier Ca rather than with Si or Al.

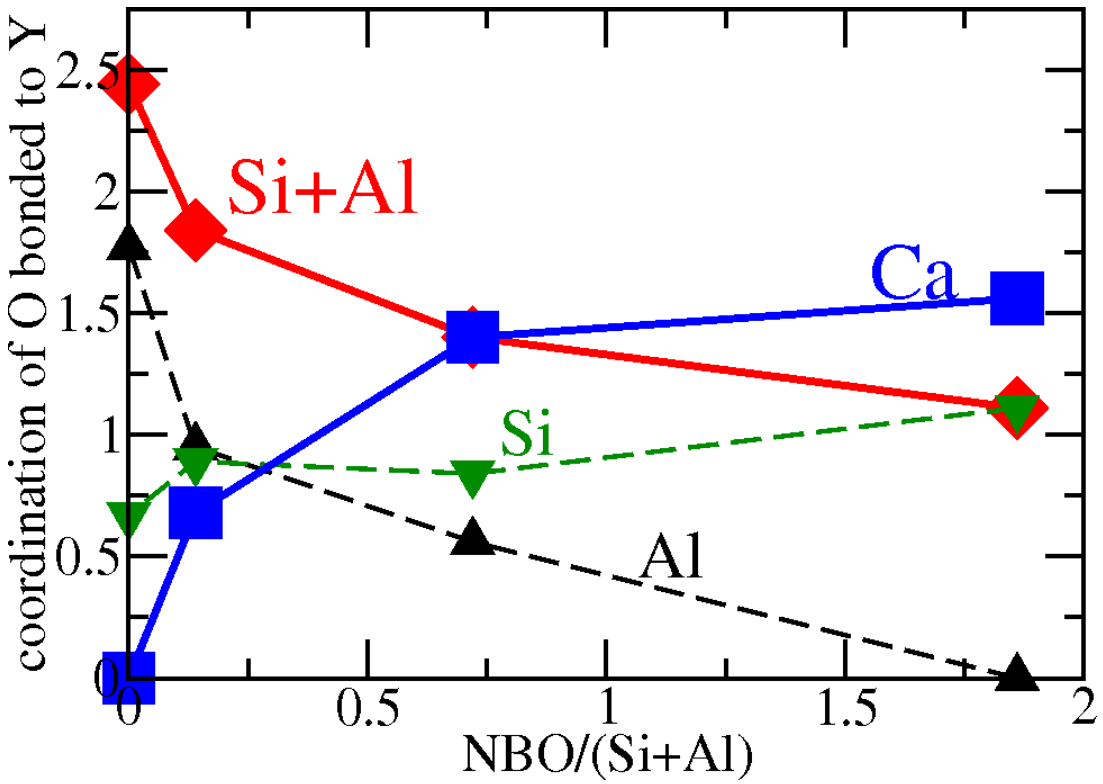

Figure 3.5: Distribution of O around Y in four silicate melts as obtained from MD simulation. The area under a curve up to a certain distance r_{Y-O} gives the number N_O of oxygen atoms within a sphere of radius r_{Y-O} around Y. Lines are a guide to the eye.

In the light of these structural findings, we put forward a qualitative explanation of the observed partitioning of Y in terms of its bonding requirement. Whereas Si and Al form very strong bonds with oxygen, the Ca-O bonds have a looser character, since Ca is less charged and has a greater ionic radius than Si and Al. When trying to satisfy its bonding requirements, Y competes for oxygen bonds with other cations. In a polymerized melt, many strong competitors (Si and Al) are present, and Y has to take what is left, forming many weak (elongated) bonds. On the other hand, in the presence of weak competitors like Ca, Y can shape its bonding environment according to its needs and forms less, but stronger (shorter) bonds. The enhanced ability of Y to shape its environment is reflected by the reduced oxygen disorder around Y, which is indicated by the narrower Y-O distribution shown in Fig. 3.4, as discussed above. This picture explains the trends in coordination number and average Y-O distance seen in the simulations. The fact that Y prefers to be associated with Ca instead of Si and Al in the second coordination shell indicates that it is energetically more favorable for Y to be surrounded by weak competitors. This should lead to the observed partitioning into the more depolymerized melts. In section 3.4.3, we will take a more quantitative approach to the energetics of trace element partitioning.

3.4.2 Comparison to EXAFS experiments

To corroborate our structural findings obtained from MD simulations, we compared them to results from extended x-ray absorption fine structure (EXAFS) spectroscopy at the Y K-edge on four glasses of the same major-element composition as the four simulated silicate melts, doped with 5000 ppm of Y. EXAFS

probes the local environment around a selected element and hence provides information about the first coordination shell of O around Y, in particular about the average Y-O distance. Since the spectra taken on Al_2SiO_5 glass could not be interpreted satisfactorily, this composition was excluded from further analysis. The details of synthesis, sample preparation, data acquisition and analysis are described by Simon et al. (2012).

A difficulty arises from the fact that the experiments were performed on glasses at room temperature whereas the simulations describe melts at 3000 K. Apart from one case (see below), we did not perform extensive simulations of glasses at room temperature (which could be compared directly to the EXAFS data) because MD averages are physically meaningful only to the extent that the simulated system samples all of the energetically relevant phase space. For a single Y atom in glassy silicates, this criterion is not fulfilled at low temperatures and with tractable simulation box sizes and simulation lengths. On the other hand, *in situ* EXAFS measurements on melts are experimentally very challenging (Pauvert et al., 2010). We anticipate that absolute interatomic distances will be larger in the high-temperature melt than in the glass, due to thermal expansion, but expect *changes* between different compositions to be similar for melts and glasses.

	simulation	experiment
Al_2SiO_5		
CN	7.7	–
r_{cut}	3.24	
$\overline{d}$	2.56	–
$CaAl_2Si_2O_8$		
CN	6.9	6.9*
r_{cut}	3.24	
$\overline{d}$	2.52	2.34 (0.01)
$Ca_3Al_2(SiO_4)_3$		
CN	6.6	6.6*
r_{cut}	3.25	
$\overline{d}$	2.49	2.31 (0.01)
$CaSiO_3$		
CN	6.2	6.2*
r_{cut}	3.22	
$\overline{d}$	2.46	2.28 (0.01)

Table 3.2: Structural parameters for Y in silicate melts (glasses): coordination number CN, cut-off radius r_{cut} for CN in Å and average Y-O distance $\overline{d}$ in Å, with standard deviations in parentheses. Simulations performed at 3000 K, EXAFS spectra taken on glasses at 300 K. *CN fixed at simulation values, see text for explanation.

The Y-O distance resulting from the analysis of the EXAFS data are compared to the results from the simulations in table 3.2. For the analysis of the EXAFS data, the coordination of Y was taken to be the one found in the MD simulations (see Simon et al. (2012) in this issue for a discussion). As expected, we find Y-O bonds systematically elongated by about 8% in the high-temperature simulation with respect to the data extracted from EXAFS. But remarkably, the Y-O bond length decreases consistently by 0.06 Å in both simulation and experiment, when going from the more polymerized $CaAl_2Si_2O_8$ to the more depolymerized $CaSiO_3$. For the distribution of O around Y, the experimental data reveal the same trend as the MD simulations: with increasing NBO/(Si+Al), the peak becomes narrower and higher, reflecting increasing oxygen order around Y (Fig. 3.6). As expected, these distributions, measured on glasses, are significantly narrower and more pronounced than the ones obtained from the simulation of high-

temperature melts (Fig. 3.4). Note, however, that they sum up to the same coordination numbers. The agreement in change of Y-O bond length between simulation and experiment as well as the congruent changes in the shape of the distribution suggest that our interaction model for MD correctly captures the link between melt composition and local environment around Y.

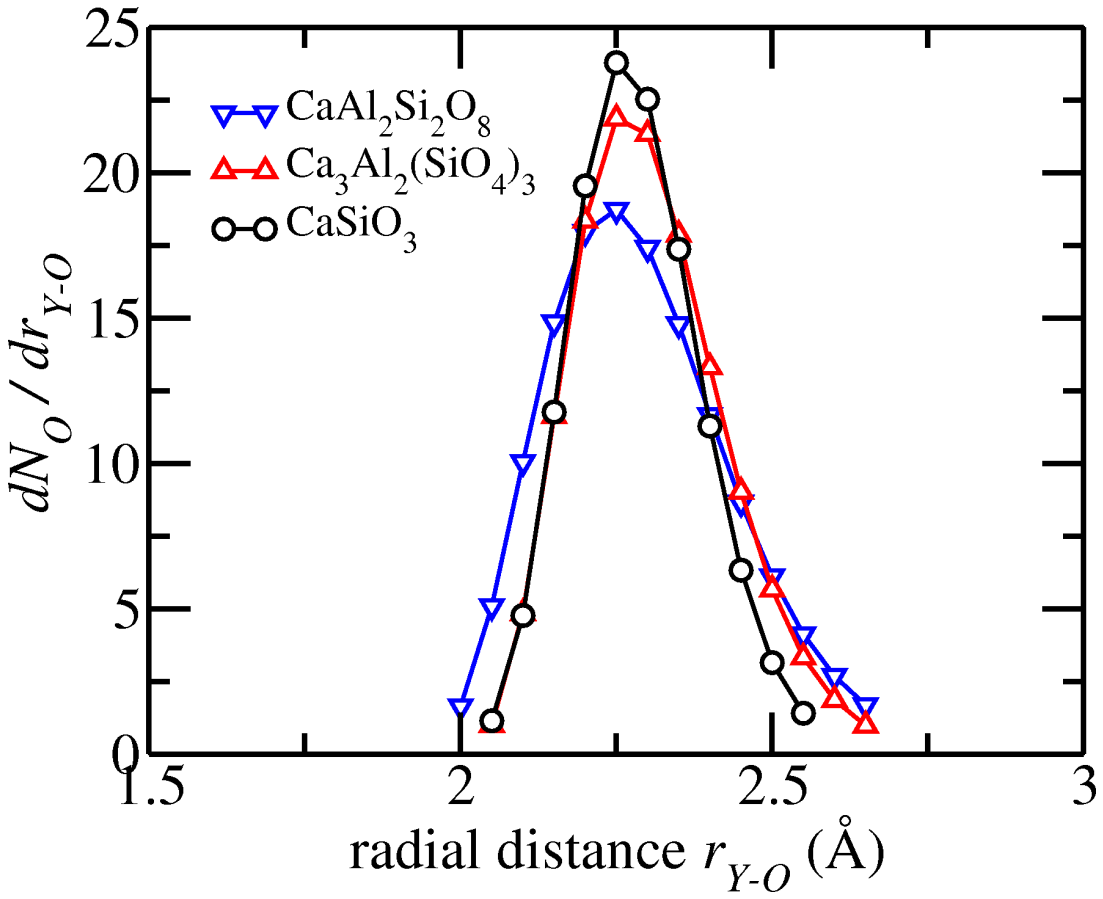

Figure 3.6: Distribution of O around Y in three silicate melts as obtained from EXAFS spectroscopy (for details see Simon et al. in this issue). The area under a curve up to a certain distance r_{Y-O} gives the number N_O of oxygen atoms within a sphere of radius r_{Y-O} around Y. Note the change of scale of the ordinate axis with respect to Fig. 3.4. Lines are a guide to the eye.

In order to confirm that the observed differences between simulation and experiment are largely due to differences between melts and glasses, and not to deficiencies of our interaction potential, we also simulated $Ca_3Al_2(SiO_4)_3$ glass, containing a single Y atom, at 300 K. We circumvented the problem of insufficient sampling of the phase space by running a simulation at 3000 K, picking 100 configurations from this simulation and quenching them separately to 300 K. With this procedure, different Y environments (sampled in the high-temperature run) are "frozen" into the glass structures, and the average over the 100 resulting glass structures should yield a representative description of Y in $Ca_3Al_2(SiO_4)_3$ glass. Note however, that due to the limited simulation time, the quench rate in the simulation was $-2.5 \cdot 10^{11}$ K/s, much larger than in the experiments. This means that the simulated glass formed at a higher fictive temperature and therefore probably still has a slightly different structure than the glass analyzed by EXAFS spectroscopy. We found an average Y-O distance of 2.38 Å in the simulated glass, to be compared with 2.31 Å obtained from experiment (and 2.49 Å in the simulated melt at 3000 K). The coordination number of Y was found to be 6.1 (compared to 6.6 in the melt). The satisfying agreement with experiment further corroborates the adequacy of our interaction potential in predicting glass and

melt structures.

3.4.3 Y partitioning between silicate melts

In section 3.4.1, we suggested a qualitative explanation for the preference of Y for less polymerized melts in terms of competition for bonding. Now we turn to a more quantitative description of element partitioning and consider the free energy balance which accompanies the process. For trace element incorporation in crystals, the lattice strain model (Blundy and Wood (1994)) provides a link between the structural changes induced by the incorporation (strain) and the associated energy costs, and these determine the influence of the crystal on partitioning. However, in melts, there is no such obvious link, due to the lack of well-defined lattice sites. We therefore chose a more general approach and applied the method of thermodynamic integration, by which we calculated the change in Gibbs free energy upon replacing a major element cation in the melt (Al) by a trace element (Y), and like in crystals, this change in Gibbs free energy governs partitioning. More precisely, we modeled the exchange reaction of Y^{3+} and Al^{3+} between Al_2SiO_5 melt and $CaAl_2Si_2O_8$ melt, as described in section 3.3.3:

$$\begin{aligned} &Y^{3+} \text{ in } Al_2SiO_5 + Al^{3+} \text{ in } CaAl_2Si_2O_8 \\ &\rightleftharpoons Al^{3+} \text{ in } Al_2SiO_5 + Y^{3+} \text{ in } CaAl_2Si_2O_8 \end{aligned} \tag{3.14}$$

By choosing this melt pair, we by no means want to suggest that these melts coexist as immiscible phases in nature or experiment. Rather they serve as a simplified model system on which the mechanism and the energetics of trace element distribution can be studied. Moreover, even hypothetical partitioning between two melts provides information about partitioning between mineral and melt: if one is interested in the *relative change* of trace element distribution between a mineral (with constant chemistry) and melts of varying compositions (see, e.g., Prowatke and Klemme (2005)), the problem can be reduced to partitioning between the different melts, because the contribution of the mineral cancels out. The equilibrium constant of reaction (3.14) is well-defined thermodynamically and reflects the fractionation tendency of Y and Al between the two melts. We suggest to view Al_2SiO_5 as highly polymerized in the sense that the ratio NBO/(Si+Al) is 0, whereas for $CaAl_2Si_2O_8$, we found NBO/(Si+Al) = 0.14 in the simulation and thus consider it less polymerized (although nominally fully polymerized). The presence of a significant amount of NBO in glasses of this composition has also been confirmed by NMR experiments (Stebbins and Xu, 1997).

The thermodynamic integration was carried out numerically, interpolating the five data points, corresponding to five values of λ, for each system with a 4th order polynomial (Fig. 3.7). The change in free energy for the transmutation $Y^{3+} \longrightarrow Al^{3+}$ is given by the integral in Eq. 3.13, i.e. the area between a curve and the x axis, and is found to be negative in both Al_2SiO_5 and $CaAl_2Si_2O_8$ (areas below the x axis are counted as negative). This indicates that incorporation of Y is energetically less favorable in both cases than incorporation of Al. However, in Al_2SiO_5, it is unfavorable to a higher degree, and thus the overall minimization of the Gibbs free energy dictates partitioning of Y into $CaAl_2Si_2O_8$.

Quantitatively, we obtained a total $\Delta G = (-66 \pm 2)$kJ/mol for the reaction (3.14). The negative sign indicates that the equilibrium is shifted to the right side, with Al enriched in the highly polymerized Al_2SiO_5 melt and Y incorporated preferentially into the less polymerized, Ca-bearing $CaAl_2Si_2O_8$. For $T = 2500$ K, the resulting equilibrium constant is $K = 24 \pm 2$. According to Eq. 3.10, it approximates the ratio of molar partition coefficients $D_{Y*}^{m2/m1}/D_{Al*}^{m2/m1}$ with m1 and m2 representing Al_2SiO_5 and $CaAl_2Si_2O_8$, respectively. If one assumes that ΔG does not vary a lot with temperature, the equilibrium constant will be $K = (200 \pm 30)$ at 1500 K, a temperature in the range usually covered in experiments.

Since the equilibrium constant of the exchange reaction (3.14) is related to a *ratio* of partition coefficients, we are cautious with making statements about $D_{Y*}^{m2/m1}$ itself. However, Veksler et al. (2006) found that the partition coefficients of Al between two immiscible silicate melts are not too far from 1 (and much closer to unity than the partition coefficients of REE). If we assume that this also holds for our

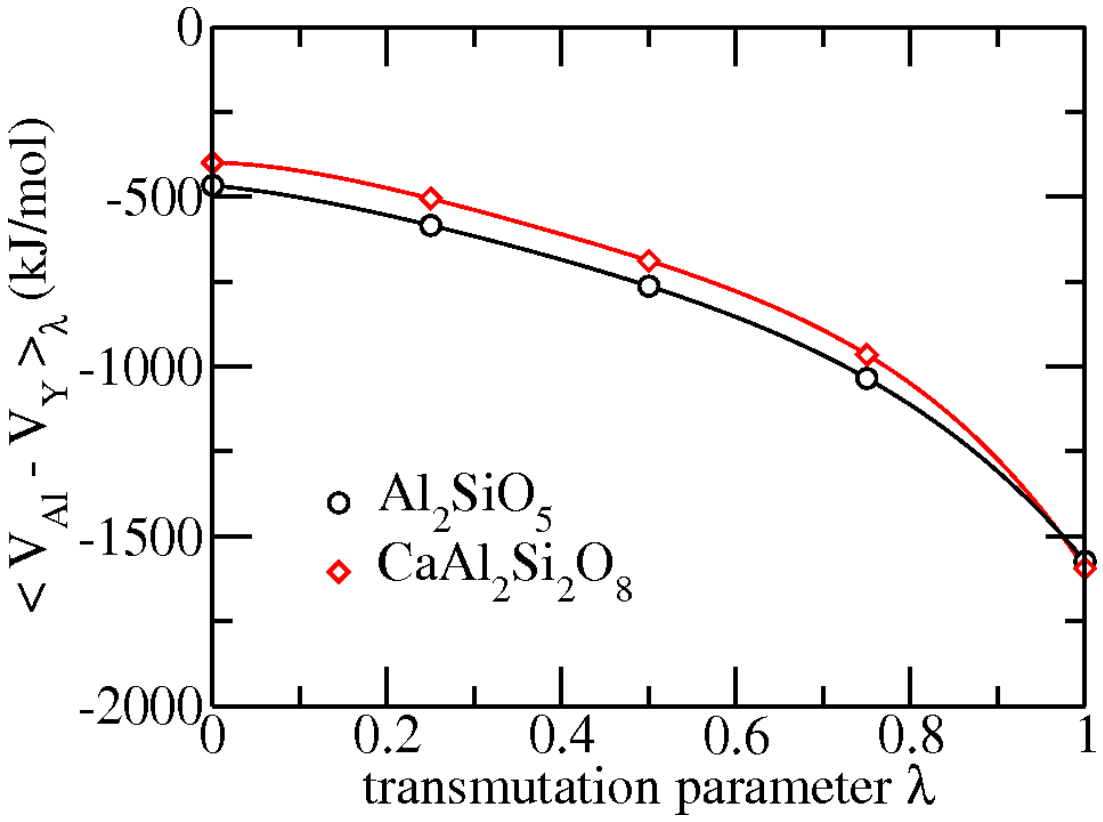

Figure 3.7: Thermodynamic integration for the exchange reaction of Y and Al between Al_2SiO_5 and $CaAl_2Si_2O_8$ melt (Eq. 3.13). The data points represent the average potential energy difference $\langle V_{\mathrm{Al}} - V_{\mathrm{Y}} \rangle_\lambda$ for the two compositions as a function of the transmutation parameter λ. The curves are 4th order polynomial interpolations to the data. Either of the curves represents one of the transmutations or partial reactions in eq. 3.11. The area between the two curves corresponds to the total change in Gibbs free energy, ΔG, for the complete exchange reaction.

system, then our result indicates $D_{Y*}^{m2/m1} > 1$. This finding is in agreement with the observed preference of Y (and other REE) for more depolymerized melts. It is also in line with our interpretation of the structural data in section 3.4.1, where we argued that the presence of Ca (a "weak competitor") facilitates the incorporation of Y into the melt.

3.5 Conclusions

We combined MD simulations and EXAFS spectroscopy to investigate the structural environment of Y as a trace element in silicate melts of varying composition. For the MD, a new interaction potential including polarization was constructed for the system Y-Ca-Al-Si-O, which proved to be accurate, transferable and computationally efficient. The simulations revealed two structural trends: First, the average coordination number of Y decreases when the melt polymerization decreases (i.e. when the Ca content increases). This change is accompanied by a decrease of the average Y-O distance by about 4%, and at the same time, oxygen disorder around Y is reduced. A very similar variation is also seen in EXAFS experiments on glasses, which corroborates the reliability of the simulation results.

Second, the MD simulations for the three Ca-bearing melts indicate that the second (cationic) coordination shell around Y exhibits a larger Ca/(Si+Al) ratio than the bulk composition. In other words, Y tends to form clusters with the network modifier Ca, which implies that for a given melt, it is energetically more favorable for Y to share oxygen with Ca than with the network formers Si and Al. This, in turn, suggests that, given *two* melts of different composition, Y should partition preferentially into the one with larger Ca/(Si+Al) ratio, i.e. into the less polymerized melt. Indeed, modeling the exchange reaction of Y and Al between a Ca-free and a Ca-bearing melt by means of thermodynamic integration, we confirmed that minimization of Gibbs free energy drives Y into the Ca-bearing melt.

In summary, using simple systems, we presented computational and experimental evidence on how the influence of melt composition on trace element partitioning can be rationalized in terms of atomic-scale processes. We found a systematic influence of melt composition on the microscopic melt structure around Y and investigated the energetic implications of structural changes. The exemplary result that Y incorporation into melts is facilitated by the presence of network modifiers is consistent with the general observation that REE prefer depolymerized melts to polymerized ones. Although most systems which are studied experimentally, and Nature itself, are more complex than the melts investigated in this study, we still hold that the underlying mechanisms are the same in both cases.

3.6 Acknowledgments

This work was funded by the German Research Foundation DFG (grants JA1469/4-1 and WI2000/6-1). The calculations were in part performed on JUROPA and JUGENE at the Jülich Supercomputing Centre under the NIC project grant HPO15. Part of the work was carried out under the HPC-EUROPA2 project (project number: 228398) with the support of the European Commission Capacities Area - Research Infrastructures Initiative. We also acknowledge support from DAAD-PROCOPE under grant no. D/9811428.

Chapter 4

Thermal conductivity of MgO, $MgSiO_3$ perovskite and post-perovskite in the Earth's deep mantle

4.1 Abstract

We report lattice thermal conductivities of MgO and $MgSiO_3$ in the perovskite and post-perovskite structures at conditions of the Earth's lower mantle, obtained from equilibrium molecular dynamics simulations. Using an advanced ionic interaction potential, the full conductivity tensor was calculated by means of the Green-Kubo method, and the conductivity of $MgSiO_3$ post-perovskite was found to be significantly anisotropic. The thermal conductivities of all three phases were parameterized as a function of density and temperature. Assuming a Fe-free lower-mantle composition with mole fractions $x_{MgSiO_3} = 0.66$ and $x_{MgO} = 0.34$, the conductivity of the two-phase aggregate was calculated along a model geotherm. It was found to vary considerably with depth, rising from 9.5 W/(mK) at the top of the lower mantle to 20.5 W/(mK) at the top of the thermal boundary layer above the core-mantle boundary. Extrapolation of experimental data suggests that at deep-mantle conditions, the presence of a realistic amount of iron impurities lowers the thermal conductivity of the aggregate by about 50% (Manthilake et al., 2011a). From this result and our thermal conductivity model, we estimate the heat flux across the core-mantle boundary to be 10.8 TW for a Fe-bearing MgO/$MgSiO_3$ perovskite aggregate and 10.6 TW for a Fe-bearing MgO/$MgSiO_3$ post-perovskite aggregate.

4.2 Introduction

The thermal conductivity of minerals in the Earth's mantle is an important geophysical parameter which governs the heat flux from the core up to the surface and hence strongly influences mantle dynamics (Naliboff and Kellogg, 2007). Moreover, the thermal conductivity of minerals at the core-mantle boundary (CMB) determines the amount of heat extracted from the core, driving the convection of the liquid outer core and thus controlling the power available to the generation of the Earth's magnetic field (Davies, 2007; Aubert et al., 2009). Yet, measuring thermal conductivities at mantle pressures and temperatures is extremely challenging, and experimental data are scarce. Several schemes exist to extrapolate thermal conductivities measured at lower pressures and temperatures to deep-mantle conditions (Ross et al., 1984; Hofmeister, 1999), but they are plagued with large uncertainties. Hence a computational approach is desirable to evaluate thermal conductivities directly at the relevant conditions. The aim of this study is to provide reliable values for the lattice thermal conductivities of MgO, $MgSiO_3$ perovskite (Pv) and post-perovskite (PPv) at lower-mantle conditions and their variation with temperature and density (or

pressure). These results can be directly applied to thermal transport in the lower mantle.

In deep-mantle minerals, heat is conducted by phonons and electromagnetic radiation. The importance of the radiative contribution to thermal transport in the Earth is under debate, and current estimates span a considerable range: while Goncharov et al. (2009) report a radiative thermal conductivity below ~ 0.5 W/(mK) across the lower mantle, Stamenković et al. (2011) predict ~ 5 W/(mK) at the CMB, and Keppler et al. (2008) even values of up to ~ 10 W/(mK), which is of the same order of magnitude as the lattice contribution. Moreover, the radiative conductivity seems to depend strongly on crystal grain size and on the iron content (Hofmeister and Yuen, 2007). In view of these difficulties, we focus on the lattice contribution in this study. If the radiative conductivity turns out to be significant it can simply be added to the lattice part presented here.

Over the past years, different atomic-scale methods were developed to calculate lattice thermal conductivities. Stackhouse et al. (2010) applied the non-equilibrium or "direct" method (Müller-Plathe, 1997; Nieto-Draghi and Avalos, 2003) to derive the thermal conductivity of MgO, using molecular dynamics (MD) simulations based on density functional theory (DFT). In this approach, an energy current from the cold to the hot side of the simulation cell is imposed. From this current and the steady-state temperature gradient which builds up, the thermal conductivity is obtained via Fourier's law. While computationally rather efficient, the method suffers from strong finite-size effects, thus requiring extrapolation to infinite system size and introducing considerable uncertainties (Sellan et al., 2010). An approach based on phonon lifetimes, obtained from DFT, was used by de Koker (2009, 2010) and by Tang and Dong (2010) to calculate the thermal conductivity of MgO. Phonon lifetimes were either calculated from line widths in the Fourier transform of the velocity autocorrelation function (de Koker, 2009) or from anharmonic lattice dynamics (Tang and Dong, 2010). Combined with the Boltzmann transport equation for the phonon gas, they yield the thermal conductivity in the relaxation time approximation. This approach treats the anharmonicity of lattice vibrations perturbatively and is thus limited to temperatures where atomic displacements from the equilibrium positions are small enough for higher-order anharmonicity to be neglected.

A third approach, the Green-Kubo method, uses the Green-Kubo relations (Kubo, 1957) to obtain thermal conductivities from appropriate current correlation functions, which, in turn, are readily extracted from equilibrium MD trajectories. This method has been successfully applied to solids (e.g. Volz and Chen (2000); Sellan et al. (2010); Esfarjani and Chen (2011)) and liquids (e.g. Galamba et al. (2007); Ohtori et al. (2009b); Salanne et al. (2011)). In contrast to the non-equilibrium method, no concerns about leaving the linear-response regime arise for equilibrium MD. Moreover, the Green-Kubo method exhibits a weaker finite-size effect (Sellan et al., 2010), provides the full thermal conductivity tensor in one simulation and takes into account thermoelectric effects which can contaminate results of the non-equilibrium method for ionic conductors (Salanne et al., 2011). Unlike the lattice dynamics approach, the Green-Kubo method takes into account anharmonicity to all orders. Thus its validity is not restricted to low temperatures. In the light of these advantages, we decided to use the Green-Kubo approach to calculate thermal conductivities of MgO, $MgSiO_3$ Pv and $MgSiO_3$ PPv at conditions spanning a wide pressure and temperature range. We also determined conductivities at conditions where experimental data are available, and satisfactory agreement with these experiments makes us confident that our results are equally reliable at CMB conditions. A drawback of the method is that it requires long run durations (in the nanosecond range) to obtain reasonable statistical accuracy. Our calculations are based on classical MD simulations involving an interaction potential of first-principles accuracy (Jahn and Madden, 2007).

4.3 Theory

The thermal conductivity tensor λ is defined by Fourier's law, $\mathbf{j}_Q = -\lambda \nabla T$, under the constraint that no mass or electric currents are present. This constraint is relevant to electronic or ionic conductors, where

thermoelectric effects occur (Callen, 1985). Fourier's law is of linear-response type and relates the heat current density $\mathbf{j}_Q$ to the temperature gradient ∇T. For cubic and orthorhombic crystals, λ is diagonal if the coordinate axes are along the crystal axes, and direction-dependent conductivities can be defined by

$$\lambda_\alpha = -j_Q^\alpha / \nabla_\alpha T, \ \alpha \in \{x,y,z\} \tag{4.1}$$

In the framework of non-equilibrium thermodynamics (Callen, 1985; de Groot and Mazur, 1984), the thermal conductivity can be expressed in terms of kinetic coefficients L_{AB}, as is done in equations 4.3 and 4.4 below. They determine the linear response of the system to deviations from equilibrium, i.e. energy and mass flows resulting from thermal and chemical gradients. The gist of the Green-Kubo method is that the kinetic coefficients L_{AB}, although representing non-equilibrium behavior, are linked to fluctuations in thermodynamic *equilibrium* via the fluctuation-dissipation theorem. The kinetic coefficients, and hence the thermal conductivity, can therefore be obtained from equilibrium MD by means of appropriate Green-Kubo formulae, which relate the linear response of a system with volume V to current correlation functions in thermodynamic equilibrium:

$$L_{AB}^{\alpha\beta} = \lim_{\tau\to\infty} \left[\frac{1}{k_B V} \int_0^\tau dt \, \langle J_A^\alpha(t) J_B^\beta(0) \rangle \right] \tag{4.2}$$

where k_B is Boltzmann's constant, and the J_A^α are Cartesian components of the energy current ($A = U$) or of the mass currents ($A = 1,\ldots,N-1$, where N is the number of chemical species in the system), with respective dimensions of energy or mass times velocity. Angular brackets denote an ensemble average. We assume that the center of mass is at rest, hence there are only $N-1$ independent mass currents for a system with N chemical species. Then, for a system with two species, the thermal conductivity is given by (Galamba et al., 2007),

$$\lambda_\alpha = \frac{1}{T^2} \left(L_{UU}^{\alpha\alpha} - \frac{(L_{U1}^{\alpha\alpha})^2}{L_{11}^{\alpha\alpha}} \right), \alpha \in \{x,y,z\} \tag{4.3}$$

and for a system with three species by (Salanne et al., 2011)

$$\begin{aligned} \lambda_\alpha = & \frac{1}{T^2} (L_{UU}^{\alpha\alpha} - \\ & \frac{(L_{U1}^{\alpha\alpha})^2 L_{22}^{\alpha\alpha} + (L_{U2}^{\alpha\alpha})^2 L_{11}^{\alpha\alpha} - 2 L_{U1}^{\alpha\alpha} L_{U2}^{\alpha\alpha} L_{12}^{\alpha\alpha}}{L_{11}^{\alpha\alpha} L_{22}^{\alpha\alpha} - (L_{12}^{\alpha\alpha})^2} \Big) \end{aligned} \tag{4.4}$$

It is worth noting that equations 4.3 and 4.4 are written here in terms of mass currents, whereas they were originally derived in terms of ionic currents.

4.4 Simulation details

We performed equilibrium molecular dynamics simulations in the NVT ensemble, with a time step of 1 fs for the integration of the equation of motion and a Nosé-Hoover thermostat (Nosé, 1984; Hoover, 1985) maintaining the system at the desired temperature. The cell dimensions were chosen as the average cell size in a previous NPT run at the desired pressure P, maintained by a barostat (Martyna et al., 1994). The interactions between atoms were described by an advanced ionic interaction potential which was parameterized non-empirically, using DFT as a reference (Jahn and Madden, 2007). This potential has been shown to reliably predict properties of minerals of the system CaO-MgO-Al_2O_3-SiO_2 over a wide temperature and pressure range, with accuracy comparable to DFT. In particular, the ionic interaction potential used in this study was shown to describe MgO and the $MgSiO_3$ phases perovskite and post-perovskite well, predicting lattice constants to within 1% and elastic constants mostly to within 10%, compared to DFT results (Jahn and Madden, 2007). The elastic constants determine vibrational modes

of the crystal in the limit of long wavelengths (Ashcroft and Mermin, 1976). These modes close to the Brillouin zone center, in turn, are expected to make the largest contribution to the thermal conductivity of the crystal (Tang and Dong, 2010). Therefore, we expect the interaction potential to produce accurate lattice dynamics and thermal transport properties. For MgO, $MgSiO_3$ Pv, and $MgSiO_3$ PPv, we used cubic or orthorhombic supercells containing 512, 960, and 720 atoms, respectively. For each composition, temperature, and pressure, we generated trajectories of at least 0.5 ns and up to 2.4 ns.

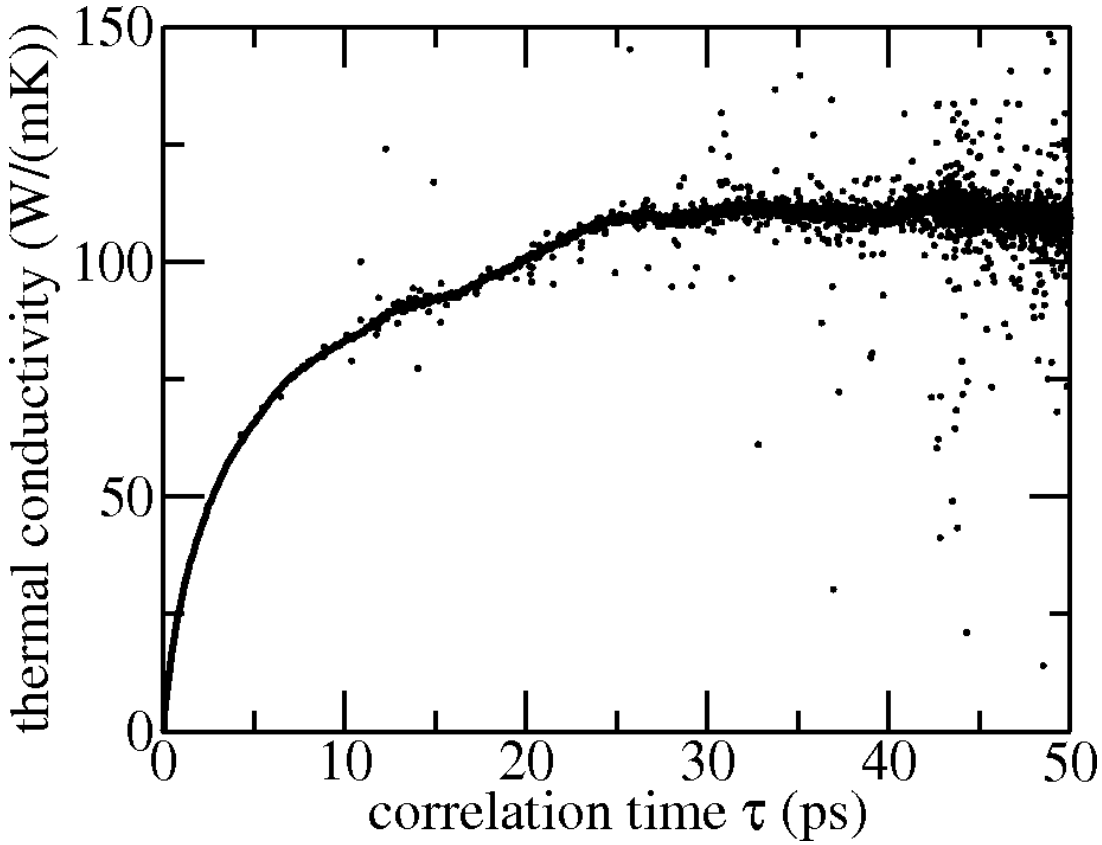

Figure 4.1: Thermal conductivity of MgO at 300 K, 0 GPa as a function of correlation time τ, see eq. 4.2, averaged over 15 MD blocks of 100 ps each. Clearly, a plateau is reached at 30 ps.

At each time step of the MD run, the mass currents for each species and the energy current were extracted for later calculation of the different current correlation functions needed in Eq. 4.2. An explicit expression for the energy current for polarizable ions was derived by Ohtori et al. (2009b). The total MD run was then divided into blocks of equal length (50 to 100 ps) which were analyzed independently for current correlation functions and thermal conductivity. The correlation time τ in Eq. 4.2 was chosen large enough for the thermal conductivity λ to reach convergence. In practice, λ as a function of τ oscillates around its limiting value, and for each MD block, we took a time average over the first plateau of the cumulative $\lambda(\tau)$ (averaged over the $\lambda(\tau)$ from the individual MD blocks), see Fig. 4.1. Finally, the thermal conductivity and its 1σ uncertainty were obtained by averaging the results from all blocks.

4.5 Results and discussion

4.5.1 MgO

For reference, we first calculated the thermal conductivity of isotopically pure MgO in the fcc structure at 300 K and ambient pressure. At these conditions, the model predicts a density ρ = 3.602 g/cm^3, which is in excellent agreement with the experimental density at ambient conditions, 3.583 g/cm^3 (Speziale et al., 2001). In Fig. 4.1, we show the computed thermal conductivity as a function of correlation time τ, see Eq. 4.2. The data contain a number of outliers, due to the second term on the right side of Eq. 4.3. Both L_{U1} and L_{11} are expected to be close to zero when no diffusion is present, thus the quotient may take on very large positive or negative values occasionally, although it should be small in a crystal. Since outliers tend to distort arithmetic averages, we calculated the conductivity for each MD block from the median of the data over the plateau, which is a more representative measure for the expectation value in such cases.

Our value of the thermal conductivity at ambient conditions is (111 ± 16) W/(mK), significantly larger than that found in other computational and experimental studies (table 4.1). However, overestimation with respect to experiments is to be expected, since we considered a perfect, isotopically pure crystal, whereas the experiments were performed on real crystals with natural isotopic composition and defects, which reduces the thermal conductivity considerably relative to its perfect-crystal value (Kremer et al., 2004; Tamura, 1983). Therefore, our results should indeed be larger than the experimental ones. Tang and Dong (2010) evaluated the isotope effect for MgO and found that at ambient conditions, the thermal conductivity of an isotopically pure crystal exceeds the one of natural samples by as much as 46%. This correction for isotopic composition is already included in their results in table 4.1. If we apply the same correction to our data, we get λ_{MgO}(300K,0GPa) = (76 ± 11)W/(mK). Defects, impurities and grain boundaries in real crystals will further reduce the thermal conductivity, and thus our result is fully compatible with the measured conductivity of (65 ± 15) W/(mK) (Katsura, 1997). On the other hand, the computed values given by de Koker (2010) and in particular by Stackhouse et al. (2010) seem to fall at the low end of values reconcilable with experiments, as the computational data represent isotopically pure, perfect crystals and therefore should *not* agree with conductivities measured on real samples. Following Sellan et al. (2010), the relatively small value of Stackhouse et al. (2010) may be attributed to the use of a linear extrapolation to account for finite-size effects in the non-equilibrium MD method, which leads to a systematic underestimation of the thermal conductivity.

The thermal conductivity was evaluated at four more ρ, T points, up to lowermost-mantle conditions, $T = 3000$ K, $\rho = 5.307$ g/cm^3, see table 4.1. These data allow us to parameterize the behavior of thermal conductivity over a wide density and temperature range, including the conditions relevant to the lower mantle. The temperature and density dependence of the thermal conductivity is a highly complex matter, and no general theory is currently available (Ohtori et al., 2009a). The dependence on density can be described, in the framework of the Debye approximation, as $\lambda \propto \rho^a$, where a is itself a function of density and temperature in principle (de Koker, 2010). In a recent study, Manthilake et al. (2011b) tested the validity of different models for $a(\rho, T)$ by measuring the thermal conductivity of $CaGeO_3$ perovskite, which is an analog phase for $MgSiO_3$. They found subtle differences in the density dependence of a compared to the case of MgO, which they attributed to the larger number of optical phonons in the perovskite phase. However, in view of the limited number of data points in our present study, we take a to be constant, as in Stackhouse et al. (2010), which yields an effective a for the entire density range spanned by our data points. Concerning the temperature dependence, thermal conductivity approximately follows a power law $\lambda \propto T^{-b}$ at high temperatures (Ashcroft and Mermin, 1976). Following de Koker (2010) and Stackhouse et al. (2010), we write

$$\lambda(\rho, T) = \lambda_0 \left(\frac{\rho}{\rho_0}\right)^a \left(\frac{T_0}{T}\right)^b \tag{4.5}$$

with a fixed reference point $\rho_0 = 3.602$ g/cm^3, $T_0 = 300$ K, and free parameters λ_0, a, and b. The result of a least-square fit of Eq. 4.5 to the data points is given in table 4.2. The quality of the fit can be assessed by means of Fig. 4.2.

At the high temperatures prevailing at the CMB, anharmonicity, i.e. phonon-phonon scattering, is expected to be the dominant mechanism limiting the thermal conductivity, compared to other sources of phonon scattering like isotopic disorder, point defects, and grain boundaries. This is because the number of phonons present in the material increases with temperature and hence the mean free path between phonon-phonon collisions becomes shorter than the mean free path imposed by other scattering mechanisms. The reduction of the thermal conductivity due to isotopic disorder in MgO has been shown to decrease from 46% at room temperature to only 4% at 4000 K (Tang and Dong, 2010). Qualitatively the same behavior has been observed in experiments on other materials, see e.g. Kremer et al. (2004). In MD simulations, anharmonicity, i.e. the dominant scattering mechanism at high temperatures, is automatically included to all orders, and hence our conductivity results for a perfect crystal should be a good approximation for real MgO at CMB conditions. The same argument applies to the $MgSiO_3$ phases to which we turn in the following paragraphs. Although the above reasoning is based on sound physical considerations, we emphasize that more experimental or simulation data are needed to fully understand and quantify the influence of different kinds of defects on the thermal conductivity at high pressure and temperature.

4.5.2 $MgSiO_3$ perovskite

$MgSiO_3$ in the orthorhombic perovskite structure *Pbnm* is generally accepted to be the most abundant mineral in the Earth's lower mantle (i.e. below a depth of 670 km). It consists of a three-dimensional network of corner-sharing SiO_6 octahedra, with Mg occupying the larger inter-octahedral sites. The calculated thermal conductivity of $MgSiO_3$ in the perovskite structure, averaged over all directions, at four state points spanning a wide range of densities and temperatures, is given in table 4.1, along with available experimental data. The effect of isotopic disorder on the thermal conductivity is not known for the $MgSiO_3$ phases Pv and PPv. As in the case of MgO, it may be significant at low temperatures but is expected to decrease rapidly with temperature. The density and temperature dependence of thermal conductivity is well described by Eq. 4.5, and the respective fit parameters are listed in table 4.2. In Fig. 4.2, the model conductivity is plotted along with the computed data points.

The available experimental data for perovskite scatter considerably (table 4.1), and the effect of grain boundaries, isotopic disorder and other defects like possible cracks in the samples is not known quantitatively. Hence a comparison to our results is difficult. As expected, the results obtained from perfect-crystal simulations are larger than the experimental values. Our results seem compatible with those of Manthilake et al. (2011a) but more difficult to reconcile with the data of Ohta et al. (2012). Note that at 300 K and approximately 30 GPa, Ohta et al. (2012) report a considerably lower conductivity than Manthilake et al. (2011a): the data, both derived from measurements, differ by a factor of almost 2. At ambient conditions, Osako and Ito (1991) report the conductivity to be 5.1 W/(mK), which is in line with the value of 5.8 W/(mK), derived from a fit to experimental data by Ohta et al. (2012).

4.5.3 $MgSiO_3$ post-perovskite

The perovskite structure of $MgSiO_3$ transforms to an orthorhombic post-perovskite phase (*Cmcm*) at approximately 125 GPa and 2500 K (Murakami et al., 2004; Oganov and Ono, 2004) which is believed to be stable in the Earth's lowermost mantle close to the core-mantle boundary and might be responsible for the D$''$ seismic discontinuity (Iitaka et al., 2004). It is characterized by layers of corner- and edge-sharing SiO_6 octahedra perpendicular to the *b* axis, with Mg occupying inter-layer sites. This anisotropic structure exhibits strongly anisotropic elastic properties (Iitaka et al., 2004), which should lead to direction-dependent phonon velocities, and hence we expect anisotropic thermal transport properties. Therefore, in

Table 4.1: Thermal conductivity of fcc MgO, $MgSiO_3$ Pv, and $MgSiO_3$ PPv. P_{MD} is the pressure resulting from our MD simulations with the indicated density and temperature, and P_{EoS} the one obtained from an equation of state by Stixrude and Lithgow-Bertelloni (2005). Results are from this study if not otherwise indicated. For the last ρ, T point of PPv, the three directional conductivities average to (15.3 ± 0.8) W/(mK), to be compared with the calculated bulk λ of (15.1 ± 0.9) W/(mK). The difference, which is safely within the error bars, results from slightly different averaging schemes: for the bulk value, we first averaged over all directions and then over time (i.e. over the plateau, see Fig. 4.1), whereas for the direction-dependent conductivities, we averaged each direction individually over the plateau.

phase	ρ (g/cm^3)	T (K)	P_{MD} (GPa)	P_{EoS} (GPa)	λ (W/(mK))
MgO	3.602	300	0	1	111 ± 16
					76 ± 11 [a]
					62 [b]
					59 ± 6 [c]
					75 [d]
					65 ± 15 [e]
	5.410	300	134	151	1400 ± 250
	4.201	2000	41	45	40.0 ± 2.5
	5.307	2000	133	148	141 ± 11
	5.307	3000	138	155	76.8 ± 4.4
$MgSiO_3$ Pv	4.544	300	26	31	27.0 ± 2.2
				26	19 [f]
				31	10.6 ± 0.6 [g]
	5.332	300	107	111	61.3 ± 7.9
				108.4	23.7 ± 4 [g]
	4.544	2000	40	42	9.7 ± 1.0
	5.401	3000	139	137	12.4 ± 2.0
		300	–	ambient	5.1 [h]
		300	–	ambient	5.8 [i]
$MgSiO_3$ PPv	5.631	298	135	138	167 ± 25
				141	65 ± 14 [g]
	5.482	2000	130	132	16.8 ± 0.5
	5.631	2000	150	150	20.6 ± 1.7
	5.482	3000	138	140	15.1 ± 0.9
					λ_x: 18.0 ± 1.8
					λ_y: 13.7 ± 1.0
					λ_z: 14.1 ± 1.2

[a] This study, with isotope correction from Tang and Dong (2010)
[b] Tang and Dong (2010), DFT, with isotope correction
[c] Stackhouse et al. (2010), DFT, perfect crystal
[d] de Koker (2010), DFT, perfect crystal
[e] Katsura (1997), experiment at ambient conditions
[f] Manthilake et al. (2011a), experiment at 300 K
[g] Ohta et al. (2012), experiment at 300 K, pressure determined experimentally
[h] Osako and Ito (1991), experiment at 300 K, metastable (quenched to ambient pressure)
[i] Ohta et al. (2012), high-P experiments, extrapolated to ambient pressure

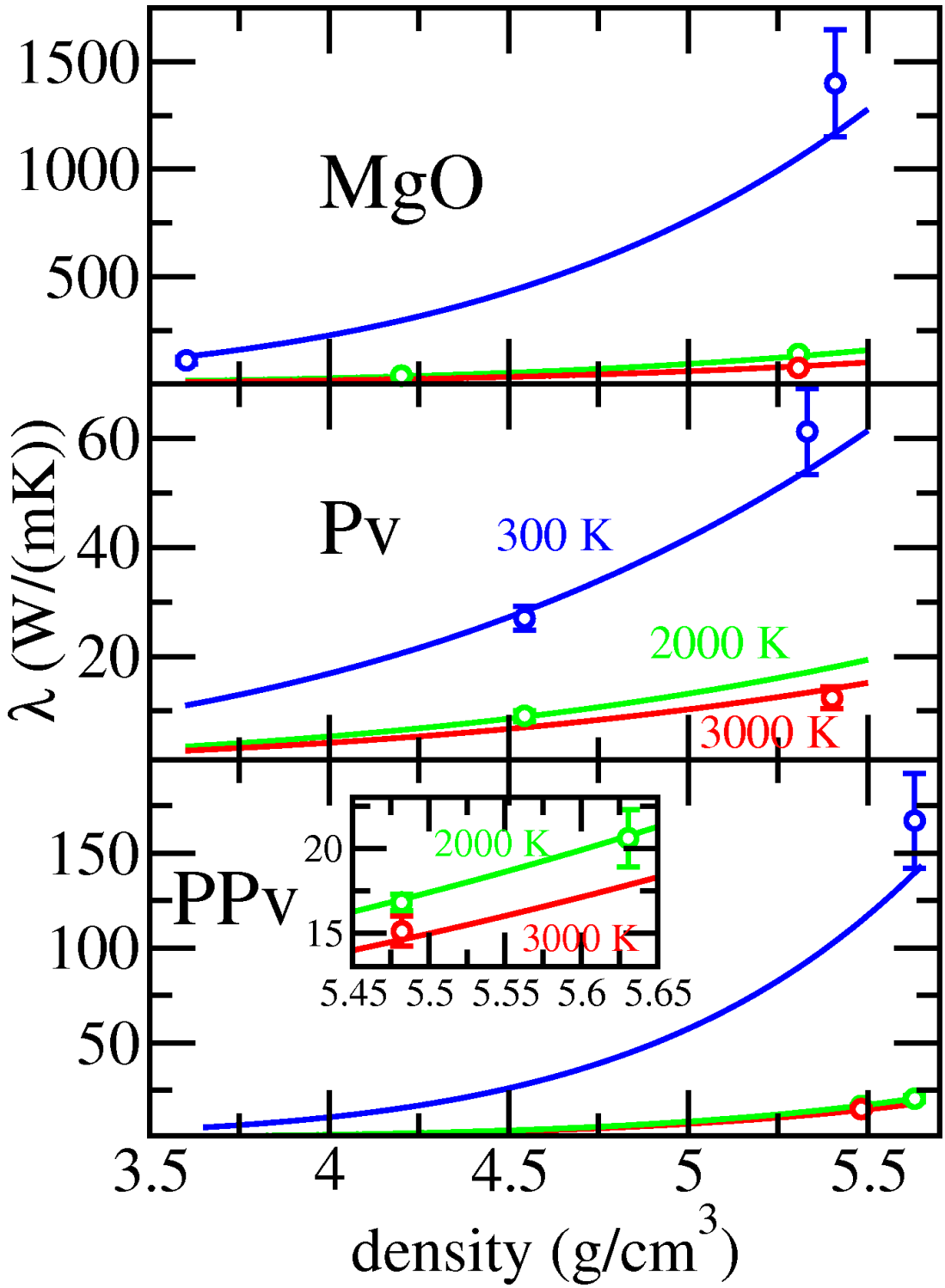

Figure 4.2: Density and temperature dependence of the thermal conductivity for MgO, Pv and PPv. Data points are results of our MD simulations. Lines are fits to eq. 4.5 (MgO, Pv) or eq. 4.6 (PPv), with colors representing different temperatures. Blue: 300 K, green: 2000 K, red: 3000 K. Inset: PPv at conditions relevant to the lower mantle.

Table 4.2: Parameters for the density and temperature dependence of thermal conductivity resulting from fits to our calculated data points, for MgO in fcc structure, $MgSiO_3$ Pv (both described by Eq. 4.5) and PPv, described by Eq. 4.6. Reference density ρ_0 and temperature T_0 are fixed during the fit.

	ρ_0 (g/cm^3)	T_0 (K)	λ_0 (W/(mK))	a	b
MgO	3.602	300	129	5.42	1.10
$MgSiO_3$ Pv	4.544	300	28.3	4.06	0.608
$MgSiO_3$ PPv	5.482	3000	14.6	7.48	0.327

addition to the direction-averaged conductivity, we also calculated the thermal conductivities separately along the three axes of the orthorhombic crystal for one data point, at conditions representative of the lowermost mantle. The simulation time was extended to 2.35 ns in this case to ensure satisfying statistics for each direction individually. The results for several ρ, T values are listed in table 4.1.

The calculated data points could not be fit satisfactorily with Eq. 4.5, due to the very weak temperature dependence of the thermal conductivity above 2000 K (compare the second and fourth data point of PPv in table 4.1). This flattening of the thermal conductivity as a function of temperature is consistent with experimental observations which show a near-constant conductivity above a certain temperature, depending on the material studied (Pertermann et al., 2008). In parameterizing the thermal conductivity of PPv, we therefore used an expression which reconciles a strong temperature dependence at lower temperatures with a flat behavior at high temperatures. A good fit could be obtained with the following functional form:

$$\lambda(\rho,T) = \lambda_0 \left(\frac{\rho}{\rho_0}\right)^a \left(\frac{T_0}{T-295\mathrm{K}}\right)^b \left(\frac{T_0-295\mathrm{K}}{T_0}\right)^b \tag{4.6}$$

where ρ_0 and T_0 are fixed reference values and λ_0, a, and b are fitting parameters, and the last (normalizing) factor ensures that $\lambda(\rho_0,T_0) = \lambda_0$. The results of a least-square fit are listed in table 4.2 and compared to the data in Fig. 4.2. Due to the somewhat empirical nature of the assumed temperature dependence, the validity of Eq. 4.6 is restricted to the temperature range covered by our data points. It can certainly not be applied below 298 K: in fact, the expression diverges at $T = 295$ K. However, we stress that all data points are well fitted. In particular, the density and temperature dependence at conditions of the lower mantle is well captured by the model, as can be seen from the inset in Fig. 4.2.

The calculated conductivity at conditions of the lowermost mantle is clearly anisotropic, and it is lowest in the y direction (along the b axis of the crystal). This is consistent with the fact that the crystal is softer along b (perpendicular to the layers formed by corner- and edge-sharing SiO_6 octahedra) than along a and c (in the plane of the SiO_6 sheets). This leads to lower phonon velocities along b, at least close to the Brillouin zone center, and a reduced conductivity.

The thermal conductivity of (167 $\pm$ 25) W/(mK), obtained at 300 K and $\rho = 5.631$ g/cm^3, is considerably higher than the value derived from experiments at similar conditions by Ohta et al. (2012), which is (65 $\pm$ 14) W/(mK) (table 4.1). Although we cannot quantify the effect of defect scattering in their polycrystalline PPv sample of natural isotopic composition, the discrepancy seems too large to be completely explained by this mechanism, and its origin remains unclear. We note however, that in the case of perovskite, the thermal conductivity reported by Ohta et al. (2012) was much lower than the experimental value by Manthilake et al. (2011a). Interestingly, the estimate of Ohta et al. (2012) for the thermal conductivity of PPv at 3000 K and 135 GPa, based on an assumed temperature dependence, is close to and even slightly higher than our result at similar conditions (19.5 W/(mK) and 15.1 W/(mK), respectively). This agreement at high T may partially be due to a fortuitous cancellation of discrepancies, since Ohta et al. (2012) assumed a different temperature dependence than the one we found. But it also hints at the fact that differences between perfect-crystal simulations and real-sample experiments

become less important with increasing temperature.

4.6 Implications for the thermal conductivity of the Earth's lower mantle

When applying our results to heat transport in the Earth's deep mantle, they should be considered upper estimates for the lattice thermal conductivities of real minerals. Our calculations do not take into account the natural isotopic composition, impurities, and defects of the minerals, all of which lower the conductivity. Manthilake et al. (2011a) measured the effect of realistic amounts of iron impurities on the thermal conductivity of MgO and $MgSiO_3$ perovskite, at relatively low temperatures and pressures. By extrapolation, they estimate that 20 mol% and 3 mol% of iron in MgO and perovskite, respectively, reduce the thermal conductivity of the aggregate at the CMB by about 50% relative to that of the chemically pure aggregate. On the other hand, we did not take into account radiative heat transport as an additional mechanism of thermal conduction.

To calculate the thermal conductivity in the lower mantle, we assumed a simplified mantle composition, derived from the pyrolitic composition given by Piazzoni et al. (2007), with molar fractions $x_{MgSiO_3} = 0.66$ (perovskite structure) and $x_{MgO} = 0.34$. The conductivities were calculated along a mantle geotherm, with the depth-dependent pressure taken from the Preliminary Reference Earth Model (Dziewonski and Anderson, 1981) and the temperature profile adopted from Stacey and Davis (2008). Since our model for thermal conductivities was parameterized as a function of density and temperature, the pressures along the geotherm had to be converted to densities. This was done by means of equations of state for the mineral phases, described by Stixrude and Lithgow-Bertelloni (2005), with a revised set of parameters for that model taken from Xu et al. (2008). The pressures resulting from the equations of states for a given density and temperature agree well with the pressures obtained directly from our MD simulations (table 4.1). This further corroborates the adequacy of the interaction potential used in the simulations in describing material properties over the ρ, T range of the lower mantle. By means of the equations of state, the mole fractions of the individual mineral phases can be converted to volume fractions, yielding about 82% Pv and 18% MgO by volume in the lower mantle. These numbers change slightly with pressure and temperature, and the exact values resulting from the equations of state have been used throughout the study.

The thermal conductivity of a two-phase aggregate, expressed in terms of the conductivities, λ_1, λ_2, and volume fractions, $f_1, f_2, (f_1 + f_2 = 1)$, of the individual phases, depends on the geometric details of the assemblage. The extreme cases are realized by a structure of alternating parallel layers of the two phases, with a heat flux parallel and perpendicular to the layers, respectively. For the former case (a "parallel circuit"), the conductivity of the aggregate is maximum and given by the arithmetic or Voigt average $\lambda_{max} = f_1\lambda_1 + f_2\lambda_2$. For the latter (a "series circuit"), the conductivity takes on its minimum or Reuss average $\lambda_{min} = (f_1/\lambda_1 + f_2/\lambda_2)^{-1}$. For other geometries, not necessarily built from layers, the conductivity of the aggregate will lie within these bounds.

Fig. 4.3 shows the thermal conductivity of the $MgSiO_3$(Pv)-MgO aggregate along the model geotherm and, for comparison, of the $MgSiO_3$(PPv)-MgO aggregate close to the CMB. Thermal conductivity increases with pressure and decreases with increasing temperature, see Eq. 4.5. With increasing depth, the pressure effect dominates over the concomitant temperature rise, resulting in a net increase of the thermal conductivity. Only close to the CMB, the sharp rise in temperature in the thermal boundary layer reverses this trend. At 2891 km depth, i.e. at the CMB, with $P = 136$ GPa and $T = 3739$ K, the conductivity of a MgO/$MgSiO_3$ perovskite aggregate is predicted to lie between $\lambda_{min} = 13.7$ W/(mK) and $\lambda_{max} = 19.1$ W/(mK), depending on geometry, with average $\overline{\lambda} = 16.4$ W/(mK). With $MgSiO_3$ in the post-perovskite structure instead, we obtain $\lambda_{min} = 13.9$ W/(mK), $\lambda_{max} = 19.3$ W/(mK), and $\overline{\lambda} = 16.6$ W/(mK), i.e. changes are not significant. The value for the PPv/MgO aggregate is in good agreement with Ohta et al. (2012), who estimate the aggregate conductivity at 4000 K and 135 GPa to be approximately 16 W/(mK). Assuming that a realistic amount of iron impurities reduces the aggregate conductivities by

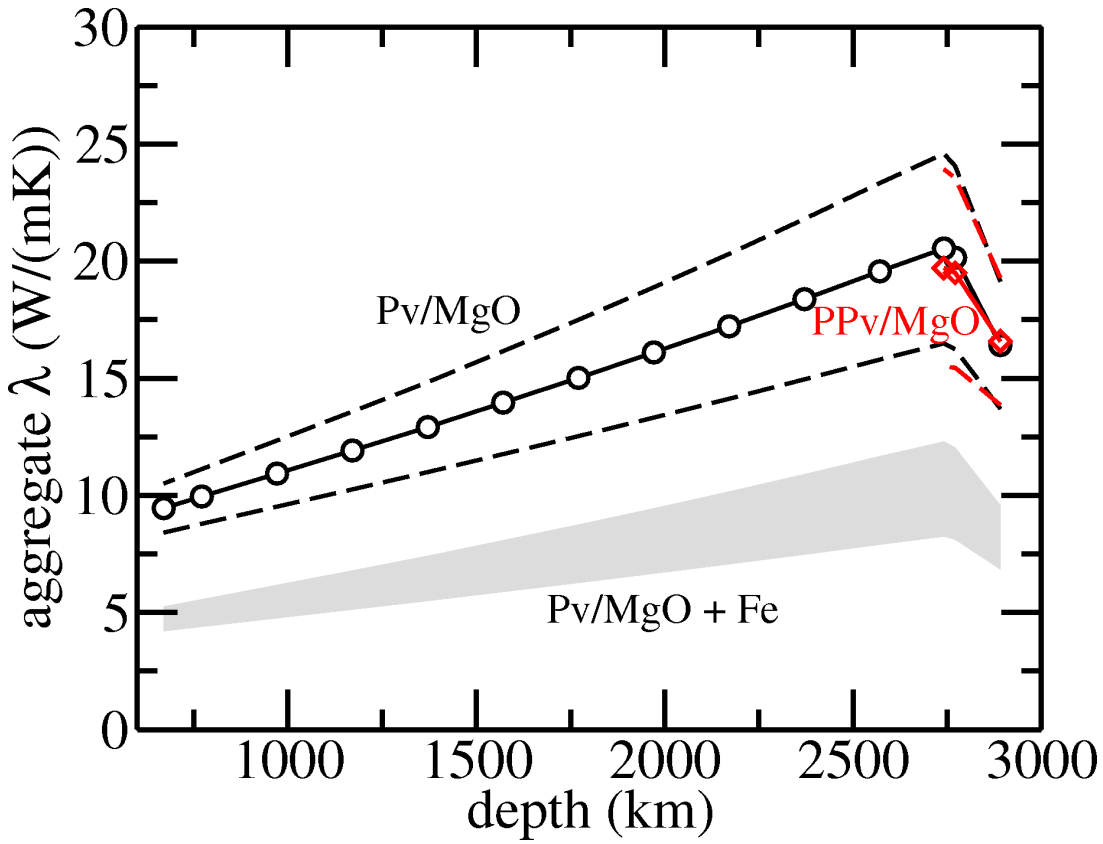

Figure 4.3: Average thermal conductivity $\overline{\lambda}$ along a model geotherm (Stacey and Davis, 2008) for an aggregate with mole fractions $x_{MgSiO_3} = 0.66$ (black circles: perovskite structure, red diamonds: post-perovskite strucutre) and $x_{MgO} = 0.34$. The dashed lines represent λ_{min} and λ_{max}, bracketing the geometry-dependent aggregate conductivity (see text). Lines are a guide to the eye. The grey-shaded area indicates the range of the Pv/MgO aggregate thermal conductivity under the assumption that iron in the Earth's lower mantle reduces the conductivity of the aggregate by 50% (Manthilake et al., 2011a).

50% (Manthilake et al., 2011a), the respective average conductivities at the CMB are 8.2 W/(mK) for the MgO/perovskite and 8.3 W/(mK) for the MgO/post-perovskite aggregate. The influence of iron on the thermal conductivity is treated approximatively here, and more data are needed to better quantify this effect at high pressures and temperatures.

Our results for the thermal conductivity across the lower mantle for an iron-free composition are in remarkable agreement with (albeit slightly larger than predicted by) the thermal conductivity model by Manthilake et al. (2011a) which is based on an extrapolation of low-P,T experimental data to CMB conditions, assuming an aggregate of 20% MgO and 80% Pv by volume. On the other hand, the model used by Hofmeister (1999) to extrapolate available conductivity data to high P,T (including iron) yields somewhat smaller values, ranging approximately between 4 W/(mK) and 7 W/(mK) across the lower mantle. Also the estimate of the lower-mantle thermal conductivity by Goncharov et al. (2009) lies below our data: for the lattice conductivity, they assumed an iron-free mantle composition (20% MgO and 80% Pv by volume) and extrapolated experimental data, finding a maximum lattice thermal conductivity $\lambda_{\max}$ varying from approximately 3 W/(mK) to 11 W/(mK) across the lower mantle. Stamenković et al. (2011), using the Ross model (Ross et al., 1984) and approximative equations of state to derive high-P,T lattice thermal conductivities from available data, also obtained values lower than ours, with $\lambda_{\max}$ not exceeding 8 W/(mK) for an iron-free mantle composition (20% MgO and 80% Pv by volume). We emphasize that our data are based on simulations directly at lower-mantle conditions and do not depend on extrapolations.

Finally, an estimate for the heat flux across the CMB is presented. Given the temperatures T_1 and T_2 at two different depths z_1 and z_2 as boundary conditions, the steady-state heat current density j_Q is determined by an integral form of Fourier's law,

$$j_Q = -\frac{1}{z_2 - z_1} \int_{T_1}^{T_2} dT \lambda(\rho, T) \tag{4.7}$$

where the two concentric spheres corresponding to z_1 and z_2 are locally approximated as parallel planes. Taking the temperature at the CMB and 120 km above from Stacey and Davis (2008) and neglecting the small density variation across this layer, we obtain an average CMB heat flux of 21.5 TW for a Pv/MgO aggregate and of 21.2 TW for a PPv/MgO aggregate. This estimate is based on a specific thermal model of the Earth, and a different temperature profile at the CMB would lead to a somewhat different estimate of the CMB heat flux. Assuming that the presence of iron impurities reduces the heat flux by 50% (Manthilake et al., 2011a), it is estimated to be 10.8 TW on average for an Fe-bearing Pv/MgO aggregate and 10.6 TW for a Fe-bearing PPv/MgO aggregate, with possible variations by about $\pm 20\%$, depending on the geometric details of the two-phase assemblage. These values for the CMB heat flux are consistent with previous estimates, spanning a wide range from 5 TW to 15 TW (Lay et al., 2008).

4.7 Conclusions

We performed equilibrium MD simulations and used the Green-Kubo method to calculate lattice thermal conductivities of MgO, $MgSiO_3$ perovskite, and $MgSiO_3$ post-perovskite over a wide range of pressure and temperature conditions relevant to the Earth's deep mantle. To our knowledge, these are the first simulation results for the $MgSiO_3$ phases. Moreover, the thermal conductivity of the lowermost mantle has been determined directly, without extrapolation from experimental or computational low-pressure or low-temperature data and hence is free of the inherent uncertainties.

The data were used to construct a model for thermal conductivities as a function of density and temperature, which was then applied to the Earth's lower mantle. The thermal conductivity was found to increase significantly with depth and to decrease steeply across the thermal boundary layer above the CMB. These results may be used in geodynamic modeling to refine large-scale simulations of mantle convection. In this field, one often assumes a constant thermal diffusivity $\lambda/(\rho c_P)$ (ρ: densitity, c_P:

specific heat capacity) across the mantle (e.g., Tan et al. (2011)), which is poorly constrained, moreover. Together with the approximation $c_P = \text{const.}$, this implies $\lambda \propto \rho$, a rather restrictive assumption, to be contrasted with the more flexible Eq. 4.5.

By combining our thermal conductivity results with a thermal model of the Earth (Stacey and Davis, 2008), the lattice contribution to the CMB heat flux is estimated to be about 11 TW for a Fe-bearing two-phase aggregate (virtually the same with $MgSiO_3$ perovskite and post-perovskite). This relatively high flux is consistent with recent estimates of the heat flux required to generate and maintain mantle plumes (Lay et al., 2008). Due to the large conductivity contrast between MgO and the $MgSiO_3$ phases, the conductivity of the two-phase aggregate depends strongly on the aggregate geometry. Thus, the CMB heat flux may show large lateral variations by up to about $\pm 20\%$.

4.8 Acknowledgments

We thank Thomas C. Chust for the numerical evaluation of the equations of state as well as Hauke Marquardt, Sergio Speziale and Rene Gaßmöller for fruitful discussions. V.H. and S.J. acknowledge financial support of the Deutsche Forschungsgemeinschaft (DFG) through the Grant No. JA1469/4-1 from the Emmy-Noether-Program. Part of the work was carried out under the HPC-EUROPA2 project (project number: 228398) with the support of the European Commission Capacities Area - Research Infrastructures Initiative. We also acknowledge support of DAAD-PROCOPE under grant no. D/9811428.

Chapter 5

Outlook

In the present thesis, we have investigated two particular aspects of the chemical and thermal inhomogeneity of the Earth from an atomistic perspective. It was stated in the introduction that the "reductionist" approach, inherent to the atomistic simulation of materials, allows us to derive all macroscopic thermodynamic properties of a system from the behavior of its microscopic constituents, *at least in principle*. The atomic-scale explanation of trace element partitioning and the calculation of thermal conductivities from crystal lattice vibrations are two examples for the power of this method. It is clear, however, that the Earth as a whole is far too big and too complex to be described directly in terms of the statistical mechanics of individual atoms. Instead, a multi-scale approach has to be taken which bridges the many orders of magnitude between atoms and planetary bodies. In this perspective, the role of atomistic modeling is to provide material parameters for modeling and the theoretical description on the next-higher scale. Thus, the observed relation between melt composition, melt structure and the chemical affinity of trace elements may be used to design or to refine (large-scale) models for trace element partitioning during crystallization processes in magmatic systems. The calculated thermal conductivities of lower-mantle minerals and their variation with density and temperature can serve as an input for large-scale hydrodynamic simulations of mantle convection, which depend on accurate material parameters.

The results on the thermal conductivity of lower-mantle phases are complemented by ongoing work which investigates the effects of isotopic disorder and lattice imperfections on the lattice thermal conductivity. In chapter 4, it was suggested that these effects might explain, at least partially, the discrepancies between simulated and experimental thermal conductivities at room temperature in MgO as well as $MgSiO_3$ perovskite and post-perovskite. There is experimental (Kremer et al., 2004; Chang et al., 2006) and computational (Tang and Dong, 2010; Lindsay et al., 2012) evidence that isotopic disorder can reduce thermal conductivities at low temperatures by up to an order of magnitude (e.g. for Si in the diamond structure) but becomes rapidly less important with increasing temperature. We are currently applying the Green-Kubo equilibrium MD method to the lower mantle phases using simulation cells with a random distribution of isotopes in order to determine this effect quantitatively. This will help to compare simulation results more directly to experimental data, typically obtained from isotopically disordered samples. Moreover, a similar simulation approach with randomly distributed lattice defects is envisaged to evaluate their effect on the thermal conductivity.

Another study is underway which is devoted to the thermal conductivity of silicate *melts*. There is strong evidence that the Earth went through a phase in its early history when it was molten to a significant extent and at least parts of the mantle formed a silicate magma ocean (Solomatov, 2009; Rubie et al., 2009). The dynamical behavior of this large melt body is governed by the Rayleigh number, which depends on the thermal conductivity, among other thermodynamical and geophysical parameters. Adjaoud et al. (2011) studied different scenarios for the magma ocean, with depths reaching up to 2740 km. In the absence of direct information about the thermal conductivity of silicate melts at these conditions, its value is poorly constrained, and the authors assumed values between 1 W/(mK) and 3 W/(mK) which

were inferred from ambient-pressure data and solid analogs.

As demonstrated in the previous chapter, equilibrium molecular dynamics simulations in conjunction with the Green-Kubo formalism are a powerful tool to determine thermal conductivities of crystalline solids even at conditions where experiments are not (yet) possible. However, the approach is rooted directly in general principles of statistical mechanics and does not depend on the crystalline structure of the studied system. Therefore, it can also be applied to liquids (see, e.g., Ohtori et al. (2009a)). This is an advantage over the lattice-dynamics method (Tang and Dong (2010)) which relies on the existence of well-defined phonons, i.e. vibrational modes of a harmonic crystal lattice, and treats anharmonic effects via a low-order perturbation approach. Melting, however, is a paradigmatic manifestation of strong anharmonicity, and hence the thermal conductivity of liquids cannot be obtained with the lattice-dynamics method.

We are currently calculating the thermal conductivity of a magma ocean, approximated as Mg_2SiO_4 melt, by means of the Green-Kubo method, at temperatures between 2600 K and 3000 K and pressures varying between ambient conditions and 32 GPa. The results will complement previous computational studies on this melt which explored thermodynamic properties and the viscosity (Adjaoud et al., 2008, 2011), and the new data will contribute to constraining the thermal and dynamical state of a magma ocean.

Bibliography

Adjaoud, O., Steinle-Neumann, G., Jahn, S., 2008. Mg_2SiO_4 liquid under high pressure from molecular dynamics. Chem. Geol. 256, 184–191.

Adjaoud, O., Steinle-Neumann, G., Jahn, S., 2011. Transport properties of Mg_2SiO_4 liquid at high pressure: physical state of a magma ocean. Earth Planet. Sci. Lett. 312, 463–470.

Aguado, A., Bernasconi, L., Jahn, S., Madden, P. A., 2003. Multipoles and interaction potentials in ionic materials from planewave-DFT calculations. Faraday Discuss. 124, 171–184.

Alfè, D., Gillan, M. J., Price, G. D., 1999. The melting curve of iron at the pressures of the Earth's core from ab initio calculations. Nature 401, 462–464.

Allen, M. P., Tildesley, D. J., 1987. Computer simulations of liquids. Oxford University Press Inc., New York.

Ashcroft, N. W., Mermin, N. D., 1976. Solid State Physics. Thomson Learning, Inc.

Aubert, J., Labrosse, S., Poitou, C., 2009. Modelling the paleo-evolution of the geodynamo. Geophys. J. Int. 179, 1414–1428.

Ayala, R., Sprik, M., 2008. A Classical Point Charge Model Study of System Size Dependence of Oxidation and Reorganization Free Energies in Aqueous Solutions. J. Phys. Chem. 112, 257–269.

Beattie, P., Drake, M., Jones, J., Leeman, W., Longhi, J., McKay, G., Nielsen, R., Palme, H., Shaw, D., Takahashi, E., Watson, B., 1993. Terminology for trace-element partitioning. Geochim. Cosmochim. Acta 57, 1605–1606.

Blundy, J., Wood, B., 1994. Prediction of crystal-melt partition coefficients from elastic moduli. Nature 372, 452–454.

Bois, L., Barré, N., Guittet, M. J., Guillopé, S., Trocellier, P., Gautier-Soyer, M., Verdier, P., Laurent, Y., 2002. Aqueous corrosion of lanthanum aluminosilicate glasses: influence of inorganic anions. J. nucl. mater. 300, 141–150.

Born, M., Oppenheimer, R., 1927. Zur Quantentheorie der Molekeln. Ann. Phys. 389, 457–484.

Brice, J. C., 1975. Some thermodynamic aspects of the growth of strained crystals. J. Cryst. Growth 28, 249–253.

Callen, H. B., 1985. Thermodynamics and an Introduction to Thermostatistics. John Wiley & Sons, Inc., New York.

Car, R., Parrinello, M., 1985. Unified approach for molecular dynamics and density-functional theory. Phys. Rev. Lett. 55, 2471–2474.

Carlson, R. W. (Ed.), 2005. The mantle and core. Elsevier, Amsterdam.

Casimir, H. B. G., Polder, D., 1948. The influence of retardation on the London-van der Waals forces. Phys. Rev. 73, 360–372.

Chang, C. W., Fennimore, A. M., Afanasiev, A., Okawa, D., Ikuno, T., Garcia, H., Li, D., Majumdar, A., Zettl, A., 2006. Isotope effect on the thermal conductivity of boron nitride nanotubes. Phys. Rev. Lett. 97, 085901.

Chu, X., Dalgarno, A., 2004. Linear response time-dependent density functional theory for van der Waals forces. J. Chem. Phys. 121, 4083–4088.

Clayden, N. J., Esposito, S., Aronne, A., Pernice, P., 1999. Solid state ^{27}Al NMR and FTIR study of lanthanum aluminosilicate glasses. J. non-cryst. sol. 258, 11–19.

Cohen-Tannoudji, C. Diu, B., Laloe, F., 1999. Quantenmechanik. de Gruyter, Berlin.

Davies, G. F., 2007. Mantle regulation of core cooling: A geodynamo without core radioactivity? Phys. Earth Planet. Int. 160, 215–229.

de Groot, S. R., Mazur, P., 1984. Non-equilibrium thermodynamics. Dover Publications, Inc., New York.

de Koker, N., 2009. Thermal conductivity of MgO periclase from equilibrium first principles molecular dynamics. Phys. Rev. Lett. 103, 125902.

de Koker, N., 2010. Thermal conductivity of MgO periclase at high pressure: Implications for the D" region. Earth Planet. Sci. Lett. 292, 392–398.

Drewitt, J. W. E., Hennet, L., Zeidler, A., Jahn, S., Salmon, P., Neuville, D., Fischer, H. E., 2012. Structural transformations on vitrification in the fragile glass forming system $CaAl_2O_6$, submitted for publication in Phys. Rev. Lett.

Drewitt, J. W. E., Jahn, S., Cristiglio, V., Bytchkov, A., Leydier, M., Brassamin, S., Fischer, H. E., Hennet, L., 2011. The structure of liquid calcium aluminates as investigated using neutron and high-energy x-ray diffraction in combination with molecular dynamics simulation methods. J. Phys.: Condens. Matter 23, 155101.

Du, J., 2009. Molecular dynamics simulations of the structure and properties of low silica yttrium aluminosilicate glasses. J. Am. Ceram. Soc. 92, 87–95.

Dupree, R., Lewis, M. H., Smith, M. E., 1989. A high-resolution NMR study of the La-Si-Al-O-N system. J. Am. Ceram. Soc. 111, 5125–5132.

Dziewonski, A. M., Anderson, D. L., 1981. Preliminary reference Earth model. Phys. Earth Planet. Int. 25, 297–356.

Esfarjani, K., Chen, G., 2011. Heat transport in silicon from first-principles calculations. Phys. Rev. B 84, 085204.

Faber, T. E., Ziman, J. M., 1965. A Theory of the Electrical Properties of Liquid Metals III. The Resistivity of Binary Alloys. Phil. Mag. 11, 153–173.

Florian, P., Sadiki, N., Massiot, D., Coutures, J. P., 2007. ^{27}Al NMR study of the structure of lanthanum- and yttrium-based aluminosilicate glasses and melts. J. Phys. Chem. B 111, 9747–9757.

Frenkel, D., Smit, B., 2002. Understanding molecular simulation: from algorithms to applications. Academic Press, San Diego.

Galamba, N., Nieto de Castro, C. A., Ely, J. F., 2007. Equilibrium and nonequilibrium molecular dynamics simulations of the thermal conductivity of molten alkali halides. J. Chem. Phys. 126, 204511.

Gillan, M. J., Alfè, D., Brodholt, J., Vocadlo, L., Price, G. D., 2006. First-rinciples modelling of Earth and planetary materials at high pressures and temperatures. Rep. Prog. Phys. 69, 2365–2441.

Goldschmidt, V. M., 1937. The principles of distribution of chemical elements in minerals and rocks. J. Chem. Soc. , 655–673.

Goncharov, A. F., Beck, P., Struzhkin, V. V., Haugen, B. D., Jacobsen, S. D., 2009. Thermal conductivity of lower-mantle minerals. Phys. Earth Planet. Int. 174, 24–32.

Gori-Giorgi, P., Seidl, M., Vignale, G., 2009. Density-functional theory for strongly interacting electrons. Phys. Rev. Lett. , 166402.

Haigis, V., Salanne, M., Jahn, S., 2012a. Thermal conductivity of MgO, $MgSiO_3$ perovskite and post-perovskite in the Earth's deep mantle. Earth Planet. Sci. Lett. 355-356, 102–108.

Haigis, V., Salanne, M., Simon, S., Wilke, M., Jahn, S., 2012b. Molecular dynamics simulations of Y in silicate melts and implications for trace element partitioning. Chem. Geol. .
URL http://dx.doi.org.10.1016/j.chemgeo.2012.08.021

Hofmeister, A. M., 1999. Mantle Values of Thermal Conductivity and the Geotherm from Phonon Lifetimes. Science 283, 1699–1706.

Hofmeister, A. M., Yuen, D. A., 2007. Critical phenomena in thermal conductivity: Implications for lower mantle dynamics. J. Geodyn. 44, 186–199.

Hohenberg, P., Kohn, W., 1964. Inhomogeneous electron gas. Phys. Rev. 136, B864–B871.

Hoover, W. G., 1985. Canonical dynamics: Equilibrium phase-space distributions. Phys. Rev. A 31, 1695–1697.

Ibers, J. A., Hamilton, W. C. (Eds.), 1974. International tables for x-ray crystallography. Vol. 4. The Kynoch Press, Birmingham.

Iftekhar, S., Grins, J., Gunwidjaja, P. N., Edén, M., 2011. Glass formation and structure-property-composition relations of the RE_2O_3-Al_2O_3-SiO_2 (RE = La, Y, Lu, Sc) systems. J. Am. Ceram. Soc. 94, 2429–2435.

Iftekhar, S., Leonova, E., Edén, M., 2009. Structural characterization of lanthanum aluminosilicate glasses by ^{29}Si solid-state NMR. J. non-cryst. sol. 355, 2165–2174.

Iftekhar, S., Pahari, B., Okhotnikov, K., Jaworski, A., Stevensson, B., Grins, J., Edén, M., 2012. Properties and structures of RE_2O_3-Al_2O_3-SiO_2 (RE = Y, Lu) glasses probed by molecular dynamics simulations and solid-state NMR: the roles of aluminum and rare-earth ions for dictating the microhardness. J. Phys. Chem. C 116, 18394–18406.

Iitaka, T., Hirose, K., Kawamura, K., Murakami, M., 2004. The elasticity of the $MgSiO_3$ post-perovskite phase in the Earth's lowermost mantle. Nature 430, 442–445.

Jahn, S., Madden, P. A., 2007. Modeling Earth materials from crustal to lower mantle conditions: A transferable set of interaction potentials for the CMAS system. Phys. Earth Planet. Int. 162, 129–139.

Jaworski, A., Stevensson, B., Pahari, B., Okhotnikov, K., Edén, M., 2012. Local structures and Al/Si ordering in lanthanum aluminosilicate glasses explored by advanced ^{27}Al NMR experiments and molecular dynamics simulations. Phys. Chem. Chem. Phys. 14, 15866–15878.

Katsura, T., 1997. Thermal diffusivity of periclase at high temperatures and high pressures. Phys. Earth Planet. Int. 101, 73–77.

Keppler, H., Dubrovinsky, L. S., Narygina, O., Kantor, I., 2008. Optical Absorption and Radiative Thermal Conductivity of Silicate Perovskite to 125 Gigapascals. Science 322, 1529–1532.

Kirkwood, J. G., 1935. Statistical mechanics of fluid mixtures. J. Chem. Phys. 3, 300–313.

Kohli, J. T., Shelby, J. E., 1991. Magnetooptical properties of rare-earth aluminosilicate glasses. Phys. Chem. Glasses 32, 109–114.

Kohn, W., Sham, L. J., 1965. Self-consistent equations including exchange and correlation effects. Phys. Rev. 140, A1133–A1138.

Koutselos, A. D., Mason, E. A., 1986. Correlation and prediction of dispersion coefficients for isoelectronic systems. J. Chem. Phys. 85, 2154–2160.

Kremer, R. K., Graf, K., Cardona, M., Devyatykh, G. G., Gusev, A. V., Gibin, A. M., Inyushkin, A. V., Taldenkov, A. N., Pohl, H.-J., 2004. Thermal conductivity of isotopically enriched ^{28}Si: revisited. Sol. State Comm. 131, 499–503.

Kubo, R., 1957. Statistical-mechanical Theory of Irreversible Processes. I. J. Phys. Soc. Japan 12, 570–586.

Lange, R. A., Carmichael, I. S. E., 1987. Densities of Na_2O-K_2O-CaO-MgO-FeO-Fe_2O_3-Al_2O_3-TiO_2-SiO_2 liquids: New measurements and derived partial molar properties. Geochim. Cosmochim. Acta 51, 2931–2946.

Lay, T., Hernlund, J., Buffet, B. A., 2008. Core-mantle boundary heat flow. Nature Geoscience 1, 25–32.

Lee, S. K., Stebbins, J. F., 2006. Disorder and the extent of polymerization in calcium silicate and aluminosilicate glasses: O-17 NMR results and quantum chemical molecular orbital calculations. Geochim. Cosmochim. Acta 70, 4275–4286.

Leydier, M., 2010. Méthodes complémentaires pour l'étude de verres et liquides fondus sur grands instruments. PhD thesis, Université d'Orléans.

Lindsay, L., Broido, D. A., Reinecke, T. L., 2012. Thermal conductivity and large isotope effect in GaN from first principles. Phys. Rev. Lett. 109, 095901.

Loewenstein, W., 1954. The distribution of aluminum in the tetrahedra of silicates and aluminates. Am. Mineral. 39, 92–96.

Manthilake, G. M., de Koker, N., Frost, D. J., McCammon, C., 2011a. Lattice thermal conductivity of lower mantle minerals and heat flux from Earth's core. PNAS 108, 17901–17904.

Manthilake, M. A. G. M., de Koker, N., Frost, D. J., 2011b. Thermal conductivity of $CaGeO_3$ perovskite at high pressure. Geophys. Res. Lett. 38, L08301.

Marchi, J., Morais, D. S., Schneider, J., Bressiani, J. C., Bressiani, A. H. A., 2005. Chearacterization of rare earth aluminosilicate glasses. J. non-cryst. sol. 351, 863–868.

Martyna, G. J., Tobias, D. J., Klein, M. L., 1994. Constant pressure molecular dynamics algorithms. J. Chem. Phys. 101, 4177–4189.

Marx, D., Hutter, J., 2000. Ab initio molecular dynamics: Theory and implementation. In: Grotendorst, J. (Ed.), Modern Methods and Algorithms of Quantum Chemistry, Forschungszentrum Jülich, NIC Series. Vol. 1. pp. 301–449.

Marzari, N., Vanderbilt, D., 1997. Maximally localized generalized Wannier functions for composite energy bands. Phys. Rev. B 56, 12847–12865.

Massiot, D., Trumeau, D., Touzo, B., Farnan, I., Rifflet, J.-C., Douy, A., Coutures, J.-P., 1995. Structure and Dynamics of $CaAl_2O_4$ from liquid to glass: a high-temperature ^{27}Al NMR time-resolved study. J. Phys. Chem. 99, 16455–16459.

Müller-Plathe, F., 1997. A simple nonequilibrium molecular dynamics method for calculating the thermal conductivity. J. Chem. Phys. 106, 6082–6085.

Murakami, M., Hirose, K., Kawamura, K., Sata, N., Ohishi, Y., 2004. Post-Perovskite Phase Transition in $MgSiO_3$. Science 304, 855–858.

Mysen, B., Richet, P., 2005. Silicate glasses and melts. Properties and Structure. Elsevier, Amsterdam.

Mysen, B. O., 2004. Element partitioning between minerals and melts, melt composition, and melt structure. Chem. Geol. 213, 1–16.

Naliboff, J. B., Kellogg, L. H., 2007. Can large increases in viscosity and thermal conductivity preserve large-scale heterogeneity in the mantle? Phys. Earth Planet. Int. 161, 86–102.

Nieto-Draghi, C., Avalos, J. B., 2003. Non-equilibrium momentum exchange algorithm for molecular dynamics simulation of heat flow in multicomponent systems. Mol. Phys. 101, 2303–2307.

Nosé, S., 1984. A molecular dynamics method for simulations in the canonical ensemble. Mol. Phys. 52, 255–268.

Oganov, A. R., Ono, S., 2004. Theoretical and experimental evidence for a post-perovskite phase of $MgSiO_3$ in Earth's D" layer. Nature 430, 445–448.

Ohta, K., Yagi, T., Taketoshi, N., Hirose, K., Kombayashi, T., Baba, T., Ohishi, Y., Hernlund, J., 2012. Lattice thermal conductivity of $MgSiO_3$ perovskite and post-perovskite at the core-mantle boundary. Earth Planet. Sci. Lett. 349-350, 109–115.

Ohtori, N., Oono, T., Takase, T., 2009a. Thermal conductivity of molten alkali halides: Temperature and density dependence. J. Chem. Phys. 130, 044505.

Ohtori, N., Salanne, M., Madden, P. A., 2009b. Calculations of the thermal conductivities of ionic materials by simulation with polarizable interaction potentials. J. Chem. Phys. 130, 104507.

Onuma, N., Higuchi, H., Wakita, H., Nagasawa, H., 1968. Trace element partition between two pyroxenes and the host lava. Earth Planet. Sci. Lett. 5, 47–51.

Osako, M., Ito, E., 1991. Thermal diffusivity of $MgSiO_3$ perovskite. Geophys. Res. Lett. 18, 239–242.

Pauvert, O., Zanghi, D., Salanne, M., Simon, C., Rakhmatullin, A., Matsuura, H., Okamoto, Y., Vivet, F., Bessada, C., 2010. In situ experimental evidence for a nonmonotonous structural evolution with composition in the molten $LiF–ZrF_4$ system. J. Phys. Chem. B 114, 6472–6479.

Pertermann, M., Whittington, A. G., Hofmeister, A. M., Spera, F. J., Zayak, J., 2008. Transport properties of low-sanidine single-crystals, glasses and melts at high temperature. Contrib. Mineral. Petrol. 155, 689–702.

Philpotts, A. R., Ague, J. J., 2009. Principles of igneous and metamorphic petrology. Cambridge University Press, Cambridge.

Piazzoni, A. S., Steinle-Neumann, G., Bunge, H.-P., Dolejš, D., 2007. A mineralogical model for density and elasticity of the Earth's mantle. Geochem. Geophys. Geosyst. 8, Q11010.

Pozdnyakova, I., Sadiki, N., Hennet, L., Cristiglio, V., Bytchkov, A., Cuello, G. J., Coutures, J. P., Price, D. L., 2008. Structures of lanthanum and yttrium aluminosilicate glasses determined by x-ray and neutron diffraction. J. non-cryst. sol. 354, 2038–2044.

Prowatke, S., Klemme, S., 2005. Effect of melt composition on the partitioning of trace elements between titanite and silicate melt. Geochim. Cosmochim. Acta 69, 695–709.

Ross, R. G., Andersson, P., Sundqvist, B., Bäckström, G., 1984. Thermal conductivity of solids and liquids under pressure. Rep. Prog. Phys. 47, 1347–1402.

Rowley, A. J., Jemmer, P., Wilson, M., Madden, P. A., 1998. Evaluation of the many-body contributions to the interionic interactions in MgO. J. Chem. Phys. 108, 10209–10219.

Rubie, D. C., Nimmo, F., Melosh, H. J., 2009. Formation of Earth's core. In: Stevenson, D. (Ed.), Evolution of the Earth. Elsevier, Amsterdam, pp. 51–90.

Ryerson, F. J., Hess, P. C., 1978. Implications of liquid-liquid distribution coefficients to mineral-melt partitioning. Geochim. Cosmochim. Acta 42, 921–932.

Salanne, M., Marrocchelli, D., Merlet, C., Ohtori, N., Madden, P. A., 2011. Thermal conductivity of ionic systems from equilibrium molecular dynamics. J. Phys. Cond. Mat. 23, 102101.

Salanne, M., Rotenberg, B., Jahn, S., Vuilleumier, R., Simon, C., Madden, P., 2012. Including many-body effects in models for ionic liquids. Theor. Chem. Acc. 131, 1143.

Salanne, M., Simon, C., Turq, P., 2008. Calculation of activities of ions in molten salts with potential application to the pyroprocessing of nuclear waste. J. Phys. Chem. 112, 1177–1183.

Schaller, T., Stebbins, J. F., 1998. The structural role of lanthanum and yttrium in aluminosilicate glasses: A ^{27}Al and ^{17}O MAS NMR study. J. Phys. Chem. B 102, 10690–10697.

Schmidt, M. W., Connolly, J. A. D., Günther, D., Bogaerts, M., 2006. Element partitioning: the role of melt structure and composition. Science 312, 1646–1650.

Sears, V. F., 1992. Neutron scattering lengths and cross sections. Neutron News 3, 26–37.

Sellan, D. P., Landry, E. S., Turney, J. E., McGaughey, A. J. H., Amon, C. H., 2010. Size effects in molecular dynamics thermal conductivity predictions. Phys. Rev. B 81, 214305.

Shannon, R. D., 1976. Revised effective ionic radii and systematic studies of interatomic distances in halides and chalcogenides. Acta Cryst. A32, 751–767.

Shaw, D. M., 2006. Trace elements in magmas. A theoretical treatment. Cambridge University Press, Cambridge.

Shelby, J. E., Kohli, J. T., 1990. Rare-earth aluminosilicate glasses. J. Am. Ceram. Soc. 73, 39–42.

Simon, S., Wilke, M., Chernikov, R., Klemme, S., hennet, L., 2012. The influence of composition on the local structure around yttrium in quenched silicate melts – insighst from EXAFS. Chem. Geol. .
URL http://dx.doi.org/10.1016/j.chemgeo.2012.09.017

Slater, J. C., Kirkwood, J. G., 1931. The van der Waals forces in gases. Phys. Rev. 37, 682–697.

Solomatov, V., 2009. Magma oceans and primordial mantle differentiaion. In: Stevenson, D. (Ed.), Evolution of the Earth. Elsevier, Amsterdam, pp. 91–119.

Speziale, S., Zha, C.-S., Duffy, T. S., Hemley, R. J., Mao, H.-k., 2001. Quasi-hydrostatic compression of magnesium oxide to 52GPa: Implications for the pressure-volume-temperature equation of state. J. Geophys. Res. 106, 515–528.

Spiekermann, G., Steel-MacInnis, M., Schmidt, C., Jahn, S., 2012. Vibrational mode frequencies of silica species in SiO_2-H_2O liquids and glasses from ab initio molecular dynamics. J. Chem. Phys. 136, 154501.

Stacey, F. D., Davis, P. M., 2008. Physics of the Earth, 4th Edition. Cambridge University Press, Cambridge.

Stackhouse, S., Stixrude, L., Karki, B. B., 2010. Thermal conductivity of periclase (MgO) from first principles. Phys. Rev. Lett. 104, 208501.

Stamenković, V., Breuer, D., Spohn, T., 2011. Thermal and transport properties of mantle rock at high pressure: Applications to super-Earths. Icarus 216, 572–596.

Stebbins, J. F., Dubinsky, E. V., Kanehashi, K., Kelsey, K. E., 2008. Temperature effects on non-bridging oxygen and aluminum coordination number in calcium aluminosilicate glasses and melts. Geochim. Cosmochim. Acta 72, 910–925.

Stebbins, J. F., McMillan, P. E., Dingwell, D. B. (Eds.), 1995. Structure, dynamics and properties of silicate melts. Mineralogical Society of America, Washington DC.

Stebbins, J. F., Xu, Z., 1997. NMR evidence for excess non-bridging oxygen in an aluminosilicate glass. Nature 390, 60–62.

Stixrude, L., Lithgow-Bertelloni, C., 2005. Thermodynamics of mantle minerals - I. Physical properties. Geophys. J. Int. 162, 610–632.

Stone, A. J., 1996. The theory of intermolecular forces. Oxford University Press Inc., New York.

Tamura, S.-i., 1983. Isotope scattering of dispersive phonons in Ge. Phys. Rev. B 27, 858–866.

Tan, E., Leng, W., Zhong, S., Gurnis, M., 2011. On the location of plumes and lateral movement of thermochemical structures with high bulk modulus in the 3-D compressible mantle. Geochem. Geophys. Geosys. 12, Q07005.

Tanabe, S., 1999. Optical transitions of rare earth ions for amplifiers: how the local structure works in glass. J. non-cryst. sol. 259, 1–9.

Tang, K. T., Toennies, J. P., 1984. An improved simple model for the van der Waals potential based on universal damping functions for the dispersion coefficients. J. Chem. Phys. 80, 3726–3741.

Tang, X., Dong, J., 2010. Lattice thermal conductivity of MgO at conditions of Earth's interior. PNAS 107, 4539–4543.

Tkatchenko, A., DiStasio, R. A., Car, R., Scheffler, M., 2012. Accurate and efficient method for many-body van der Waals interactions. Phys. Rev. Lett. 108, 236402.

Troullier, N., Martins, J. L., 1991. Efficient pseudopotentials for plane-wave calculations. Phys. Rev. B 43, 1993–2005.

Veksler, I. V., Dorfmann, A. M., Danyushevsky, L. V., Jakobsen, J. K., Dingwell, D. B., 2006. Immiscible silicate liquid partition coefficients: implications for crystal-melt element partitioning and basalt petrogenesis. Contrib. Mineral. Petrol. 152, 685–702.

Volz, S. G., Chen, G., 2000. Molecular-dynamics simulation of thermal conductivity of silicon crystals. Phys. Rev. B 61, 2651–2656.

Vuilleumier, R., Sator, N., Guillot, B., 2009. Computer modeling of natural silicate melts: what can we learn from ab initio simulations. Geochim. Cosmochim. Acta 73, 6313–6339.

Watson, E. B., 1976. Two-liquid partition coefficients: experimental data and geochemical implications. Contrib. Mineral. Petrol. 56, 119–134.

Wilding, M. C., Benmore, C. J., McMillan, P. F., 2002. A neutron diffraction study of yttrium- and lanthanum-aluminate glasses. J. non-cryst. sol. 297, 143–155.

Wilson, M., Madden, P. A., 1993. Polarization effects in ionic systems from first principles. J. Phys.: Condens. Matter. 5, 2687–2706.

Wood, B. J., Blundy, J. D., 1997. A predictive model for rare earth element partitioning between clinopyroxene and anhydrous silicate melt. Contrib. Mineral. Petrol. 129, 166–181.

Xu, W., Lithgow-Bertelloni, C., Stixrude, L., Ritsema, J., 2008. The effect of bulk composition and temperature on mantle seismic structure. Earth Planet. Sci. Lett. 275, 70–79.

Acknowledgements

I would like to thank all the people who accompanied me over the past three years and supported me during my work on this thesis. First of all, I thank Sandro Jahn for the highly committed and insightful supervision, always with the right balance of guidance and scientific freedom. I also thank all the colleagues of section 3.3 at GFZ Potsdam, in particular my office mate Piotr Kowalski, who taught me the art of pragmatism, Georg Spiekermann, always willing to discuss all kinds of questions from petrology to quantum chemistry, as well as Sebastian Simon and Max Wilke, who introduced me to the real (not simulated) world, taking me to EXAFS experiments in Grenoble. I would also like to thank Sergio Speziale and Hauke Marquardt, who were eager to share their knowledge in geo- and mineral physics. Mathieu Salanne was a wonderful host during my HPC Europa-funded stay at the Université Pierre et Marie Curie in Paris and provided valuable insights into advanced simulation methods. Finally, I thank my family for supporting me in every respect during all these years.

Erklärung der Eigenständigkeit

Hiermit versichere ich, dass ich die vorliegende Arbeit selbständig verfasst und keine anderen als die angegebenen Hilfsmittel benutzt habe. Die Stellen der Arbeit, die anderen Werken wörtlich oder inhaltlich entnommen sind, wurden durch entsprechende Angaben der Quellen kenntlich gemacht. Die Beiträge der Koautoren der veröffentlichten und noch nicht veröffentlichten Arbeiten sind in der Einleitung aufgeführt. Diese Arbeit wurde nicht schon einmal in einem früheren Promotionsverfahren eingereicht.

Volker Haigis